

HERON contains contributions based mainly on research work performed in I.B.B.C. and STEVIN and related to strength of materials and structures and materials science.

HERON

vol. 26
1981
no. 1B

Contents

NUMERICAL MODELLING OF BOND-SLIP BEHAVIOUR

A. K. de Groot
G. M. A. Kusters
Th. Monnier

I.B.B.C. Institute TNO
for Building Materials and Building Structures
P.O. Box 49
2600 AA Delft, The Netherlands

Jointly edited by:

STEVIN-LABORATORY
of the Department of
Civil Engineering of the
Delft University of Technology,
Delft, The Netherlands
and
I.B.B.C. INSTITUTE TNO
for Building Materials
and Building Structures,
Rijswijk (ZH), The Netherlands.

EDITORIAL BOARD:

J. Witteveen, *editor in chief*
G. J. van Alphen
M. Dragosavić
H. W. Reinhardt
A. C. W. M. Vrouwenvelder
L. van Zetten

Secretary:

G. J. van Alphen
Stevinweg 1
P.O. Box 5048
2600 GA Delft, The Netherlands
Tel. 0031-15-785919
Telex 38070 BITHD

List of symbols	3
Preface	5
Summary	7
1 Introduction	8
2 Constructing the model for the axially symmetric element	10
2.1 Bond-slip zone	10
2.2 Combining the bond-slip element with the reinforcement element	14
2.3 Further elaboration	17
2.4 Tyings	19
3 Constructing the model for the 3D element	20
3.1 General	20
3.2 Element stiffness matrix	22
3.3 Physical thickness of reinforcing bar ...	24
3.4 Symmetry	24
4 Some general supplementary matters	26
4.1 Delimitation of the τ - Δ -relation ...	26
4.2 Algebraic sign the ribfactor k	27
4.3 Radial tension	29
5 Possible translation of 3D into 2D model	30
5.1 Introduction	30
5.2 Derivation of formulas	30
5.3 Element stiffness matrix	34



This publication has been issued in close co-operation with the Netherlands Committee for Research, Codes and Specifications for Concrete (CUR-VB).

6	Constitutive equations of concrete and steel	35
6.1	Concrete	35
6.1.1	Yield criterion.	35
6.1.2	Tension cut-off criterion 1	37
6.1.3	Tension cut-off criterion 2	37
6.1.4	Relation between f_{ct} and the auxiliary quantities f_{t2} and f_{t3}	37
6.2	Steel	38
7	Verification of the axially symmetric element . . .	38
7.1	Verification with reference to tests by Dörr and Mehlhorn.	38
7.1.1	Data of the tests.	38
7.1.2	Schematization of material properties in the analysis and element distribution . .	40
7.2	Verification with reference to tests without radial pressure.	41
7.2.1	General	41
7.2.2	Effect of load level.	42
7.2.3	Preliminary parameter study	43
7.3	Verification with reference to tests with radial pressure	45
7.3.1	General	45
7.3.2	Distribution of steel stress.	45
7.3.3	Parameter study	48
7.3.4	Provisional conclusions and recommendations	54
8	Verification of the symmetric variant of the 3D element	56
8.1	Introduction	56
8.2	Schematization of material properties in the analysis and element distribution	57
8.3	Bond-slip parameters	58
8.4	Comparison of numerical and experimental results.	60
8.5	Stress distribution	60
8.6	Conclusions	60
9	Experiments for the general 3D element	62
9.1	Description of test specimens	62
9.2	Material data.	64
9.3	Steel strain measurements.	64
9.4	Results of the measurements	65
10	Verification of the general 3D element.	73
10.1	Mathematical model	73
10.2	Material properties adopted in the analysis	74
10.3	Calculation procedure.	76
10.4	Results of the analysis	76
10.5	Comparison with experimental results	82
11	Conclusions	88
	References	89

Publications in HERON since 1970

List of symbols

A	area
\mathbf{B}	relation between internal strains and nodal displacements
\mathbf{C}	constitutive relation
C_1, C_2	elements of \mathbf{C}
E_c, E_s	modulus of elasticity of concrete and steel respectively
F	axial force acting on specimen; yield criterion
N_1, N_2	interpolation functions
Q	distributed radial pressure on specimen
S	slip modulus
\mathbf{S}^e	element stiffness matrix
V	volume
a	bar spacing
c	cohesion (Mohr-Coulomb criterion)
d	thickness of "smeared-out" reinforcement in 2D slip element
f_{cc}	compressive strength of concrete
f_{ct}	tensile strength of concrete
f_{sp}	splitting tensile strength of concrete
f_y	yield stress of reinforcing steel
f_{Ω}, f_{Ω}	auxiliary quantities for defining the tension cut-off criterion 2 and the Mohr-Coulomb yield criterion respectively
k	rib factor
r	radius of reinforcing bar
x, y, z	co-ordinates
$\left. \begin{matrix} u, v, w \\ v_x, v_y \end{matrix} \right\}$	displacements
$\Delta u, \Delta v$	displacement differences, where $\Delta u = \text{slip}$
α	layer thickness coefficient
ε_a	axial strain in reinforcing bar
ε_r	radial strain in reinforcing bar
\emptyset	diameter of reinforcing bar
θ	friction (Mohr-Coulomb criterion)
ν_c, ν_s	Poisson's ratio for concrete and steel respectively
$\sigma_1, \sigma_2, \sigma_3$	principal stresses
σ_a	axial stress in reinforcing bar
σ_r	radial stress on reinforcing bar
τ	shear stress between concrete and reinforcing bar
+	tension
–	compression (or pressure)

Preface

This issue of HERON reports on a mainly theoretical, but also experimental, investigation of the bond-slip model for the analysis of reinforced concrete structures. As sub-project 2 it formed part of the overall “Betonmechanica” (“Concrete Mechanics”) research project, stage 1, which was carried out by Rijkswaterstaat (Netherlands Government Department for Public Civil Engineering Works), TNO-IBBC (Institute TNO for Building Materials and Building Structures), and the Universities of Technology at Eindhoven and Delft.

“Betonmechanica”, stage 1, is subdivided into four sub-projects as indicated in Fig. 1.1. Sub-projects 1, 2 and 4 relate to the modelling of the material behaviour, such as cracking and bond. This investigation is being carried out by specialists in concrete research, and the results it yields serve as input for sub-project 3, the basic models of which are used for describing the global (overall) behaviour of concrete structures. In connection with this research work, two computer programs have been produced, namely the “micro” model and the “macro” model. These have been developed by specialists in numerical methods and structural mechanics.

The purpose of this approach to the subject is to focus attention on the basic components with which the behaviour of reinforced concrete structures can be described. At the same time, other ways and means are being sought with a view to incorporating these basic models in global models with which finally the behaviour of reinforced concrete structures can be studied, so as to improve our fundamental knowledge of the behaviour of this material. More detailed information concerning the object and method of the “Betonmechanica” project, stage 1, and the subdivision of the research work into the four sub-projects is given in [1].

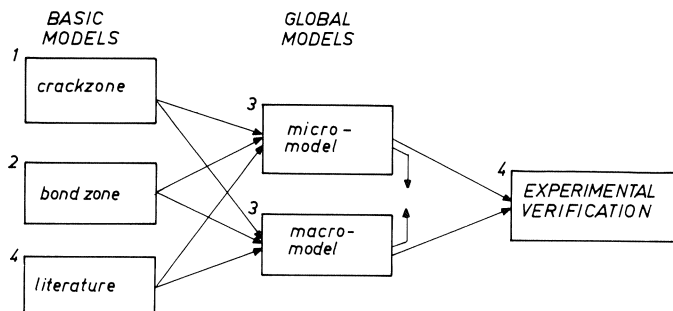


Fig. 1.1. Position occupied by sub-project 2 in the work of A26 “Concrete mechanics”.

The present report deals with the modelling of the behaviour of the bond-slip zone. The other subjects will be dealt with in the HERON issues 1_A and 1_C of this volume.

The joint project is being supervised and partly financed by CUR-VB (Netherlands Committee for Research, Codes and Specifications for Concrete), which set up the Working Committee A 26 “Betonmechanica”. This Working Committee is constituted

as follows: prof. ir. B. W. van der Vlugt (Chairman), prof. dr. ir. J. Blaauwendraad (Secretary), prof. ir. A. L. Bouma, prof. dr. ir. A. S. G. Bruggeling, prof. ir. J. W. Kamerling, prof. ir. H. Lambotte, prof. Dr.-Ing. G. Mehlhorn, ir. Th. Monnier, prof. Dr.-Ing. H. W. Reinhardt, ing. A. C. van Riel, ir. J. C. Slagter (Mentor), prof. ir. J. Witteveen, and prof. Dr. F. H. Wittmann. The authors are indebted to the members of this committee for their contributions, help and encouragements.

The work for sub-project 2 ("The bond-slip zone") was carried out by TNO-IBBC under the guidance of ir. Th. Monnier. The numerical and theoretical work involved in this sub-project was done by ir. A. K. de Groot and ir. G. M. A. Kusters, while ir. F. B. J. Gijsbers and ir. M. Dragosavić undertook the experimental work.

This publication is to be regarded as a comprehensive summary of the results obtained, which have been reported in greater detail in [2] to [9]. This English translation has been prepared by ir. C. van Amerongen.

NUMERICAL MODELLING OF BOND-SLIP BEHAVIOUR

Summary

The development and verification of a numerical bond-slip element suitable for plain as well as for deformed (ribbed) reinforcing bars is reported in this issue of HERON. In the preface it is explained how this study forms part of the overall “Betonmechanica” project in The Netherlands. First, the formulae for the axially symmetric case are derived; then the results are generalized to the three-dimensional case. Next, a procedure for effecting the transformation to the case of plane stress is proposed. After the theoretical treatment of the subject, the suitability of the bond-slip element is assessed with reference to experimental results. More particularly, these relate to tests on cylindrical specimens by Dörr and Mehlhorn [10], tests on rectangular prisms [4] and tests on specimens representing the end portions of beams [9]. Finally, on the basis of the experience gained in the course of this verification, recommendations are made for the various parameters that govern the behaviour of the bond-slip element.

Numerical modelling of bond-slip behaviour

1 Introduction

The study relating to the basic model for bond is more particularly concerned with the bond-slip zone of a beam as shown in Fig. 1.2. The region of constant bending moment as well as the end part of the beam will be considered.

The initial intention was to carry out experimental research, but it soon became apparent that part of the investigation would have to be of a numerical character, the reason being that the global models for which the necessary constituent units had to be provided are two-dimensional. An actual beam section (Fig. 1.3a) is conceived both in the micro model and in the macro model as a section in which the material properties do not vary in the transverse direction (Fig. 1.3b). Since experimental research on the bond-slip zone is always performed on prismatic specimens as shown in Fig. 1.4, some sort of “translation” is required. More particularly, the experiments yield three-dimensional (3D) results which, for the purpose of sub-project 3, have to be converted into two-dimensional (2D) results.

It was therefore decided to verify the experiments with the DIANA program which TNO-IBBC had at its disposal for the analysis of three-dimensional structures. For concrete structures, however, a numerical bond-slip element had to be designed for this purpose and be incorporated in DIANA. This numerical bond-slip element will be dis-

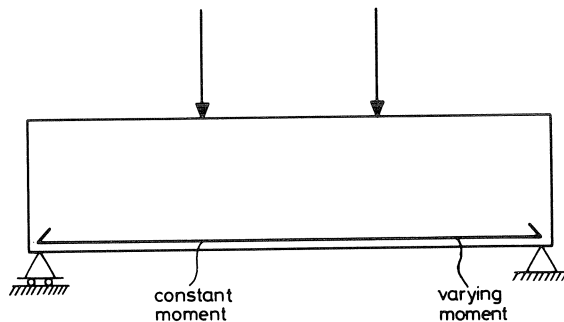


Fig. 1.2. Regions with which sub-project 2 is more particularly concerned.



Fig. 1.3. Schematization of a beam cross-section.

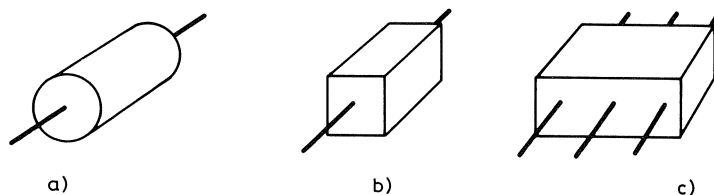


Fig. 1.4. Test specimens for determining the bond-slip relation.

cussed in the present report, and the verification of this model with reference to experimental results will then be described. It will be shown that this verification is proceeding satisfactorily.

With regard to the experimental part of the research it was decided by the present authors not to carry out for themselves the basic tests on the axially symmetric model (Fig. 1.4a), since the results of a comprehensive series of tests by Dörr and Mehlhorn [10] were available.

For general guidance, however, three tests were performed on specimens as shown in Fig. 1.4b [4]. Both the test series mentioned here in fact related to the region of constant bending moment as indicated in Fig. 1.2. The region near the end of the beam from Fig. 1.2 was investigated in two tests [9]. Interim reports on the work have been issued at various times in recent years [2] to [9].

The whole study project is summarized in the present report, which is subdivided as follows.

First, the numerical model employed, with its possible variants, will be dealt with. In Chapter 2 attention will be focused on the axially symmetric element. Next, the general 3D element and a symmetric variant thereof are discussed in Chapter 3. Some general supplementary matters are treated in Chapter 4, after which, in Chapter 5, it is explained how the 3D results obtained could be translated into 2D results for the micro model. The behaviour of the materials concrete and steel is schematized in Chapter 6, and the numerical model is then tested and verified with reference to experiments. Chapter 7 deals with the verification of the axially symmetric element with the aid of the tests by Dörr and Mehlhorn [10]. A parameter study has also been carried out. In Chapter 8 the symmetric variant of the general 3D model is verified with reference to the TNO-IBBC series of tests on prisms [4]. Verification on the basis of experiments is also done in Chapter 10 for the general 3D model, but now with reference to the tests on the beam end parts [9] reported in Chapter 9. The conclusions and recommendations are presented in Chapter 11. Finally, it is to be noted that the numerical model employed in this study concerned with the bond-slip region can be regarded as a model that comprises all the possibilities offered by the spring models variously described in the literature (see Fig. 1.5) [13] to [17]. Most of these models are discontinuous, i.e., springs are assumed to be installed only at the nodes. An improvement in behaviour is obtained by using a continuous spring model, as exemplified by that proposed by Schäfer [14] and the model described in the present report.

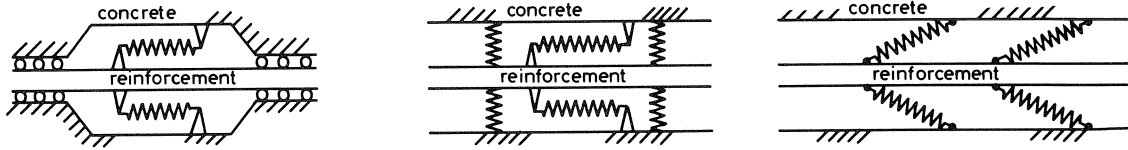


Fig. 1.5. Various possible spring models.
 a. spring in one direction (ref. [13], [14])
 b. two independent springs (ref. [15], [16])
 c. springs at an angle (ref. [17])

2 Constructing the model for the axially symmetric element

2.1 Bond-slip zone

Bond can be thought of as the shear stress or force between a bar and the surrounding concrete. The force in the bar is transmitted to the concrete by bond, or vice versa. According to Lutz and Gergely [19], bond can be conceived as comprising three components:

- chemical adhesion;
- friction;
- mechanical interaction between concrete and steel.

Bond of plain bars depends primarily on the first two of these components, though there is some mechanical interlocking due to roughness of the bar surface. Deformed bars, however, depend primarily on mechanical interlocking for superior bond properties. This does not mean that friction and chemical adhesion are negligible in the case of deformed bars, but that they are secondary.

The above-mentioned aspects will have to play a part in a numerical model. For constructing the model it is helpful to begin with a description of the behaviour of a plain reinforcing bar. The shear stress measured on such a bar, and designated by τ_0 , can be plotted against the associated slip displacement. The curve representing this function is shown in Fig. 2.1a, which could be schematized to so-called rigid-plastic behaviour as in Fig. 2.1b. For describing the actual behaviour within a local context this is an entirely justifiable assumption. At the interface of the concrete and reinforcing steel the connection is completely rigid so long as the shear stress τ_0 is below a certain limiting value. Slip becomes possible only after destruction of the bond. However, measurements will not reveal this rigid-plastic behaviour; a behaviour type more like that in Fig. 2.1c will be found instead. This is due to the circumstance that the strains in the concrete cannot be measured exactly at the interface itself, but always only at a certain distance therefrom. Hence the actually measured slip value is affected by the sliding within the concrete between the interface and the strain gauges.

The fact that the behaviour envisaged in Fig. 2.1c will also be adopted in the numerical model is, however, in no way associated with the phenomenon just referred to. It is

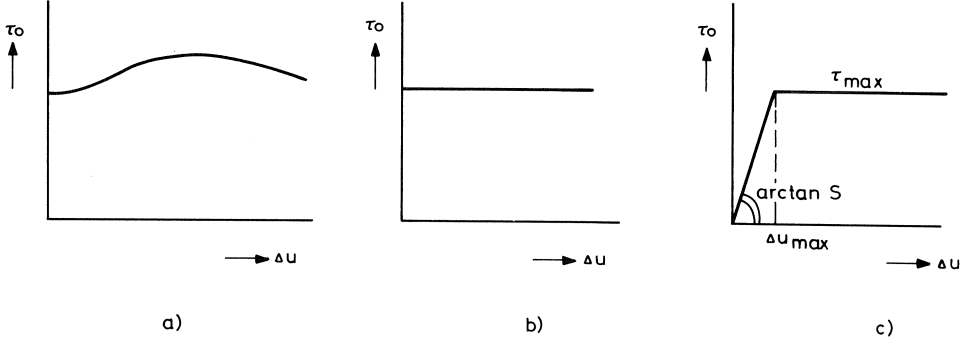


Fig. 2.1. Example of τ_0 - Δu -relations.

instead due to the need to provide, not just a local, but a rather more “global” (overall) description of the bond-slip layer. For example, as a result of cracking, there will exist between the local regions where rigid-plastic behaviour occurs other regions where the bond is distinctly less effective, so that for the purpose of a global description Fig. 2.1c is more appropriate than Fig. 2.1b.

The rising branch in Fig. 2.1c will be defined with the so-called slip modulus S , as follows:

$$\tau_0 = S \Delta u \quad (2.1)$$

The horizontal branch of the diagram is determined by a maximum stress τ_{\max} , which could also be defined as:

$$\tau_{\max} = S \Delta u_{\max} \quad (2.2)$$

The magnitude of τ_{\max} and thus also that of Δu_{\max} will be a function of the radial stress σ_r , which will be further considered in Section 7.3.4.

This fully describes the behaviour of a plain reinforcing bar. In the case of a deformed (ribbed) bar, however, there will be a slip resistance due to the ribs in addition to the above-mentioned slip resistance $S \Delta u$ and $S \Delta u_{\max}$ respectively. In the hypothetical case that $S = 0$ this mechanical interlocking will still be acting. This can be conceived with reference to the behaviour of the specimen shown in Fig. 2.2 [12], where the bar is seen to be surrounded by compression cones – inclined at an angle φ with respect to the vertical – between the cracks. The action of the forces in a segment of the axially symmetric specimen can be clarified with reference to Fig. 2.3. The “prisms” shown in that diagram are conceived as being able to undergo frictionless displacement in relation to one another. Each prism is of such section that in the direction perpendicular to the centre-line of the bar a total force σ_r is present in the prism.

If one such prism is given a unit displacement Δu while the displacement Δw is restrained (see Fig. 2.4a), the change in length will be:

$$\Delta l = - \Delta u \sin \varphi \quad (2.3)$$

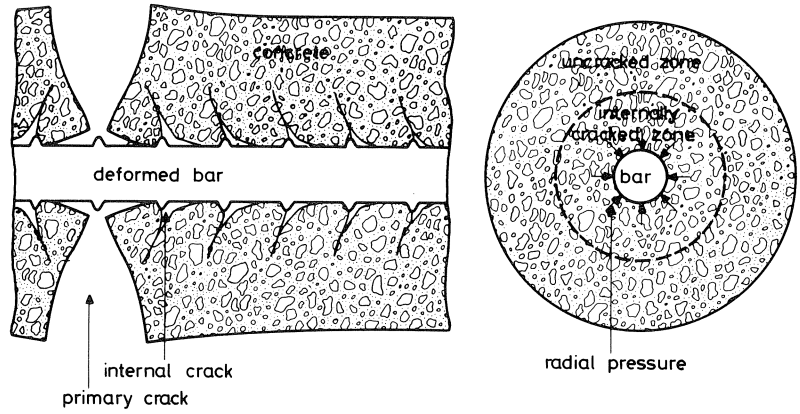


Fig. 2.2. Deformation of concrete around reinforcing steel after formation of internal cracks (schematic diagram) according to Goto [12].

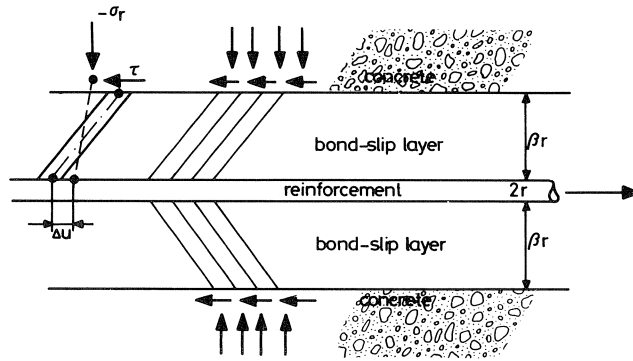


Fig. 2.3. Bond-slip model.

The associated normal force, whose magnitude is $\sigma_r / \cos \varphi$ (see Fig. 2.4c), can be written as:

$$\frac{\sigma_r}{\cos \varphi} = E_l \frac{\Delta l}{l} \quad (2.4)$$

where E_l is a measure of the stiffness of the bond-slip layer. According to Fig. 2.4a the following expression can be written for the length l :

$$l = \frac{\beta r}{\cos \varphi} \quad (2.5)$$

whence, with equations (2.3) and (2.4), is obtained for σ_r :

$$\sigma_r = -\frac{E_l}{\beta r} \sin \varphi \cos^2 \varphi \Delta u \quad (2.6)$$

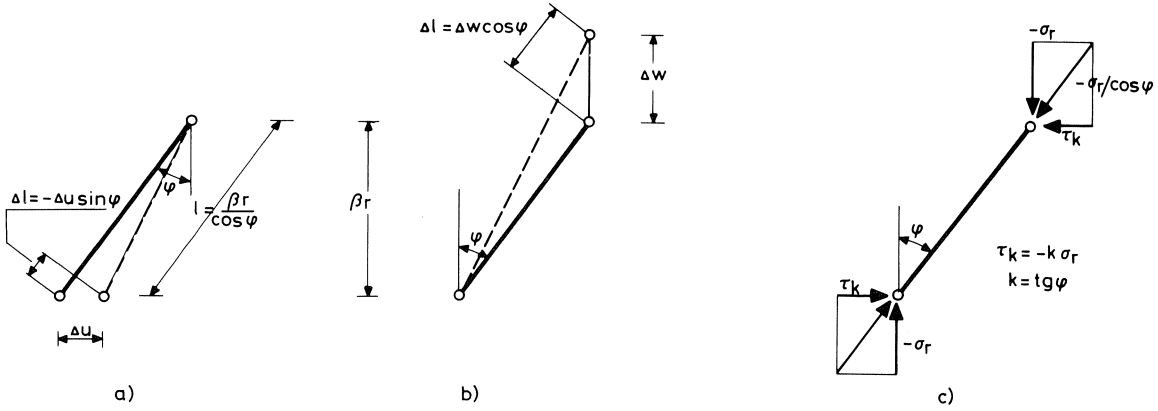


Fig. 2.4. The relation between Δu , Δw , τ_k and σ_r .

Now if the prism is given a unit displacement Δw while the displacement Δu is restrained (see Fig. 2.4b), the change in length will be:

$$\Delta l = \Delta w \cos \varphi \quad (2.7)$$

whence, with equations (2.4) and (2.5):

$$\sigma_r = \frac{E_l}{\beta r} \cos^3 \varphi \Delta w \quad (2.8)$$

The total stress σ_r is obtained by summation of equations (2.6) and (2.8), giving:

$$\sigma_r = -\frac{E_l}{\beta r} (\sin \varphi \cos^2 \varphi \Delta u - \cos^3 \varphi \Delta w) \quad (2.9)$$

or with:

$$k = \operatorname{tg} \varphi \quad (2.10)$$

this expression becomes:

$$\sigma_r = -\frac{E_l \cos^3 \varphi}{\beta r} (k \Delta u - \Delta w) \quad (2.11)$$

From Fig. 2.4c it moreover appears that there is a shear component τ_k expressed by:

$$\tau_k = -\sigma_r \operatorname{tg} \varphi = -k \sigma_r \quad (2.12)$$

In this expression k is the so-called rib factor which represents the effect of the “deformity” (ribbed surface configuration) of the bar, i.e., mechanical interlocking.

It has been established that in the case of a plain reinforcing bar a shear stress τ_0 can be developed without this having consequences with regard to σ_r (equation 2.1). The magnitude of τ_{\max} (equation 2.2) is a function of σ_r , however. It has furthermore been shown that for the deformed bar, in the extreme case where $S = 0$, a shear stress τ_k can be resisted, in conjunction with which a radial stress σ_r will now be produced (equation 2.12).

In general, for a deformed bar the magnitude of S will be non-zero. This being so, the combination of the two models described above would appear to be a reasonable point of departure for further research. In the combined model the shear stress τ is conceived as being composed of the sum of the slip resistance τ_0 and the mechanical interlocking τ_k :

$$\tau = \tau_0 + \tau_k \quad (2.13)$$

or with equations (2.1) and (2.12):

$$\tau = S \Delta u - k \sigma_r \quad (2.14)$$

With equation (2.11) and (2.12) this can be written as:

$$\begin{bmatrix} \tau \\ \sigma_r \end{bmatrix} = S \begin{bmatrix} 1 & 0 \\ 0 & 0 \end{bmatrix} \begin{bmatrix} \Delta u \\ \Delta w \end{bmatrix} + \frac{E_l \cos^3 \phi}{\beta r} \begin{bmatrix} k^2 & -k \\ -k & 1 \end{bmatrix} \begin{bmatrix} \Delta u \\ \Delta w \end{bmatrix} \quad (2.15)$$

This almost completes the model, except that it has yet to be indicated how the limiting magnitude Δu_{\max} from equation (2.2) has to be dealt with. This will be done in Section 4.1 and 7.3.4. There are two approaches to the practical application of the model that has been developed. The first consists in inserting the bond-slip layer as a separate element between a concrete and a steel element. However, the second approach has been chosen, in which the bond-slip element and the reinforcement element are combined. After Section 2.2, the present report is concerned only with this combined element, which, for the sake of convenience, will be referred to merely as the “bond-slip element”, even though this is in fact an incomplete designation for it.

2.2 Combining the bond-slip element with the reinforcement element

In this study reported here, the bond-slip element has been combined with the element for the reinforcing bar. The behaviour of the bond-slip element is determined by two degrees of freedom, namely, Δu and Δw , while the element for the bar likewise has two degrees of freedom, namely, the longitudinal strain ε_a and the radial strain ε_r . In the combined element the degrees of freedom Δw and ε_r are united in the degree of freedom Δv , so that three degrees of freedom remain. As indicated in Fig. 2.5, this combination is expressed by:

$$\Delta v = \Delta w + r \varepsilon_r \quad (2.16)$$

Since the following expression is valid for ε_r :

$$\varepsilon_r = (1 - \nu_s) \frac{\sigma_r}{E_s} - \nu_s \frac{\sigma_a}{E_s} \quad (2.17)$$

and since:

$$\varepsilon_a = \frac{\sigma_a}{E_s} - 2\nu_s \frac{\sigma_r}{E_s} \quad (2.18)$$

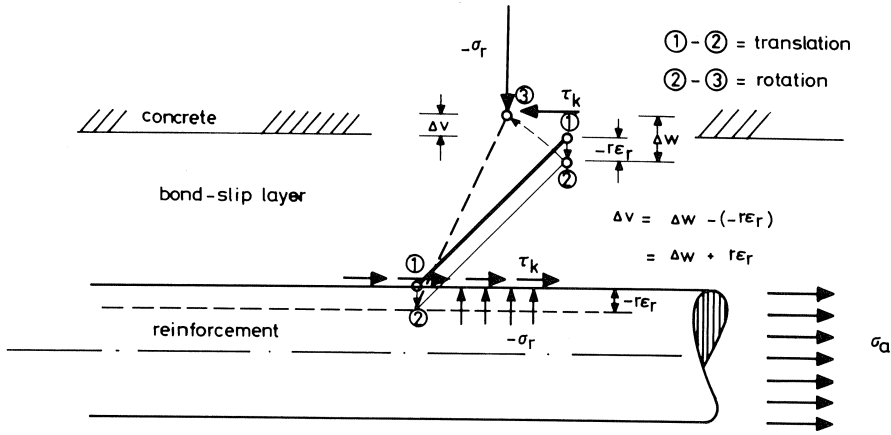


Fig. 2.5. The rebar element and the bond-slip element are connected.

ϵ_r can alternatively be written as follows:

$$\epsilon_r = \frac{(1 + v_s)(1 - 2v_s)\sigma_r}{E_s} - v_s \epsilon_a \quad (2.19)$$

Equation (2.16) can now be put in the following form:

$$\Delta w = \Delta v - \frac{r(1 + v_s)(1 - 2v_s)\sigma_r}{E_s} + rv_s \epsilon_a \quad (2.20)$$

Equation (2.9) thus becomes:

$$\sigma_r = C_2(rv_s \epsilon_a - k \Delta u + \Delta v) \quad (2.21)$$

where C_2 is:

$$C_2 = \frac{1}{\frac{\beta r}{E_l \cos^3 \varphi} + \frac{r(1 + v_s)(1 - 2v_s)}{E_s}} \quad (2.22)$$

For the sake of simplification this relationship will, in the further treatment of the subject, be approximated by:

$$C_2 = \alpha \frac{E_s}{r} \quad (2.23)$$

In this simplified relationship the coefficient α depends mainly on the quality and thickness of the boundary layer around the reinforcing bar. Hence this coefficient α is to be regarded as a kind of layer thickness coefficient. Its order of magnitude is found to be 0.5-1.

For τ_k is obtained from equations (2.12) and (2.21):

$$\tau_k = C_2(-krv_s \epsilon_a + k^2 \Delta u - k \Delta v) \quad (2.24)$$

On addition of equations (2.24) and (2.1) the total shear stress is found:

$$\tau = C_2(-k v_s \varepsilon_a + k^2 \Delta u - k \Delta v) + S \Delta u \quad (2.25)$$

Finally, from equations (2.18) and (2.21):

$$\sigma_a = E_s \varepsilon_a + 2C_2(v_s^2 r \varepsilon_a - v_s k \Delta u + v_s \Delta v) \quad (2.26)$$

In summarized form the equations (2.26), (2.25) and (2.21) can be written as:

$$\begin{bmatrix} \sigma_a \\ \tau \\ \sigma_r \end{bmatrix} = \begin{bmatrix} \frac{2E_s}{r} & 0 & 0 \\ 0 & S & 0 \\ 0 & 0 & 0 \end{bmatrix} \cdot \begin{bmatrix} \frac{\varepsilon_a r}{2} \\ \Delta u \\ \Delta v \end{bmatrix} + C_2 \begin{bmatrix} 4v_s^2 & -2kv_s & 2v_s \\ -2kv_s & k^2 & -k \\ 2v_s & -k & 1 \end{bmatrix} \cdot \begin{bmatrix} \frac{\varepsilon_a r}{2} \\ \Delta u \\ \Delta v \end{bmatrix} \quad (2.27)$$

In the vector comprising strains the product $\varepsilon_a r/2$ is employed in lieu of ε_a . This has been done in connection with determining the variation of the internal work, which will later take place implicitly in establishing the stiffness matrix of the element.

For this variation the following expression holds:

$$\delta A_{vv} = \int_V \sigma_a \delta \varepsilon_a dV + \int_A (\tau \delta \Delta u + \sigma_r \delta \Delta v) dA \quad (2.28)$$

This can alternatively be written as follows:

$$\delta A_{vv} = \int_A \left(\sigma_a \delta \frac{\varepsilon_a r}{2} + \tau \delta \Delta u + \sigma_r \delta \Delta v \right) dA \quad (2.29)$$

which becomes apparent on considering that for a circular section with radius r :

$$A = 2\pi r \int_0^l dx \quad \text{and} \quad V = \pi r^2 \int_0^l dx \quad \text{so that:} \quad V = \frac{r}{2} A$$

Equation (2.27) can be written in the following shorter form:

$$\begin{bmatrix} \sigma_a \\ \tau \\ \sigma_r \end{bmatrix} = \begin{bmatrix} C_4 & -C_5 & C_6 \\ -C_5 & C_1 & -C_3 \\ C_6 & -C_3 & C_2 \end{bmatrix} \times \begin{bmatrix} \frac{\varepsilon_a r}{2} \\ \Delta u \\ \Delta v \end{bmatrix} \quad (2.30)$$

or in abbreviated notation:

$$\mathbf{\tau} = \mathbf{C} \Delta \mathbf{u}$$

where:

$$C_1 = S + k^2 C_2 = S + k C_3 \quad (2.31)$$

$$C_2 = \alpha \frac{E_s}{r} \quad (2.23)$$

$$C_3 = k C_2 \quad (2.32)$$

$$C_4 = \frac{2E_s}{r} + 4v_s^2 C_2 = \frac{2E_s}{r} (1 + 2av_s^2) \quad (2.33)$$

$$C_5 = 2kv_s C_2 \quad (2.34)$$

$$C_6 = 2v_s C_2 \quad (2.35)$$

As already stated, in these formulas the rib factor k represents the effect of the “deformity” (ribbed surface configuration) of the bar, i.e., mechanical interlocking.

2.3 Further elaboration

The components for establishing the element stiffness matrix of the combined bond-slip element (including the reinforcing bar) are now ready. In the now following section of this article it will briefly be shown how this is done. More particularly, this will relate to the axially symmetric 6-node bond-slip element which is represented in Fig. 2.6b and is compatible with the axially symmetric 8-node concrete element represented in Fig. 2.6a. The bond-slip element is numerically integrated, using Gauss’s method.* The integration points employed for the purpose will accordingly be referred to as Gauss points in this article.

The interpolation polynomial* for the displacements has been chosen as follows:

$$\begin{aligned} N_1 &= -\frac{1}{2}\xi(1 - \xi) \\ N_2 &= (1 - \xi^2) \\ N_3 &= \frac{1}{2}\xi(1 + \xi) \end{aligned} \quad (2.36)$$

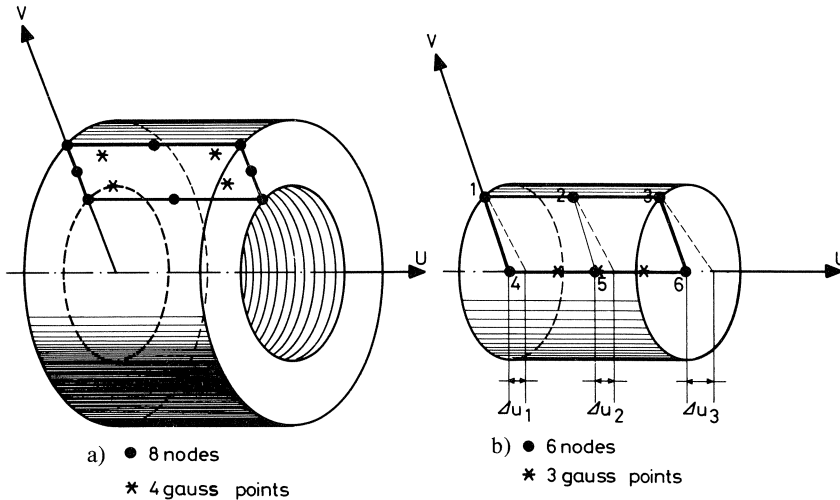


Fig. 2.6. Axially symmetric elements.
a. concrete element
b. bond-slip element

* For an explanation of this concept see, for example, [18].

This means that for the strains the following derivatives are used for interpolation:

$$\begin{aligned}\frac{dN_1}{d\xi} &= \xi - \frac{1}{2} \\ \frac{dN_2}{d\xi} &= -2\xi \\ \frac{dN_3}{d\xi} &= \xi + \frac{1}{2}\end{aligned}\tag{2.37}$$

From these equations it is possible to calculate dN_i/dx by multiplication of $dN_i/d\xi$ and $d\xi/dx$ where $d\xi/dx$ follows from equation (2.46).

The generalized strains – i.e., the strains that determine the internal stresses – can thus be expressed in the nodal displacements:

$$\begin{bmatrix} \frac{\varepsilon_a r}{2} \\ \Delta u \\ \Delta v \end{bmatrix} = \begin{bmatrix} 0 & 0 & 0 & \frac{r}{2} \frac{dN_1}{dx} & \frac{r}{2} \frac{dN_2}{dx} & \frac{r}{2} \frac{dN_3}{dx} & 0 & 0 & 0 \\ -N_1 & -N_2 & -N_3 & N_1 & N_2 & N_3 & 0 & 0 & 0 \\ 0 & 0 & 0 & 0 & 0 & 0 & N_1 & N_2 & N_3 \end{bmatrix} \cdot \begin{bmatrix} u_1 \\ u_m \\ u_6 \\ v_1 \\ v_2 \\ v_3 \end{bmatrix}\tag{2.38}$$

or in abbreviated notation:

$$\Delta \mathbf{u} = \mathbf{B} \mathbf{u}^e$$

The correctness of the above relationship is apparent, inter alia, from Fig. 2.6b, from which it is seen that the following relations are valid for the slip Δu :

$$\begin{aligned}\Delta u_1 &= u_4 - u_1 \\ \Delta u_2 &= u_5 - u_2 \\ \Delta u_3 &= u_6 - u_3\end{aligned}\tag{2.39}$$

The displacements v_4 to v_6 of the nodes 4 to 6 need not occur in the system, since they are zero anyway on account of the axial symmetry.

The steel strain ε_a depends only on the displacements u_4 to u_6 , in accordance with:

$$\varepsilon_a = \frac{du}{dx}\tag{2.40}$$

where:

$$\frac{du}{dx} = \frac{dN_1}{dx} u_4 + \frac{dN_2}{dx} u_5 + \frac{dN_3}{dx} u_6\tag{2.41}$$

The element stiffness matrix \mathbf{S}^e now follows from the matrix \mathbf{C} defined in equation (2.30) and from the matrix \mathbf{B} in equation (2.38). It is expressed by:

$$\mathbf{S}^e = \int_A \mathbf{B}^T \mathbf{C} \mathbf{B} d(A)\tag{2.42}$$

where:

$$\text{so that: } d(A) = 2\pi r dx \quad (2.43)$$

$$\mathbf{S}^e = 2\pi r \int_{x=x_1}^{x=x_3} \mathbf{B}^T \mathbf{C} \mathbf{B} dx \quad (2.44)$$

which can alternatively be written:

$$\mathbf{S}^e = 2\pi r \int_{\xi=-1}^{\xi=1} \mathbf{B}^T \mathbf{C} \mathbf{B} \frac{dx}{d\xi} d\xi \quad (2.45)$$

In this equation $dx/d\xi$ follows from:

$$\frac{dx}{d\xi} = \frac{\partial N_1}{\partial \xi} x_4 + \frac{\partial N_2}{\partial \xi} x_5 + \frac{\partial N_3}{\partial \xi} x_6 \quad (2.46)$$

Next, the overall stiffness matrix for the structure to be analysed can be compiled in the usual way. How this has been arranged in the DIANA program package need not be further described here.

2.4 Tying

The model that has been developed up to this point does, however, still suffer from a small practical drawback, which will be explained with the aid of Fig. 2.7. This diagram shows part of a reinforcing bar (length dx) on which is acting a shear stress τ that brings about a reduction of the axial stress σ_a . The following relation applies:

$$\tau(2\pi r dx) = d\sigma_a (\pi r^2)$$

or:

$$\tau = \frac{1}{2} r \frac{d\sigma_a}{dx} \quad (2.47)$$

The shear stress is therefore proportional to the derivative of the normal stress. In the element under consideration a quadratic distribution of the displacement field is assumed, so that a linear distribution of the strain and thus also of the axial stress σ_a occurs. The associated shear stress is therefore constant according to equation (2.47). This is not in agreement with what is stated by equation (2.30):

$$\tau = -C_5 \frac{\varepsilon_a r}{2} + C_1 \Delta u - C_3 \Delta v$$

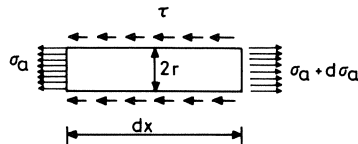


Fig. 2.7. Relation between σ_a and τ .

In this expression τ is mainly dependent on Δu and Δv , which display quadratic behaviour while only a minor portion displays linear behaviour as a function of ε_a .

This discrepancy can be dealt with by the application of so-called tyings. By this is understood the possibility offered by DIANA to make a degree of freedom linearly dependent on a certain number of other degrees of freedom. The tyings introduced are then, first:

$$\Delta u_2 = \frac{1}{2}(\Delta u_1 + \Delta u_3) \quad (2.48)$$

or according to equation (2.39):

$$u_2 = u_5 + \frac{1}{2}u_1 - \frac{1}{2}u_4 + \frac{1}{2}u_3 - \frac{1}{2}u_6 \quad (2.49)$$

and second:

$$\Delta v_2 = \frac{1}{2}(\Delta v_1 + \Delta v_3) \quad (2.50)$$

or:

$$v_2 = v_5 + \frac{1}{2}v_1 - \frac{1}{2}v_4 + \frac{1}{2}v_3 - \frac{1}{2}v_6 \quad (2.51)$$

Since v_4 to v_6 are zero, the last-mentioned equation can be written as follows:

$$v_2 = \frac{1}{2}v_1 + \frac{1}{2}v_3 \quad (2.52)$$

The effect of applying the tyings indicated above is that now Δu and Δv , and therefore v , behave linearly, just as ε_a does, so that there is no longer any discrepancy in equation (2.30). The discrepancy with equation (2.47) still exists, though to a reduced extent (constant versus linear behaviour). There is, however, nothing more that can be done to remedy the matter, since the phenomenon in question is inherent in the finite element method. With increasing refinement of the elements employed, the drawbacks associated with this effect will become less and less noticeable, anyway.

3 Constructing the model for the 3D element

3.1 General

In order to be able to analyse specimens not of axially symmetric shape, a bond-slip element as shown in Fig. 3.1 is proposed. Instead of the radial stress σ_r , such as that acting upon the axially symmetric element, there are now the stresses σ_{xa} , σ_{xb} , σ_{ya} and σ_{yb} acting upon the element, as shown at cross-section 3 in Fig. 3.1. The element comprises 15 nodes and a total of 45 degrees of freedom. A number of these degrees of freedom can in fact be dispensed with; they are indicated by the dotted arrows in Fig. 3.1. In DIANA these are expressed, with the aid of tyings, in the other degrees of freedom. The tyings result in the following relations:

$$\begin{aligned} v_{x1} &= v_{x2}; & v_{x6} &= v_{x7}; & v_{x11} &= v_{x12} \\ v_{x4} &= v_{x3}; & v_{x9} &= v_{x8}; & v_{x14} &= v_{x13} \\ v_{y3} &= v_{y2}; & v_{y8} &= v_{y7}; & v_{y13} &= v_{y12} \\ v_{y4} &= v_{y1}; & v_{y9} &= v_{y6}; & v_{y14} &= v_{y11} \end{aligned} \quad (3.1)$$

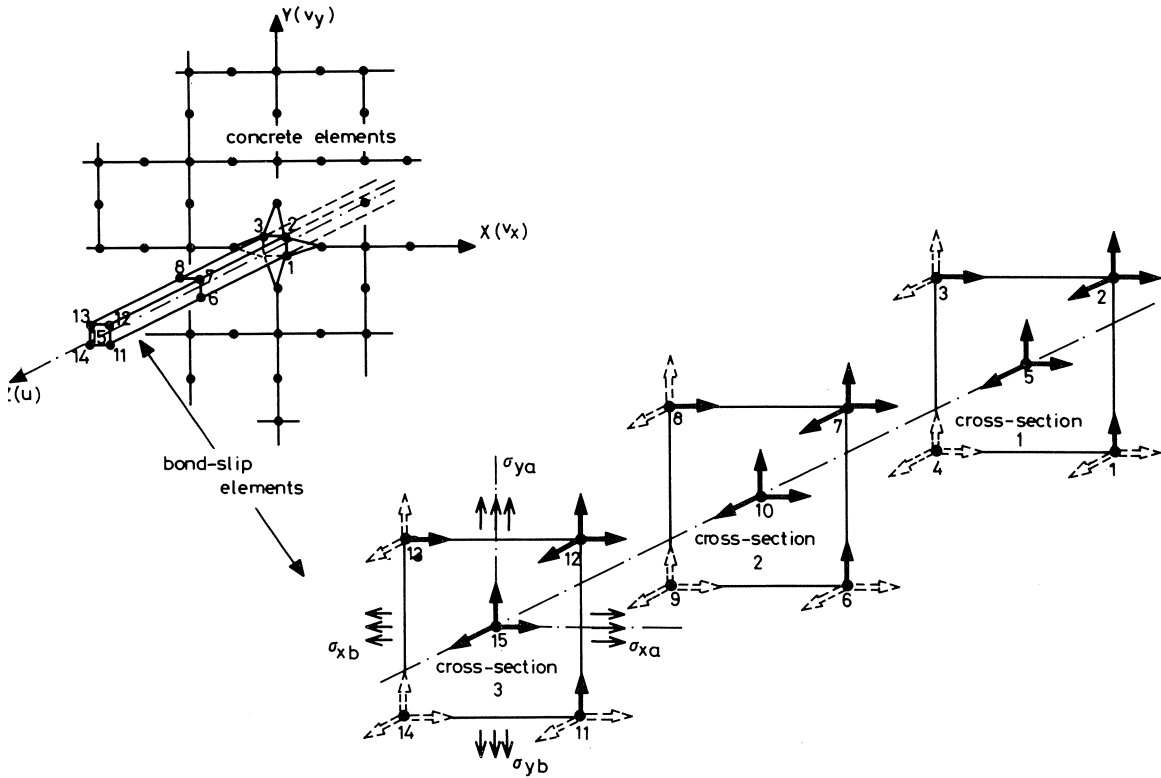


Fig. 3.1. Three-dimensional (3D) bond-slip element.

$$\begin{aligned}
 u_1 &= u_3 = u_4 = u_2 \\
 u_6 &= u_8 = u_9 = u_7 \\
 u_{11} &= u_{13} = u_{14} = u_{12}
 \end{aligned} \tag{3.2}$$

Furthermore, in analogy with equation (2.39):

$$\begin{aligned}
 u_7 &= u_{10} - \frac{1}{2}u_5 + \frac{1}{2}u_2 - \frac{1}{2}u_{15} + \frac{1}{2}u_{12} \\
 v_{x7} &= v_{x10} - \frac{1}{2}v_{x5} + \frac{1}{2}v_{x2} - \frac{1}{2}v_{x15} + \frac{1}{2}v_{x12} \\
 v_{y7} &= v_{y10} - \frac{1}{2}v_{y5} + \frac{1}{2}v_{y2} - \frac{1}{2}v_{y15} + \frac{1}{2}v_{y12}
 \end{aligned} \tag{3.3}$$

Finally there are the tyings:

$$\begin{aligned}
 v_{x5} &= \frac{1}{2}(v_{x2} + v_{x3}); & v_{x10} &= \frac{1}{2}(v_{x7} + v_{x8}); & v_{x15} &= \frac{1}{2}(v_{x12} + v_{x13}) \\
 v_{y5} &= \frac{1}{2}(v_{y1} + v_{y2}); & v_{y10} &= \frac{1}{2}(v_{y6} + v_{y7}); & v_{y15} &= \frac{1}{2}(v_{y11} + v_{y12})
 \end{aligned} \tag{3.4}$$

which are applicable only if there are no stirrups. If stirrups are employed, a number of the last-mentioned tyings can be discarded. As a result of the presence of a stirrup, which can likewise be conceived as a bond-slip element, the relations $\sigma_{xa} = \sigma_{xb}$ and $\sigma_{ya} = \sigma_{yb}$ no longer apply. This is exemplified by Fig. 3.2, which relates to, for instance,

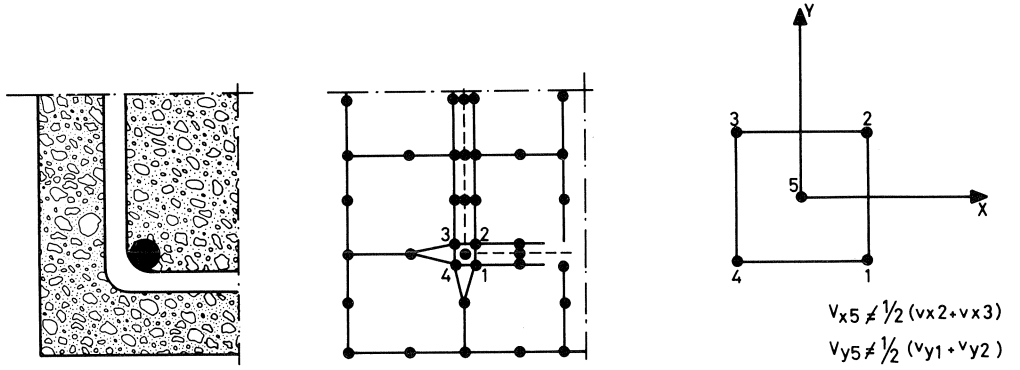


Fig. 3.2. If stirrups are installed, tyings are dispensed with.

cross-section 1 in Fig. 3.1. Owing to the stirrup being present, the following tyings are dispensed with:

$$v_{x5} = \frac{1}{2}(v_{x2} + v_{x3})$$

and:

$$v_{y5} = \frac{1}{2}(v_{y1} + v_{y2})$$

The extension of the axially symmetric element to the 3D element consists in replacing equation (2.30) by:

$$\begin{bmatrix} 4\sigma_a \\ 4\tau \\ \sigma_{xa} \\ \sigma_{xb} \\ \sigma_{ya} \\ \sigma_{yb} \end{bmatrix} = \begin{bmatrix} 4C_4 & -4C_5 & C_6 & C_6 & C_6 & C_6 \\ -4C_5 & 4C_1 & -C_3 & -C_3 & -C_3 & -C_3 \\ C_6 & -C_3 & C_2 & 0 & 0 & 0 \\ C_6 & -C_3 & 0 & C_2 & 0 & 0 \\ C_6 & -C_3 & 0 & 0 & C_2 & 0 \\ C_6 & -C_3 & 0 & 0 & 0 & C_2 \end{bmatrix} \cdot \begin{bmatrix} \frac{\epsilon_a r}{2} \\ \Delta u \\ \Delta v_{xa} \\ \Delta v_{xb} \\ \Delta v_{ya} \\ \Delta v_{yb} \end{bmatrix} \quad (3.5)$$

or in abbreviated notation:

$$\mathbf{t} = \mathbf{C} \Delta \mathbf{u}$$

where C_1 to C_6 have the same meaning as in equation (2.30).

3.2 Element stiffness matrix

The generalized strains conform to the following relation, established in analogy with equation (2.38):

$$\begin{bmatrix} \frac{\varepsilon_a r}{2} \\ \Delta u \\ \Delta v_{xa} \\ \Delta v_{xb} \\ \Delta v_{ya} \\ \Delta v_{yb} \end{bmatrix} = \begin{bmatrix} \mathbf{B}_{11} & \mathbf{B}_{12} & \mathbf{B}_{13} & 0 & 0 & 0 & 0 & 0 & 0 \\ \mathbf{B}_{21} & \mathbf{B}_{22} & \mathbf{B}_{23} & 0 & 0 & 0 & 0 & 0 & 0 \\ 0 & 0 & 0 & \mathbf{B}_{31} & \mathbf{B}_{32} & \mathbf{B}_{33} & 0 & 0 & 0 \\ 0 & 0 & 0 & \mathbf{B}_{41} & \mathbf{B}_{42} & \mathbf{B}_{43} & 0 & 0 & 0 \\ 0 & 0 & 0 & 0 & 0 & 0 & \mathbf{B}_{51} & \mathbf{B}_{52} & \mathbf{B}_{53} \\ 0 & 0 & 0 & 0 & 0 & 0 & \mathbf{B}_{61} & \mathbf{B}_{62} & \mathbf{B}_{63} \end{bmatrix} \times \begin{bmatrix} u_1 \\ \vdots \\ u_{15} \\ v_{x1} \\ \vdots \\ v_{x15} \\ v_{y1} \\ \vdots \\ v_{y15} \end{bmatrix} \quad (3.6)$$

or:

$$\Delta \mathbf{u} = \mathbf{B} \mathbf{u}^e$$

where, for $i = 1, 2, 3$:

$$\mathbf{B}_{1i} = \begin{bmatrix} 0 & 0 & 0 & 0 & \frac{r}{2} \frac{dN_i}{dz} \end{bmatrix} \quad (3.7)$$

$$\mathbf{B}_{2i} = \begin{bmatrix} -\frac{N_i}{4} & -\frac{N_i}{4} & -\frac{N_i}{4} & -\frac{N_i}{4} & N_i \end{bmatrix} \quad (3.8)$$

$$\mathbf{B}_{3i} = \begin{bmatrix} \frac{N_i}{2} & \frac{N_i}{2} & 0 & 0 & -N_i \end{bmatrix} \quad (3.9)$$

$$\mathbf{B}_{4i} = \begin{bmatrix} 0 & 0 & -\frac{N_i}{2} & -\frac{N_i}{2} & N_i \end{bmatrix} \quad (3.10)$$

$$\mathbf{B}_{5i} = \begin{bmatrix} 0 & \frac{N_i}{2} & \frac{N_i}{2} & 0 & -N_i \end{bmatrix} \quad (3.11)$$

$$\mathbf{B}_{6i} = \begin{bmatrix} -\frac{N_i}{2} & 0 & 0 & -\frac{N_i}{2} & N_i \end{bmatrix} \quad (3.12)$$

In analogy with equation (2.45) the element stiffness matrix can now be written as follows:

$$\boxed{S^e = \frac{1}{2}\pi r \int_{\xi=-1}^{\xi=+1} \mathbf{B}^T \mathbf{C} \mathbf{B} \frac{dz}{d\xi} d\xi} \quad (3.13)$$

In this relation the integral sign is preceded by the factor $\frac{1}{2}\pi$ instead of 2π as in equation (2.45), i.e., there is a difference amounting to a factor 4.

On putting $\sigma_{xa} = \sigma_{xb} = \sigma_{ya} = \sigma_{yb} = \sigma_r$ in equation (3.13), it will appear that this factor 4 is exactly compensated in the expression $\mathbf{B}^T \mathbf{C} \mathbf{B}$.

It should further be noted that the following expression holds for $dz/d\xi$:

$$\frac{dz}{d\xi} = \frac{dN_1}{d\xi} z_5 + \frac{dN_2}{d\xi} z_{10} + \frac{dN_3}{d\xi} z_{15} \quad (3.14)$$

With the information now available there is no problem in establishing the \mathbf{S}^e matrix. Besides, the further treatment within the wider context is to be regarded as a familiar standard problem. All the same, the following general comments are of importance with a view to ensuring a satisfactory procedure.

3.3 Physical thickness of reinforcing bar

In the case of the axially symmetric element the physical thickness of the reinforcing bar can simply be deducted from the dimension of the adjacent concrete element in establishing the co-ordinates. In the model proposed here, however, this approach runs into difficulties, and for this reason the dimension of the bar must, in so far as the concrete is concerned, be neglected. Hence, for each cross-section, the nodes will have the same x, y and z co-ordinates. Of course, the bar thickness does play a part in the analysis by virtue of the radius r occurring in equation (3.13).

3.4 Symmetry

In the model it is possible to take advantage of symmetry, so that only a quarter of the section need be considered, as is indicated in Fig. 3.3. The number of degrees of freedom is thus greatly reduced in comparison with the general case envisaged in Fig. 3.1. The number of tyings is also much smaller. There then remains of the equations (3.1), (3.2) and (3.4):

$$v_{x1} = v_{y1} = v_{x3} = v_{y3} = v_{x5} = v_{y5} = 0 \quad (3.15)$$

while the equations (3.3) become:

$$\begin{aligned} u_4 &= u_3 - \frac{1}{2}u_1 + \frac{1}{2}u_2 - \frac{1}{2}u_5 + \frac{1}{2}u_6 \\ v_{x4} &= \frac{1}{2}(v_{x2} + v_{x6}) \\ v_{y4} &= \frac{1}{2}(v_{y2} + v_{y6}) \end{aligned} \quad (3.16)$$

For the general 3D case equation (3.5.) is now simplified to:

$$\begin{bmatrix} 2\sigma_a \\ 2r \\ \sigma_x \\ \sigma_y \end{bmatrix} = \begin{bmatrix} 2C_4 & -2C_5 & C_6 & C_6 \\ -2C_5 & 2C_1 & -C_3 & -C_3 \\ C_6 & -C_3 & C_2 & 0 \\ C_6 & -C_3 & 0 & C_2 \end{bmatrix} \times \begin{bmatrix} \frac{\epsilon_a r}{2} \\ \Delta u \\ \Delta v_x \\ \Delta v_y \end{bmatrix} \quad (3.17)$$

or in abbreviated form:

$$\mathbf{r} = \mathbf{C} \Delta \mathbf{u}$$

while equation (3.14) can be written as:

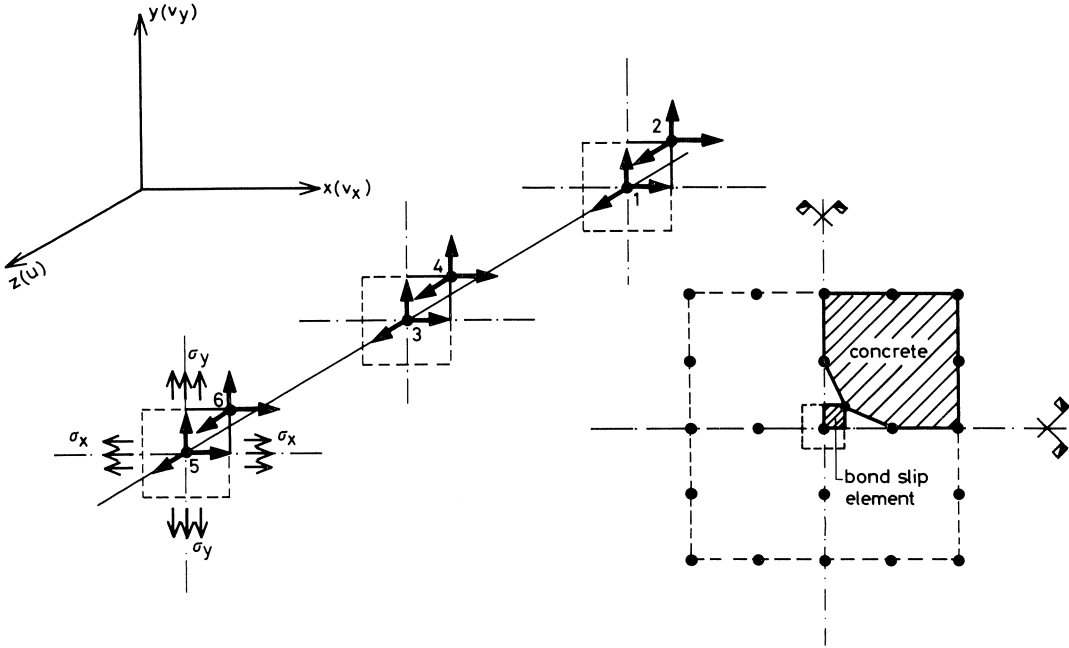


Fig. 3.3. Symmetric 3D element.

$$\frac{dz}{d\zeta} = \frac{dN_1}{d\zeta} z_1 + \frac{dN_2}{d\zeta} z_3 + \frac{dN_3}{d\zeta} z_5 \quad (3.18)$$

Equation (3.6) can be simplified to:

$$\begin{bmatrix} \frac{\varepsilon_a r}{2} \\ \Delta u \\ \Delta v_x \\ \Delta v_y \end{bmatrix} = \begin{bmatrix} \mathbf{B}_1 & 0 & 0 \\ \mathbf{B}_2 & 0 & 0 \\ 0 & \mathbf{B}_3 & 0 \\ 0 & 0 & \mathbf{B}_4 \end{bmatrix} \times \begin{bmatrix} u_1 \\ \vdots \\ u_6 \\ \Delta v_{x1} \\ \vdots \\ \Delta v_{x6} \\ \Delta v_{y1} \\ \vdots \\ \Delta v_{y6} \end{bmatrix} \quad (3.19)$$

where:

$$\mathbf{B}_1 = \begin{bmatrix} \frac{r}{2} \frac{dN_1}{dz} & 0 & \frac{r}{2} \frac{dN_2}{dz} & 0 & \frac{r}{2} \frac{dN_3}{dz} & 0 \end{bmatrix} \quad (3.20)$$

$$\mathbf{B}_2 = \begin{bmatrix} N_1 & -N_1 & N_2 & -N_2 & N_3 & -N_3 \end{bmatrix} \quad (3.21)$$

$$\mathbf{B}_3 = \begin{bmatrix} -N_1 & N_1 & -N_2 & N_2 & -N_3 & N_3 \end{bmatrix} \quad (3.22)$$

$$\mathbf{B}_4 = \begin{bmatrix} -N_1 & N_1 & -N_2 & N_2 & -N_3 & N_3 \end{bmatrix} \quad (3.23)$$

In determining the stiffness matrix by:

$$S^e = \frac{1}{2} \int_A \mathbf{B}^T \mathbf{C} \mathbf{B} d(A) \quad (3.24)$$

in which relation the factor $\frac{1}{2}$ compensates the factors 2 in equation (3.17), it should be borne in mind that $d(A)$ now does not follow from equation (2.43). This is because only a quarter of the section is considered, so that:

$$d(A) = \frac{1}{2} \pi r dx \quad (3.25)$$

This yields the following expression:

$$S^e = \frac{1}{4} \pi r \int_{\xi=-1}^{\xi=+1} \mathbf{B}^T \mathbf{C} \mathbf{B} \frac{dz}{d\xi} d\xi \quad (3.26)$$

The further elaboration resulting in the overall stiffness matrix for the structure to be analysed can be done in the usual way.

4 Some general supplementary matters

As yet, nothing has been said about three drawbacks associated with the mathematical model of which the several variants have been discussed in the foregoing. These drawbacks will now be indicated, and it will also be explained how they can be overcome. They are successively:

- delimitation of the r - Δ relation;
- algebraic sign of k dependent on the direction of slip;
- radial tension.

4.1 Delimitation of the r - Δ relation

In the treatment of the subject so far, attention has mainly been focused on the formulation of the rising branch of the r - Δ relation, resulting in equation (3.5). For formulating the second branch, which forms the upper bound of equation (3.5), a variant of this equation may be employed, which is obtained by replacement of Δu by Δu_{\max} , as a result of which the following relation is arrived at:

$$\begin{bmatrix} 4\sigma_a \\ 4r \\ \sigma_{xa} \\ \sigma_{xb} \\ \sigma_{ya} \\ \sigma_{yb} \end{bmatrix} = \begin{bmatrix} 4C_4 & -4C_5 & C_6 & C_6 & C_6 & C_6 \\ -4C_5 & 4C_1 & -C_3 & -C_3 & -C_3 & -C_3 \\ C_6 & -C_3 & C_2 & 0 & 0 & 0 \\ C_6 & -C_3 & 0 & C_2 & 0 & 0 \\ C_6 & -C_3 & 0 & 0 & C_2 & 0 \\ C_6 & -C_3 & 0 & 0 & 0 & C_2 \end{bmatrix} \times \begin{bmatrix} \frac{\varepsilon_a r}{2} \\ \Delta u_{\max} \\ \Delta v_{xa} \\ \Delta v_{xb} \\ \Delta v_{ya} \\ \Delta v_{yb} \end{bmatrix} \quad (4.1)$$

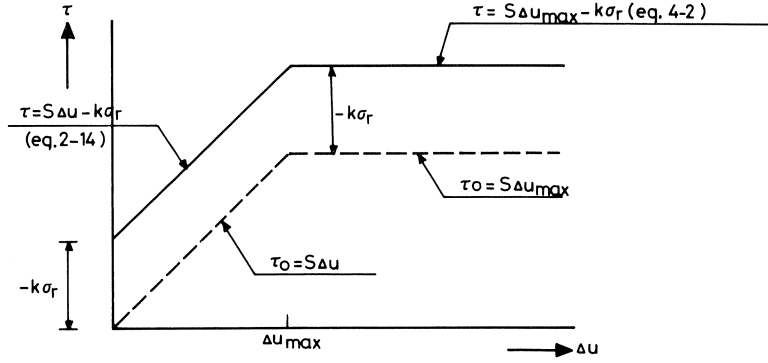


Fig. 4.1. τ - Δu -relation for an axially symmetric element for a constant value of σ_r .

In order to satisfy this relation in the analysis, an iterative computational process is required, in connection with which the difference between the stresses found in the analysis and the stresses as determined by equation (4.1) is eliminated with so-called unbalanced stresses. For an explanation of the procedure associated with the application of unbalanced stresses, see for example [18].

The computational use of equation (4.1) can, for an axially symmetric element, be illustrated in a conveniently simple manner for the special case where σ_r is constant. This is shown in Fig. 4.1, for which equation (2.14) has been used; when Δu_{\max} is exceeded, this equation is replaced by:

$$\tau = S \Delta u_{\max} - k \sigma_r \quad (4.2)$$

The model is, incidentally, still open to the objection that it is what is known as hyper-elastic, which means that the same relation is adopted for loading and for unloading. Since elasto-plastic behaviour is assumed for the concrete and steel themselves, ideal interadjustment has not yet been achieved.

However, for the test specimens envisaged in the present article, the above-mentioned objection did not cause any difficulty. This is because the reversal of loading direction due to cracking right through the specimen occurs in the elastic range of behaviour, for which $\Delta u < \Delta u_{\max}$. In future, when alternating load conditions are also considered, however, this objection will certainly have to receive attention.

4.2 Algebraic sign of the rib factor k

The model as so far described is "direction-sensitive". This is exemplified by the axially symmetric test specimens shown in Fig. 4.2, for which, according to equation (2.14), the relation between the radial stress σ_r and the shear stress τ is:

$$\tau = S \Delta u - k \sigma_r \quad (2.14)$$

If the specimen is rotated through 180 degrees, so that τ and Δu change their signs, the

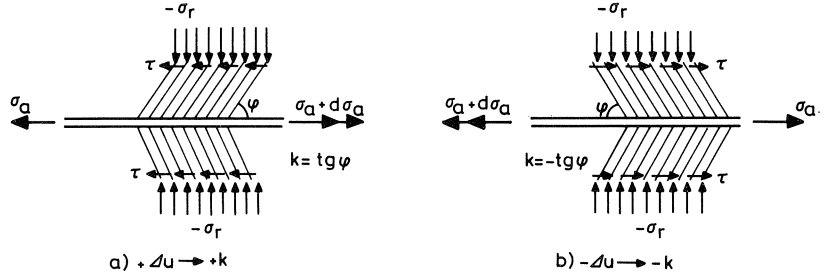


Fig. 4.2. Sign of k depends on the sign of Δu .

rib factor k will also have to undergo a change of sign, since the physical behaviour of the specimen will remain unchanged. This means:

$$\tau = S \Delta u + k \sigma_r \quad (4.3)$$

The difference between equation (2.14) and equation (4.3) is shown in Fig. 4.3. Evidently, the direction of the slip Δu has to be known in advance in order to decide whether $-k$ to $+k$ must be adopted. This is the case only if the specimen is symmetrically shaped as in Fig. 4.4 and then only if there is no continuous crack at the plane of symmetry. Hence it is even now not possible to avoid employing a procedure involving unbalanced stresses.

This procedure could be as follows. In establishing the element stiffness matrix S^e a value $k=0$ is adopted. After the set of equations has been solved, the direction of the slip in the case where $k=0$ is known. Now, with the aid of unbalanced stresses, the correct magnitude of k is taken into account, in which case the direction is no longer a problem, since the direction of Δu is known. For low values of k (approx. 0.02) this procedure works satisfactorily, but difficulties are encountered for higher values of k (> 0.05). This is due to the fact that the S^e matrix based on $k=0$ is too flexible and gives rise to over-large initial estimates of the slip, as a result of which the occurrence of cracks in the concrete is wrongly inferred and convergence problems occur. It was found that these problems could be solved by not only putting $k=0$ in the equation which is

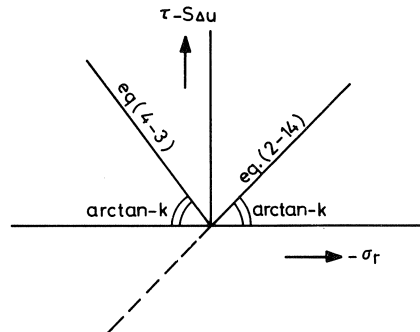


Fig. 4.3. Difference between equation (2.14) and equation (4.3).

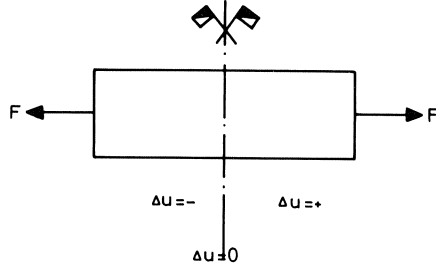


Fig. 4.4. For a symmetrical specimen the sign of Δu is known.

used for establishing the S^e matrix, but also replacing S by $S(1 + 50k)$, where of course k is now not taken as zero. The S^e matrix becomes stiffer in consequence. Equation (2.30) provides an example. For establishing the S^e matrix with which the stiffness of the structure is estimated, equation (2.30) corresponding to the axially symmetric case is replaced by:

$$\begin{bmatrix} \sigma_a \\ \tau \\ \sigma_r \end{bmatrix} = \begin{bmatrix} \frac{2E_s}{r}(1 + 2\alpha v_s^2) & 0 & 2v_s \frac{\alpha E_s}{r} \\ 0 & S(1 + 50k) & 0 \\ 2v_s \frac{\alpha E_s}{r} & 0 & \frac{\alpha E_s}{r} \end{bmatrix} \times \begin{bmatrix} \frac{\varepsilon_a r}{2} \\ \Delta u \\ \Delta v \end{bmatrix} \quad (4.4)$$

4.3 Radial tension

Besides the unbalanced stresses discussed in the two preceding sections of this chapter, unbalanced stresses are also introduced in the case where there is radial tension instead of radial compression.

It is in fact inconceivable that, with radial tension, a completely plain (“smooth-surfaced”) bar would offer more resistance to slip than a deformed (“ribbed”) bar would. Yet this is so according to equation (2.14), because for positive σ_r a lower value of τ is obtained with $k > 0$ than with $k = 0$. Just as in Section 4.2, k will have to change its sign. Since it is moreover questionable whether the absolute magnitude of k for radial compression is the same as for radial tension, it has been assumed, for the sake of simplicity, that $k = 0$ in the case where radial tension occurs. This means that in the axially symmetric model the relation represented in Fig. 4.5b is adopted instead of the original relation represented in Fig. 4.5a. Quite probably, a relation as indicated in Fig. 4.5c is in even better agreement with the actual behaviour. For the time being, however, this refinement has not been adopted, as it is not consistent with the accuracy of the assumptions for the other parameters in the model. Although Fig. 4.5 is valid only for the axially symmetric model (because σ_r is adopted here), it is evident that this procedure can also be applied to the general 3D element, for which equation (2.14) then becomes:

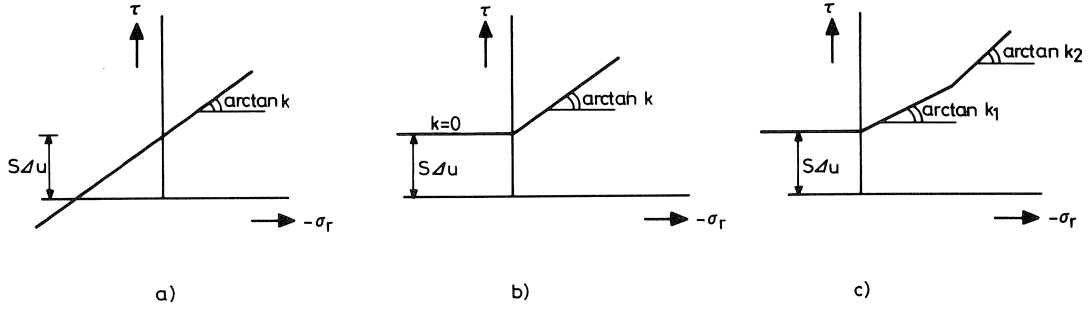


Fig. 4.5. Definition of k in the relation $\tau = S \Delta u - k \sigma_r$ (equation 2.14).

$$\tau = S \Delta u - \frac{1}{4} k_{xa} \sigma_{xa} - \frac{1}{4} k_{xb} \sigma_{xb} - \frac{1}{4} k_{ya} \sigma_{ya} - \frac{1}{4} k_{yb} \sigma_{yb} \quad (4.5)$$

where in principle:

$$k_{xa} = k_{xb} = k_{ya} = k_{yb} = k \quad (4.6)$$

As soon as it appears that σ_{xa} or σ_{xb} (etc.) is a tensile stress, the assumption $k_{xa} = 0$ or $k_{xb} = 0$ (etc.) is introduced.

5 Possible translation of 3D into 2D model

5.1 Introduction

To enable the results obtained with the 3D bond-slip element to be employed for a 2D analysis, a “translation” as envisaged in Fig. 5.1 will have to be carried out. Instead of being based on the discrete reinforcing bars shown in Fig. 5.1a, the analysis will then be based on a the steel strip shown in Fig. 5.1b and possessing the same total cross-sectional area as the bars. In this approach the steel area is therefore “smeared out”, as it were. In this chapter a possible procedure for such a translation will be considered, in connection with which it is necessary to bear in mind that any translation, however, sophisticated, will ultimately have to be verified with reference to comparative calculations in order to determine as correctly as possible the parameters adopted in performing it. For this reason it is advisable to keep the translation as simple as possible, with as few “translation parameters” as possible, but of course comprising the most important ones.

5.2 Derivation of formulas

The starting point of the translation is provided by:

$$\bar{\varepsilon}_a = \varepsilon_a \quad (5.1)$$

$$\Delta \bar{u} = \Delta u \quad (5.2)$$

$$\bar{\sigma}_a = \sigma_a \quad (5.3)$$

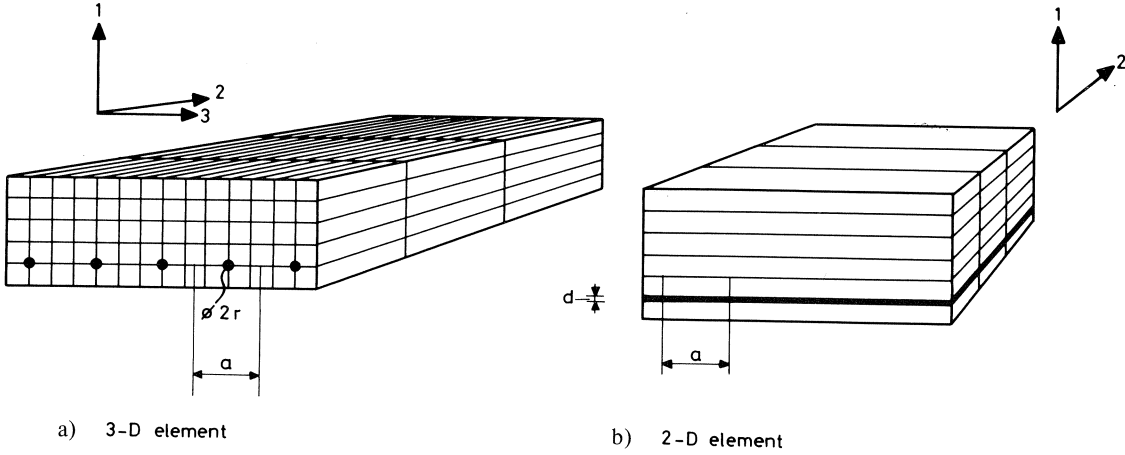


Fig. 5.1. Translation of 3D into 2D model.

In these equations the horizontal line over the symbols denotes that the variable in question relates to the 2D model. This notation will be adopted in the following treatment to distinguish these variables from those in the 3D model.

For the sake of convenience only a plain reinforcing bar will first be considered, i.e., the case $k=0$. Starting from an equal cross-sectional area for the reinforcement in the two models, this means that the area on which the shear stress acts is different. As Fig. 5.1 shows, for the cross-sectional area can be written:

$$A = \frac{1}{4}\pi r^2 = ad \quad (5.4)$$

so that the bond surface area per unit length is then:

$$A_{2D} = 2a = \frac{1}{2} \frac{\pi r^2}{d} \quad (5.5)$$

which is not equal to:

$$A_{3D} = 2\pi r \quad (5.6)$$

In order to ensure that the total shear force in the two models is equal, it is therefore necessary that:

$$\bar{\tau} = \frac{\pi r}{a} \tau \quad (5.7)$$

Since (still for $k=0$):

$$\tau = S \Delta u \quad (5.8)$$

it follows with equations (5.7) and (5.2) that:

$$\bar{\tau} = \frac{\pi r}{a} S \Delta \bar{u} \quad (5.9)$$

On furthermore defining:

$$\bar{S} = \frac{\pi r}{a} S \quad (5.10)$$

the following relation is finally obtained:

$$\bar{\tau} = \bar{S} \Delta \bar{u} \quad (5.11)$$

With the defining of \bar{S} the translation for the case $k = 0$ has been completed. Now before the other parameters needed for the deformed bar are translated, the definition of \bar{S} will be stated in a somewhat more general form, namely:

$$\boxed{\bar{S} = \frac{\beta \pi r}{a} S} \quad (5.12)$$

so that:

$$\boxed{\bar{\tau} = \frac{\beta \pi r}{a} \tau} \quad (5.13)$$

in which the coefficient β has been introduced in order to provide rather more freedom in effecting the translation. To start with, a value of β approximately equal to unity will of course first be considered. In the final numerical verification this value can then, if necessary, be suitably modified.

For the deformed reinforcing bar the following translational approach is found to yield a consistent whole:

$$\boxed{\bar{k} = k \sqrt{\frac{\beta \pi r}{a}}} \quad (5.14)$$

$$\boxed{\bar{v}_s = v_s \sqrt{\frac{\beta \pi r}{a}}} \quad (5.15)$$

Besides the above translation of material parameters, the following relations are valid for the displacements and stresses respectively:

$$\boxed{\Delta \bar{v}_{ya} = \Delta v_{ya} \sqrt{\frac{\beta \pi r}{a}}} \quad (5.16)$$

$$\boxed{\Delta \bar{v}_{yb} = \Delta v_{yb} \sqrt{\frac{\beta \pi r}{a}}} \quad (5.17)$$

$$\boxed{\bar{\sigma}_{ya} = \sigma_{ya} \sqrt{\frac{\beta \pi r}{a}}} \quad (5.18)$$

$$\boxed{\bar{\sigma}_{yb} = \sigma_{yb} \sqrt{\frac{\beta \pi r}{a}}} \quad (5.19)$$

In the 2D model the quantities Δv_{xa} , Δv_{xb} , σ_{xa} and σ_{xb} are of course absent.

Starting from equation (3.5) and assuming that $\Delta v_{xa} = \Delta v_{xb} = 0.5(\Delta v_{ya} + \Delta v_{yb})$ it is now possible, with the aid of the foregoing, to establish the following relation:

$$\begin{bmatrix} \frac{\beta\pi r}{a} \sigma_a \\ \bar{\mathbf{r}} \\ \frac{1}{2}\bar{\sigma}_{ya} \\ \frac{1}{2}\bar{\sigma}_{yb} \end{bmatrix} = \begin{bmatrix} \bar{C}_4 & -\bar{C}_5 & \frac{1}{2}\bar{C}_6 & \frac{1}{2}\bar{C}_6 \\ -\bar{C}_5 & \bar{C}_1 & -\frac{1}{2}\bar{C}_3 & -\frac{1}{2}\bar{C}_3 \\ \frac{1}{2}\bar{C}_6 & -\frac{1}{2}\bar{C}_3 & \frac{1}{2}\bar{C}_2 & 0 \\ \frac{1}{2}\bar{C}_6 & -\frac{1}{2}\bar{C}_3 & 0 & \frac{1}{2}\bar{C}_2 \end{bmatrix} \times \begin{bmatrix} \frac{\bar{\epsilon}_a r}{2} \\ \Delta \bar{\mathbf{u}} \\ \Delta \bar{v}_{ya} \\ \Delta \bar{v}_{yb} \end{bmatrix} \quad (5.20)$$

or in abbreviated form: $\bar{\mathbf{r}} = \bar{\mathbf{C}} \Delta \bar{\mathbf{u}}$

$$\bar{C}_1 = \bar{S} + k^2 \bar{C}_2 = (S + k^2 C_2) \frac{\beta\pi r}{a} = C_1 \frac{\beta\pi r}{a} \quad (5.21)$$

$$\bar{C}_2 = \frac{\alpha E_s}{r} = C_2 \quad (5.22)$$

$$\bar{C}_3 = k \bar{C}_2 = k C_2 \sqrt{\frac{\beta\pi r}{a}} = C_3 \sqrt{\frac{\beta\pi r}{a}} \quad (5.23)$$

$$\bar{C}_4 = 2 \frac{\beta\pi}{a} E_s + 4 \bar{v}_s^2 \bar{C}_2 = 2 \frac{\beta\pi}{a} E_s + 4 v_s^2 C_2 \frac{\beta\pi r}{a} = C_4 \frac{\beta\pi r}{a} \quad (5.24)$$

$$\bar{C}_5 = 2 k \bar{v}_s \bar{C}_2 = 2 k v_s C_2 \frac{\beta\pi r}{a} = C_5 \frac{\beta\pi r}{a} \quad (5.25)$$

$$\bar{C}_6 = 2 \bar{v}_s C_2 \sqrt{\frac{\beta\pi r}{a}} = C_6 \sqrt{\frac{\beta\pi r}{a}} \quad (5.26)$$

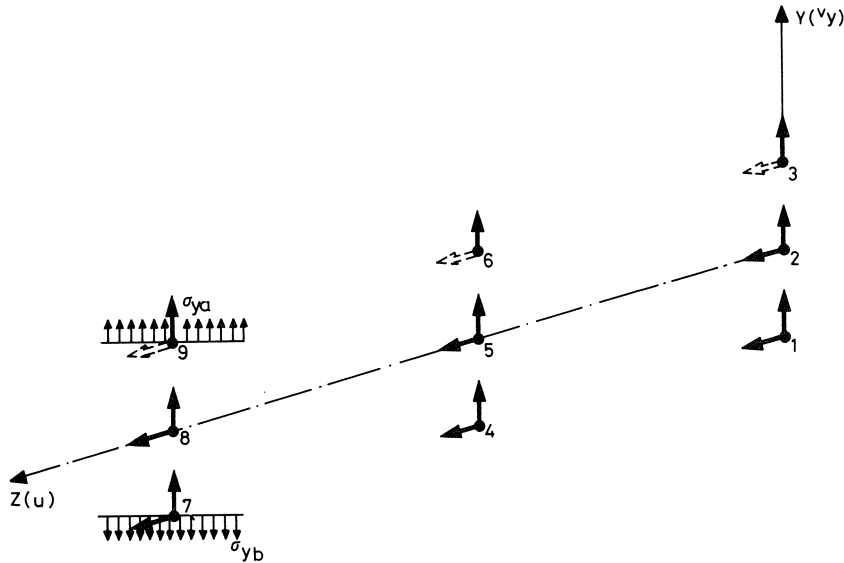


Fig. 5.2. Degrees of freedom in 2D bond-slip element.

Equation (5.20) relates to the 2D element shown in Fig. 5.2, of which the element stiffness matrix will be established in the next section of this chapter.

5.3 Element stiffness matrix

The generalized strains can, with the aid of the interpolation polynomials given in equations (2.36) and (2.37), be expressed in the nodal displacements as follows:

$$\begin{bmatrix} \frac{\bar{\epsilon}_a r}{2} \\ \Delta \bar{u} \\ \Delta \bar{v}_{ya} \\ \Delta \bar{v}_{yb} \end{bmatrix} = \begin{bmatrix} \mathbf{B}_{11} & \mathbf{B}_{12} & \mathbf{B}_{13} & 0 & 0 & 0 \\ \mathbf{B}_{21} & \mathbf{B}_{22} & \mathbf{B}_{23} & 0 & 0 & 0 \\ & & & \mathbf{B}_{31} & \mathbf{B}_{32} & \mathbf{B}_{33} \\ & & & \mathbf{B}_{41} & \mathbf{B}_{42} & \mathbf{B}_{43} \end{bmatrix} \times \begin{bmatrix} u_1 \\ \vdots \\ u_9 \\ v_1 \\ \vdots \\ v_9 \end{bmatrix}$$

or:

$$\Delta \bar{\mathbf{u}} = \mathbf{B} \mathbf{u}^e \quad (5.27)$$

where, for $i = 1, 2, 3$:

$$\mathbf{B}_{1i} = \begin{bmatrix} 0 & \frac{r}{2} \frac{dN_i}{dz} & 0 \end{bmatrix} \quad (5.28)$$

$$\mathbf{B}_{2i} = \begin{bmatrix} -N_i & N_i & 0 \end{bmatrix} \quad (5.29)$$

$$\mathbf{B}_{3i} = \begin{bmatrix} N_i & -N_i & 0 \end{bmatrix} \quad (5.30)$$

$$\mathbf{B}_{4i} = \begin{bmatrix} 0 & N_i & -N_i \end{bmatrix} \quad (5.31)$$

The stiffness matrix S^e is now:

$$S^e = \frac{1}{\beta} \int_A \mathbf{B}^T \bar{\mathbf{C}} \mathbf{B} d(A) \quad (5.32)$$

In which expression the factor $1/\beta$ compensates the factors β in equation (5.20) and where for an element of unit width the bond-slip surface is:

$$d(A) = 2 dz \quad (5.33)$$

so that:

$$S^e = \frac{2}{\beta} \int_{\xi=-1}^{\xi=1} \mathbf{B}^T \bar{\mathbf{C}} \mathbf{B} \frac{dz}{d\xi} d\xi \quad (5.34)$$

where $dz/d\xi$ is obtained from:

$$\frac{dx}{d\xi} = \frac{\partial N_1}{\partial \xi} z_1 + \frac{\partial N_2}{\partial \xi} z_2 + \frac{\partial N_3}{\partial \xi} z_3 \quad (3.35)$$

The following tyings are needed in the model:

$$\begin{aligned} u_4 &= u_5 - \frac{1}{2}u_2 + \frac{1}{2}u_1 - \frac{1}{2}u_8 + \frac{1}{2}u_7 \\ v_4 &= v_5 - \frac{1}{2}v_2 + \frac{1}{2}v_1 - \frac{1}{2}v_8 + \frac{1}{2}v_7 \end{aligned} \quad (5.36)$$

$$\begin{aligned} u_3 &= u_1 \\ u_6 &= u_4 \\ u_9 &= u_7 \end{aligned} \quad (5.37)$$

It has been assumed here that stirrups are present, so that σ_{ya} and Δv_{ya} are not necessarily equal to σ_{yb} and Δv_{yb} respectively. If there are no stirrups, these variables will indeed have to be respectively equal, which is achieved with the following tyings:

$$\begin{aligned} v_2 &= \frac{1}{2}(v_1 + v_3) \\ v_5 &= \frac{1}{2}(v_4 + v_6) \\ v_8 &= \frac{1}{2}(v_7 + v_9) \end{aligned} \quad (5.38)$$

6 Constitutive equations of concrete and steel

6.1 Concrete

6.1.1 Yield criterion

The elasto-plastic material model will be used for describing the behaviour of concrete, combined with two tension cut-off criteria (see Fig. 6.1b). These criteria are so chosen that in the region where tension occurs in at least one direction the material will rupture in a brittle manner, without attendant plastic phenomena. Plastic material behaviour therefore occurs only in the compression-compression-compression region. The simplest of the several elasto-plastic models available in DIANA is chosen, namely, the Mohr-Coulomb yield criterion, which can be written as:

$$F = \frac{1}{2}(\sigma_1 - \sigma_3) - c \cos \theta + \frac{1}{2}(\sigma_1 + \sigma_3) \sin \theta \leq 0 \quad (6.1)$$

where the principal stresses are in the following order:

$$\sigma_1 \geq \sigma_2 \geq \sigma_3$$

So long as this condition is satisfied, the material behaves in an elastic manner. For the sake of simplicity it is further assumed that the concrete is ideally elasto-plastic. For a uniaxial state of stress this means that a bilinear σ - ϵ -diagram is adopted. If $F = 0$ the material is plastic, and in that case Drucker's postulate is applied as the yield relationship. More particularly this postulate states that the vector of the plastic strain increments is perpendicular to the yield surface.

Besides the principal stresses σ_1 and σ_3 the quantities θ and c also occur in equation (6.1). The significance of this is clarified with reference to Fig. 6.1a, where θ and c are to be regarded respectively as an angle of friction and a measure of cohesion. Together they delimit the linearly elastic region within which Mohr's circle, determined by σ_1 and σ_3 , must be situated.

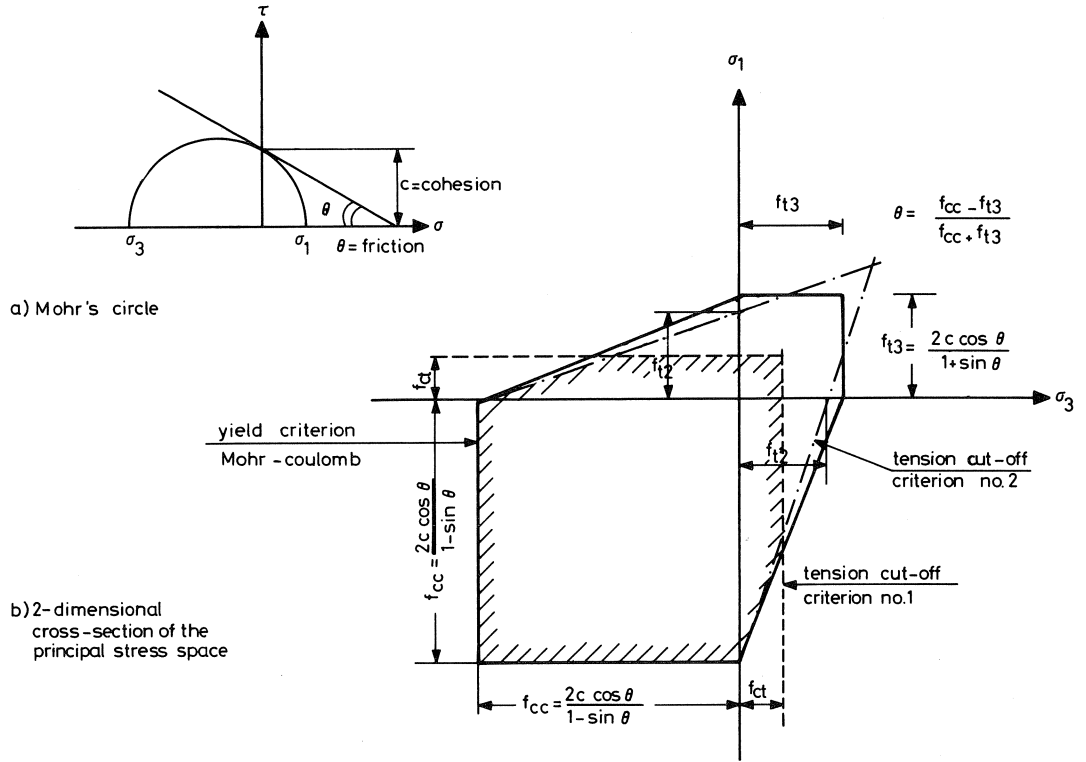


Fig. 6.1. Yield and tension cut-off criteria.

The yield criterion can alternatively be represented as in Fig. 6.1b, which can be conceived as a section through the three-dimensional principal stress space for the case where the middle principal stress σ_2 is zero. The diagram is governed by a tensile stress, which will be designated as f_{t3} , and the compressive strength f_{cc} , for which the relation with c and θ is:

$$f_{t3} = \frac{2c \cos \theta}{1 + \sin \theta} \quad (6.2)$$

$$f_{cc} = \frac{2c \cos \theta}{1 - \sin \theta} \quad (6.3)$$

Conversely, for given f_{t3} and f_{cc} , c and θ are obtained from:

$$\sin \theta = \frac{f_{cc} - f_{t3}}{f_{cc} + f_{t3}} \quad (6.4)$$

$$c = \frac{1}{2} f_{cc} \frac{(1 - \sin \theta)}{\cos \theta} \quad (6.5)$$

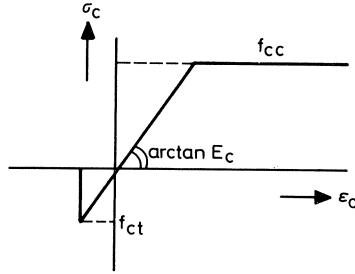


Fig. 6.2. σ_c - ϵ_c -diagram concrete

Fig. 6.1b has furthermore been utilized to indicate the two tension cut-off criteria, designated as criterion 1 and criterion 2, the first of these being applicable in a case where the compressive stresses are relatively low, while the second becomes decisive if somewhat higher compressive stresses occur and a reduction in the tensile strength is effected.

6.1.2 Tension cut-off criterion 1

According to this criterion the principal tensile stress σ_1 can never exceed the uniaxial tensile strength f_{ct} . Expressed in a formula, this becomes:

$$F = f_{ct} - \sigma_1 = 0 \quad (6.6)$$

It is further assumed that the plane of cracking is perpendicular to the direction of σ_1 , in which direction the tensile strength is assumed to be zero. In combination with the yield criterion the σ - ϵ -diagram indicated in Fig. 6.2 is thus obtained for a uniaxial state of stress.

6.1.3 Tension cut-off criterion 2

This criterion becomes the deciding one for somewhat higher values of σ_3 and is as follows:

$$F = f_{i2} \left(1 + \frac{\sigma_3}{f_{cc}} \right) - \sigma_1 = 0 \quad (6.7)$$

It is apparent from this formula, for example, that if the smallest principal tensile stress is $\sigma_3 = -f_{cc}$, no tension at all can be resisted. For criterion 2 the plane of cracking is likewise assumed to be perpendicular to the direction of σ_1 .

6.1.4 Relation between f_{ct} and the auxiliary quantities f_{i2} and f_{i3}

For the relation between f_{i2} from the tension cut-off criterion 2 and f_{i3} from the Mohr-Coulomb yield criterion the following has been adopted in the calculations:

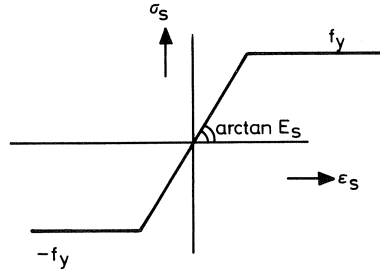


Fig. 6.3. σ_s - ϵ_s -diagram steel

$$f_{t3} = 1.01f_{t2} \quad (6.8)$$

by which tension cut-off criterion 2 is decisive just a little earlier than the yield criterion, so that – as already noted previously – plastic behaviour occurs only in the compression-compression region.

The ratio of f_{t2} to f_{ct} is always taken as:

$$f_{t2}/f_{ct} = 2 \quad (6.9)$$

which is in reasonably good agreement with what is observed experimentally.

However, the tension cut-off criterion 2 has not been applied in the calculations described in Section 7.2, because this criterion had, at that time, not yet been incorporated in DIANA.

6.2 Steel

The reinforcing steel is also conceived as an ideally elasto-plastic material (Fig. 6.3). Its elastic range is described by means of the modulus of elasticity E_s and Poisson's ratio ν_s . The choice of the yield criterion is of no further importance, since the steel stress is smaller than the yield stress in all the calculations.

7 Verification of the axially symmetric element

7.1 Verification with reference to tests by Dörr and Mehlhorn [10]

7.1.1 Data of the tests

The results of a series of tests performed by Dörr and Mehlhorn, comprising 34 axially symmetric specimens, were used for verifying the axially symmetric element. The only variable in that test series was the external radial pressure as summarized in Table 7.1. The reinforcement consisted of a deformed (ribbed) bar of 16 mm diameter, steel grade BST 42/50 IIIA. The geometric features of the specimens are shown in Fig. 7.1, while the reinforcing bar is shown in Fig. 7.2.

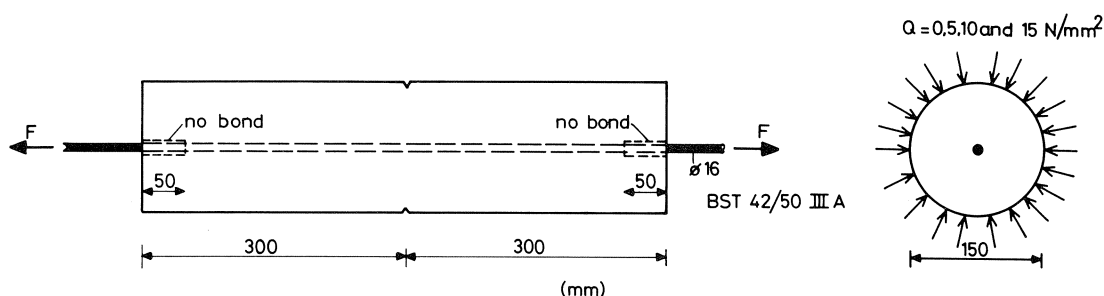


Fig. 7.1. Geometry of the specimens of Dörr and Mehlhorn.

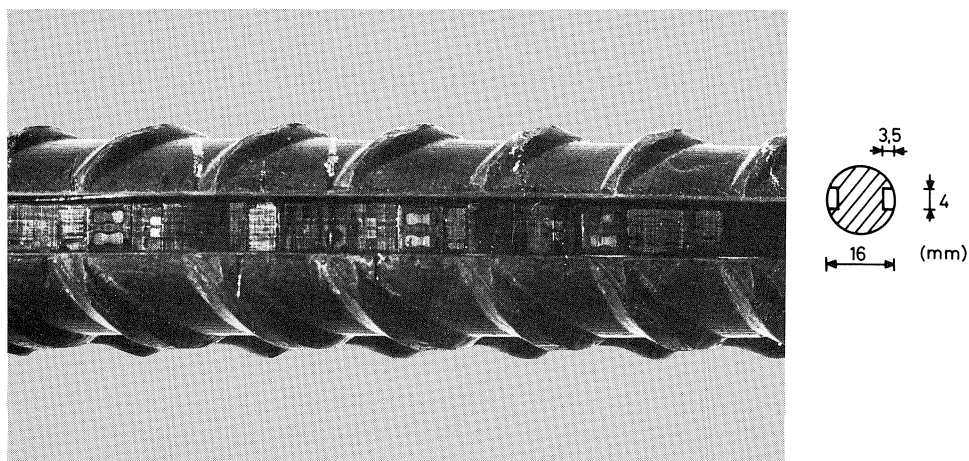


Fig. 7.2. The reinforcing bar.

Table 7.1 External radial pressures applied in the tests performed by Dörr and Mehlhorn

number of specimens	radial pressure Q in N/mm^2
6	0
7	5
6	10
6	15
3	2
5	7
1	11

Of the radial pressure values stated in this table only the first four ($Q = 0, 5, 10$ and 15 N/mm^2) are considered here. For each of these values there are something like six specimens available. It is thus possible, despite a certain amount of scatter in the measured concrete strengths, to select a series having virtually the same cylinder compressive strength f_{cc} . This series is presented in Table 7.2, where also the splitting tensile

strength f_{sp} is given (as far as possible) and where the test No. indicated in the first column corresponds to [10].

Table 7.2 Reference basis

test No.	radial pressure Q (N/mm ²)	f_{cc} (N/mm ²)	f_{sp} (N/mm ²)
6-1	0	29.8	–
35-1	5	30.8	2.02
46-1	10	28.8	2.84
50-1	15	29.8	–

The selected series comprises tests in which the tensile force was increased monotonically.

According to data supplied by Mehlhorn, the modulus of elasticity E_c of the concrete can in all cases be taken as $E_c = 30000 \text{ N/mm}^2$. The calibration curves in [10] indicated a value $E_s = 206000 \text{ N/mm}^2$ for the modulus of elasticity of the reinforcing steel.

As the bar was provided with $3.5 \text{ mm} \times 4 \text{ mm}$ slots for accommodating strain gauges (see Fig. 7.2), a fictitious value was adopted for the modulus of elasticity:

$$E_s = \frac{A_{\text{net}}}{A_{\text{gross}}} \times 206000 = \frac{173}{201} \times 206000 = 177000 \text{ N/mm}^2$$

The associated axial steel stresses σ_a are therefore likewise fictitious and are referred to the gross cross-sectional area ($A_{\text{gross}} = \pi r^2$). With this procedure it was possible correctly and in a simple manner to take account of the total circumference ($2\pi r$) which partly determines the resistance to slip.

7.1.2 Schematization of material properties in the analysis and element distribution

Reinforcing steel: $E_s = 177000 \text{ N/mm}^2$ (fictitious)

$$\nu_s = 0$$

The yield point f_y of the steel is unimportant because in all the tests the stress employed is far below this value.

Concrete: The Mohr-Coulomb criterion is adopted, supplemented (except in Section 7.2) with two tension cut-off criteria as indicated in Fig. 6.1. The parameters which determine these criteria are:

$$f_{cc} = 30 \text{ N/mm}^2; \quad f_{ct} = 2.1 \text{ N/mm}^2; \quad f_{t2} = 4.2 \text{ N/mm}^2; \quad f_{t3} = 1.01f_{t2}$$

From equations (6.4) and (6.5) it follows that $c = 5.65 \text{ N/mm}^2$ and $\theta = 0.85$. The modulus of elasticity of the concrete E_c will always be stated separately. In all cases the value $\nu_c = 0.2$ has been adopted for Poisson's ratio.

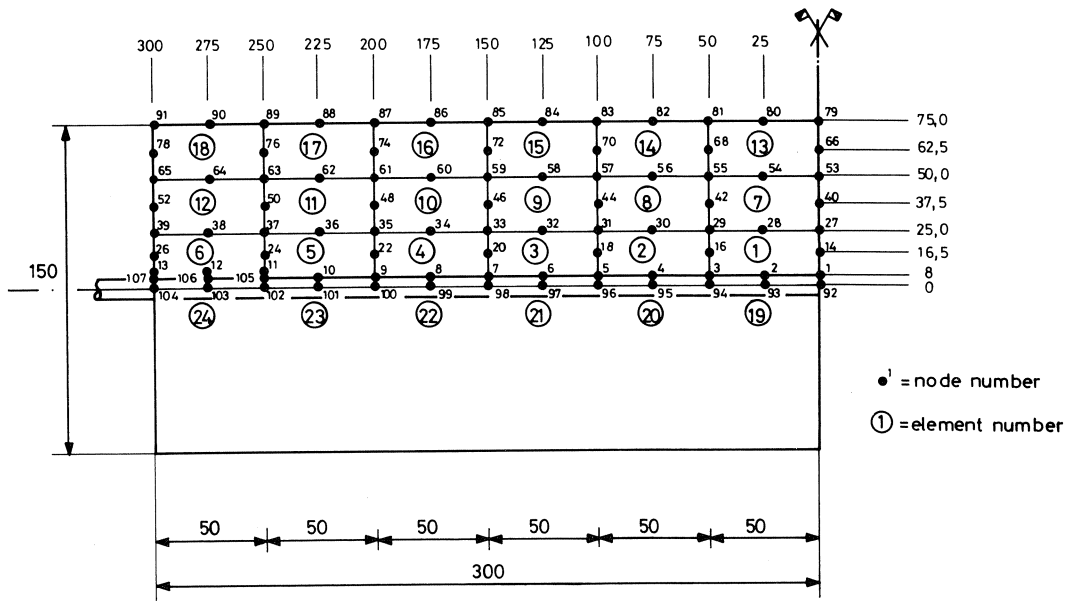


Fig. 7.3. Element distribution.

Element distribution: See Fig. 7.3. An axially symmetric element with eight nodes, with two degrees of freedom per node, was adopted for the concrete. Four integration points per element were applied. For the steel the axially symmetric bond-slip element was adopted, with six nodes and a total of nine degrees of freedom and three integration points. Actually there are twelve degrees of freedom, but three of them are taken as zero, namely, those associated with the radial displacement of the nodes on the axis of symmetry. At the end of the test specimen, at the nodes 105, 106 and 107, the reinforcement is detached from the concrete specimen, which is in agreement with the manner of construction of the specimens. Symmetric considerations have been applied in the analysis, though actually this symmetry (more particularly with regard to the measured steel stress) was not manifest in the test results, probably because of the manner of casting the specimens (vertical), which caused variation in the quality of the concrete along each specimen.

7.2 Verification with reference to tests without radial pressure

7.2.1 General

Verification of the axially symmetric bond-slip element was begun by considering the case where the external radial pressure was zero ($Q = 0$) [5]. In this first attempt at verification no experience at all had as yet been gained with the element. Besides, at that stage it was not yet possible, for example, to apply the tension cut-off criterion 2 (see

Fig. 6.1). This being so, the choice of the various parameters in the analysis was fairly arbitrary. All the same, the results obtained give a reasonably good measure of insight into the serviceability of the model. The test results for test 6.1 in Table 7.2 were used in performing the verification. Contrary to the general statement in Section 7.1.2, in this present Section only one tension cut-off criterion was considered in the analysis, i.e., criterion 1 as indicated in Fig. 6.1, with the bound $f_{ct} = 2.1 \text{ N/mm}^2$. Furthermore, here a value of $f_{t3} = 3 \text{ N/mm}^2$ has been adopted in the Mohr-Coulomb criterion, so that from equations (6.4) and (6.5) it follows that $c = 4.75 \text{ N/mm}^2$ and $\theta = 0.96$.

7.2.2 Effect of load level

The following bond-slip parameters were adopted in the analysis:

$$k = 0; \Delta u_{\max} = \infty; S = 100 \text{ N/mm}^3; \alpha = 1$$

It was furthermore assumed that $E_c = 10000 \text{ N/mm}^2$.

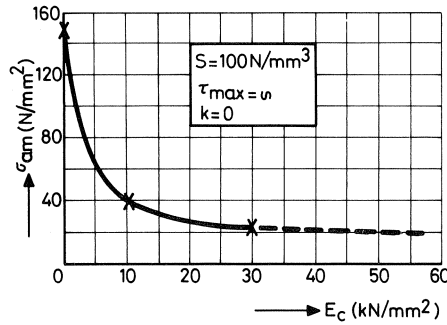
In the analysis the tensile force applied to the test specimen was raised incrementally as indicated in Table 7.3.

Table 7.3

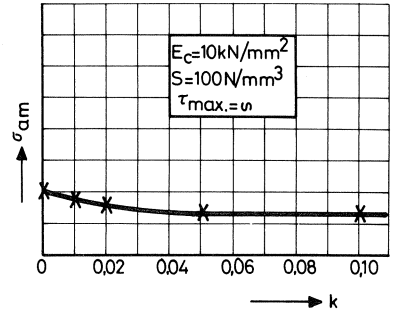
designation in Fig. 7.4	tensile force (kN)	fictitious steel stress σ_a (N/mm ²)	corresponds to load increment No. in test
(1)	30	149.2	8
(2)	40	198.9	9
(3)	45	223.9	-
(4)	48	238.8	-
(5)	48.6	241.8	~ 10

The results of the calculations are presented in Fig. 7.4 and are provided with the respective designations (1), (2), etc. In this analysis a continuous (through-and-through) crack was found to develop between increments (4) and (5). Because of this the load had to be applied cautiously in small increments. Increment (5) involved considerably more computation time before the stop criterion was satisfied. As in all the other calculations mentioned in the present chapter, this criterion stated that the sum of the squares of the displacement increases within an iteration step had to be less than 10^{-5} times the sum of the squares of the total displacements. Since the criterion is concerned with squares (quadratic quantities), only the magnitude, not the algebraic sign, of these displacements is of importance.

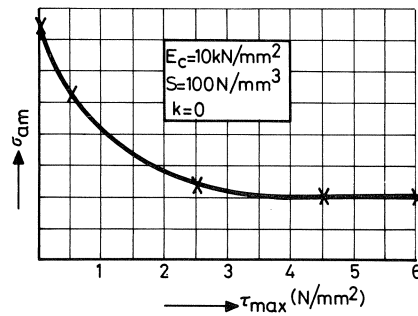
The development of cracking can be investigated with the aid of Fig. 7.5. As appears from Fig. 7.4, the calculated steel stress is in good agreement with the measured steel stress. After the occurrence of the first continuous crack, between increments (4) and (5), this agreement is distinctly less good, however. This is attributable to the fact that in the test the development of cracking takes place very locally, whereas in the analysis there was cracking in a number of places.



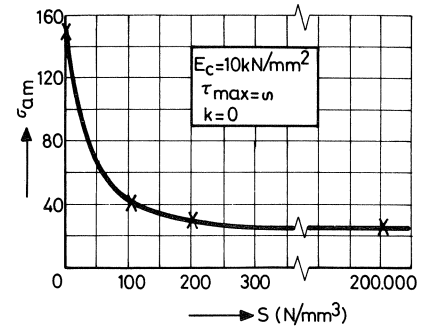
Ⓐ influence of E_c



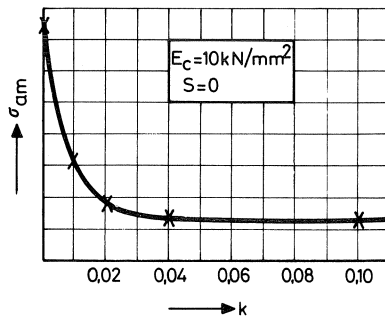
Ⓑ influence of k



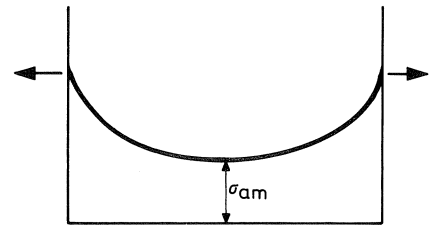
Ⓒ influence of τ_{\max}



Ⓓ influence of S



Ⓔ influence of k



Ⓕ definition of σ_{am}

Fig. 7.6. Results of the parameter study

It is apparent from Figs. 7.6b, 7.6d and 7.6e that, in the case under investigation, for values of the slip modulus S above 300 N/mm³ and/or for values of the rib factor k above 0.1 the specimen behaves as if there were complete bond. In Fig. 7.6b the effect of k is seen to be slight. This is the case for a real value of S . On the other hand, if an extremely low value of S is considered (Fig. 7.6e), the effect of k is found to be very great.

This is to be regarded as illustrating the amount of freedom that exists in choosing the magnitude of the various parameters, because different combinations of parameters can result in equally good agreement between experimentally determined and calculated values.

7.3 Verification with reference to tests with radial pressure

7.3.1 General

When the research described in the previous Section had been completed, the DIANA program had meanwhile been modified to permit the analysis also of specimens subjected to external radial pressure. A number of calculations in which the results are again compared with the experimental ones obtained by Dörr and Mehlhorn are reported in [5], but now with external radial pressure acting. In the various calculations the externally applied tensile force in the reinforcing bar is always $F = 30$ kN. This choice appeared suitable because at this value of the force no through-and-through cracking of the specimen occurred at any value of the external radial pressure Q .

7.3.2 Distribution of steel stress

For this load $F = 30$ kN the test was analytically checked for three combinations of bond-slip parameters. For this purpose the properties stated in Section 7.1.2 were adopted, with $E_c = 25000$ N/mm², i.e., the measured $E_c = 30000$ N/mm² was reduced somewhat in order to take account of the decrease of the slope of the σ_c - ε_c -diagram of concrete for the higher stresses. The calculated results are compared with the experimental ones in Figs. 7.7 to 7.10. In these diagrams the calculated and the measured steel stress values have been plotted for the three combinations considered. The bond-slip parameters in these combinations are summarized in Table 7.4.

Table 7.4 Parameter combinations investigated, as envisaged in Figs. 7.7 to 7.10

	case A (standard combination)	case B	case C (same as A, except for Δu_{\max})
$C_1 = S + k^2 \frac{\alpha E_s}{r}$ (N/mm ³)	200	316	200
$C_2 = \frac{\alpha E_s}{r}$ (N/mm ³)	25750	25750	25750
$C_3 = k \frac{\alpha E_s}{r}$ (N/mm ³)	1000	2000	1000
Δu_{\max} (mm)	0,01	0,01	∞
f_{i2}/f_{ct}	2	2	2

The calculated results for combination B are missing from Fig. 7.10, this being due to

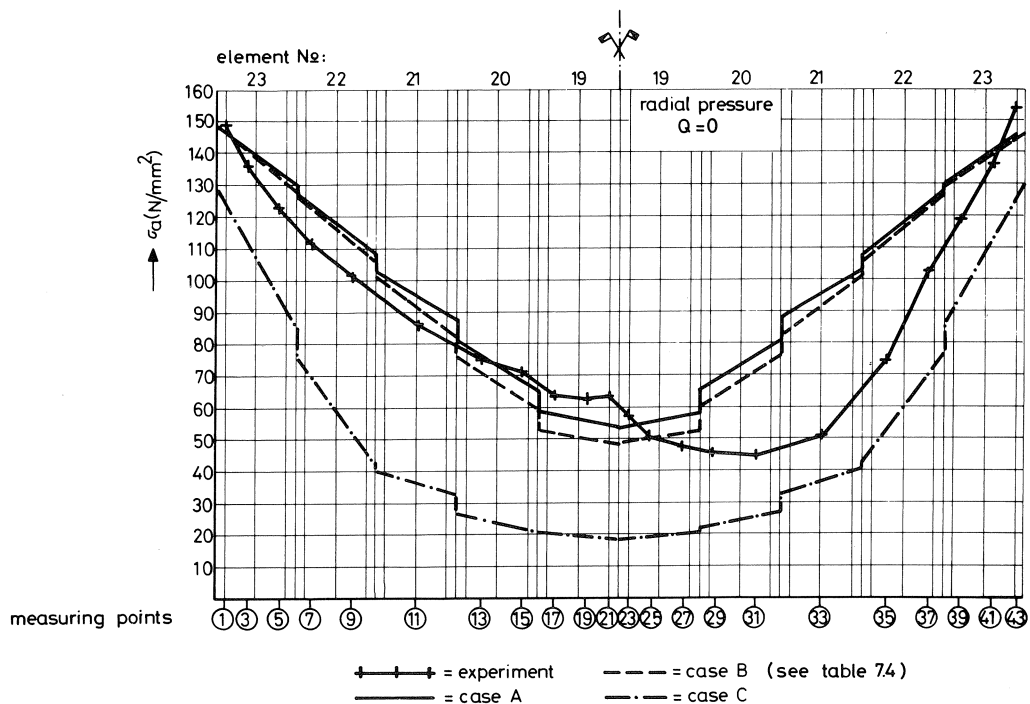


Fig. 7.7. Distribution of the steel stress σ_a

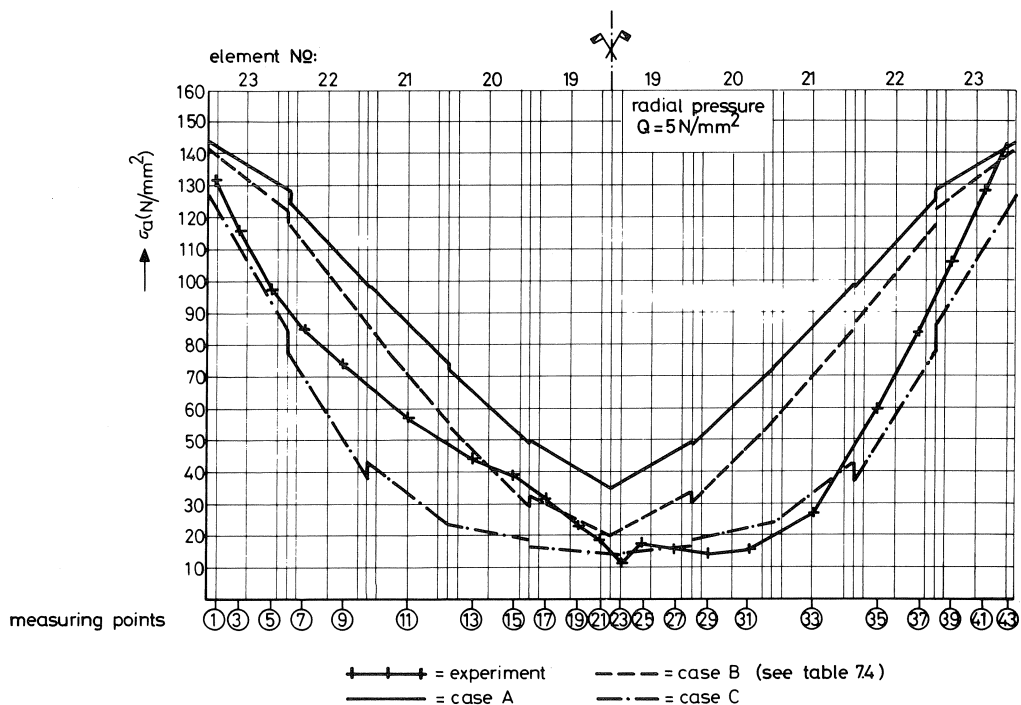


Fig. 7.8. Distribution of the steel stress σ_a

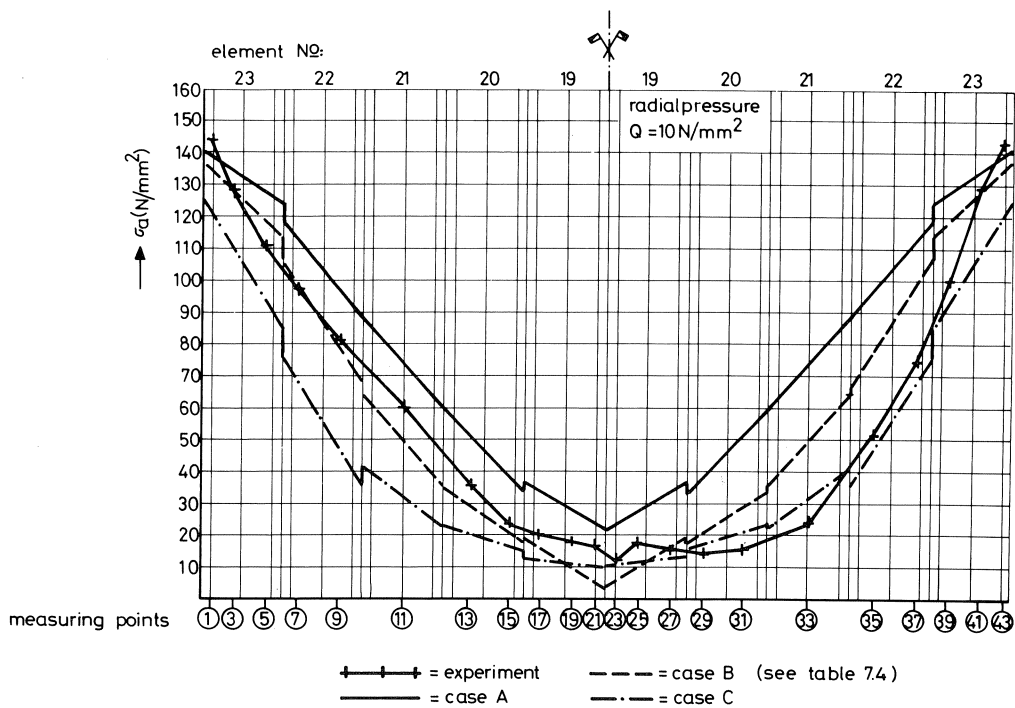


Fig. 7.9. Distribution of the steel stress σ_a

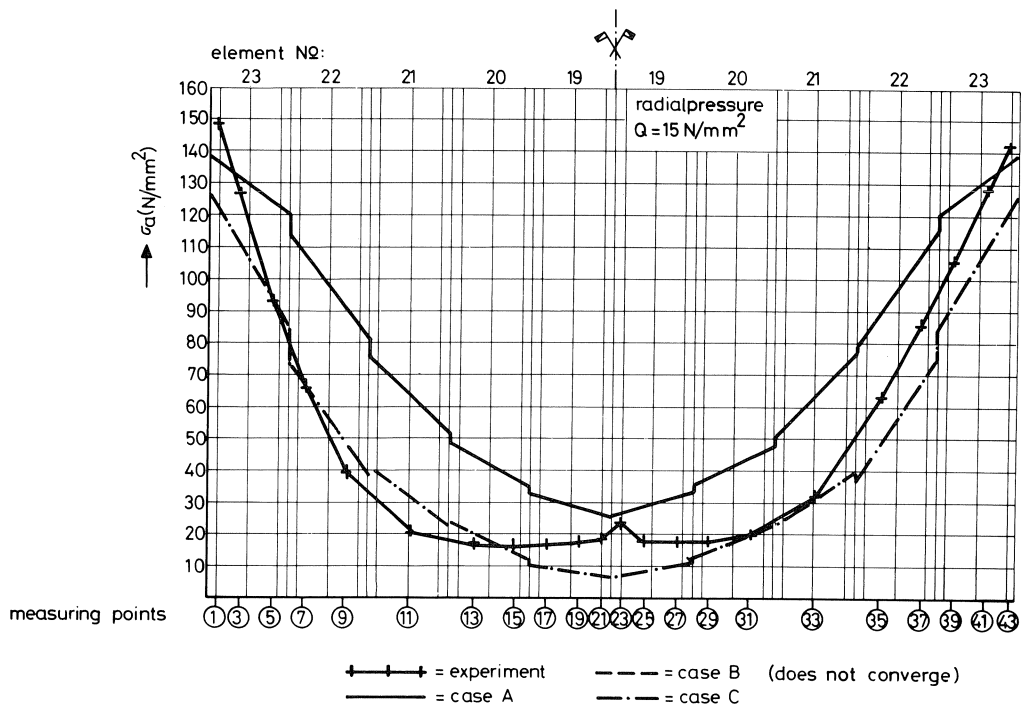


Fig. 7.10. Distribution of the steel stress σ_a

convergence problems encountered at the time. It can nevertheless be concluded that the combinations B and C in general, for the various radial pressures, yield results that are in reasonably good agreement with the experimental results. The exception to this is the case considered in Fig. 7.7 (external radial pressure $Q = 0$), for which combination C is found to be much too rigid. From this it must be concluded that for $Q = 0$ it is necessary to introduce a limit for Δu_{\max} . If $\Delta u_{\max} = 0.01$ mm is adopted for this, so that combination A is obtained, there is found to be much better agreement for $Q = 0$: combination A is then equivalent to combination B. In the cases where $Q \neq 0$ (Figs. 7.8 to 7.10), however, the agreement for case A is poorer than for case B, so that this latter combination must be rated the best. It is to be noted that Δu_{\max} is evidently a function of the magnitude of the radial pressure and is therefore not constant as has been assumed for varying Q in cases A and B.

7.3.3 Parameter study

Besides the calculations described in the foregoing, a parameter study was also carried out in [5]. For the purpose of that study the combination A of Table 7.4 was chosen as the standard combination.

The parameters C_1 and C_3 employed in the parameter study are defined after equation (2.30), which definitions will for the sake of convenience be repeated here, at the same time noting that always $C_5 = 0$ and $C_6 = 0$ has been adopted. Thus the following relation between τ , σ_r , Δu and Δv exists:

$$\begin{bmatrix} \tau \\ \sigma_r \end{bmatrix} = \begin{bmatrix} C_1 & -C_3 \\ -C_3 & C_2 \end{bmatrix} \times \begin{bmatrix} \Delta u \\ \Delta v \end{bmatrix} \quad (7.1)$$

where:

$$C_1 = S + k^2 C_2 = S + k C_3 \quad (2.31)$$

$$C_2 = \alpha \frac{E_s}{r} \quad (2.23)$$

$$C_3 = k C_2 \quad (2.32)$$

The results of the parameter study are summarized in Figs. 7.11 to 7.15. Figs. 7.11 and 7.12 relate to the steel stress at the centre of the specimen, while Figs. 7.13 and 7.14 relate to the steel stress at a quarter of its length. Besides these calculated stresses plotted as functions of the parameter that was varied, the measured steel stress values are included in these diagrams.

On the basis of the results of the parameter study the following can be stated with regard to the effect of the parameters C_1 to C_3 on the bond-slip behaviour and the effect of Δu_{\max} and the ratio f_{t2}/f_{cc} .

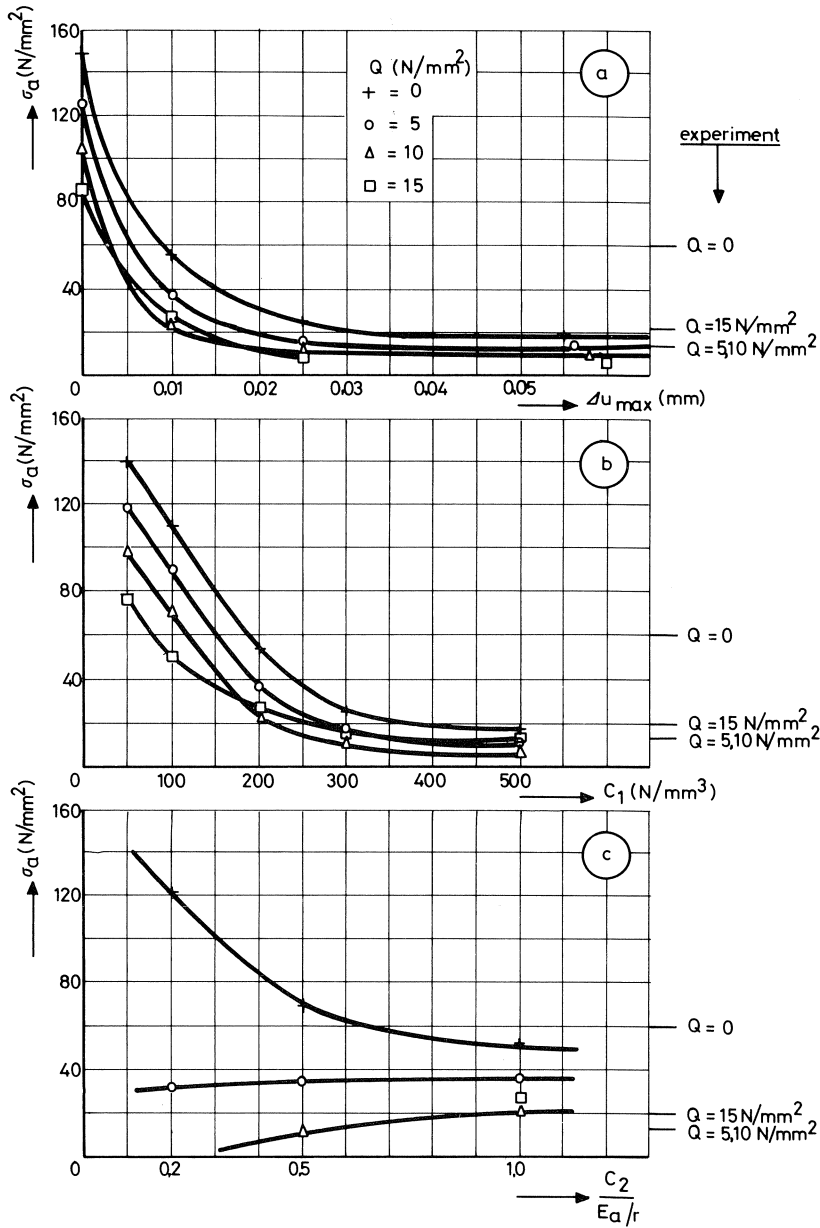


Fig. 7.11. Influence of parameters on steel stress at measuring point 21 (centre of specimen).

Effect of C_1 ($= S + \alpha k^2 E_s / r$):

From Figs. 7.11b and 7.13b, corresponding to the steel stress at the centre and at a quarter of the specimen respectively (measuring points 21 and 11 respectively), it appears that the steel stress behaviour is entirely in conformity with expectations. With increas-

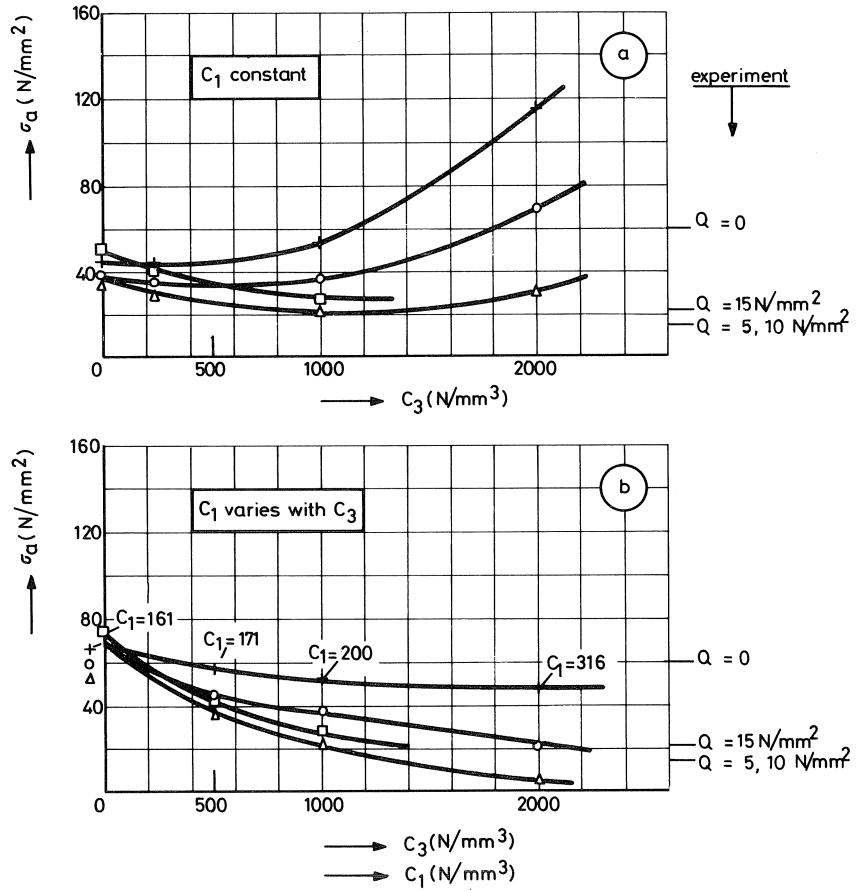


Fig. 7.12. Influence of parameters on steel stress at measuring point 21 (centre of specimen).

ing magnitude of C_1 the slip resistance increases, as a result of which the steel stress decreases.

Effect of C_2 ($= \alpha E_s / r$):

Figs. 7.11c and 7.13c show that little variation occurs over a considerable range extending from $C_2 = 0.5E_s/r$ to $C_2 = E_s/r$. For values of C_2 smaller than $0.5E_s/r$ the effect on the results becomes clearly manifest. In the case of $C_2 = 0.2E_s/r$ it is even found that for radial pressure values $Q = 10$ and $Q = 15 \text{ N/mm}^2$ no solution can be obtained, this being due to convergence problems caused by through-and-through cracking of the specimen. Such cracking occurs earlier according as the radial pressure becomes larger. This in turn is bound up with the fact that the tension cut-off criterion No. 2 in Fig. 6.1b results in lower tensile strengths for higher compressive stresses. For the radial pressure $Q = 15 \text{ N/mm}^2$ there is divergence also for $C_2 = 0.5E_s/r$, and a supplementary analysis for $Q = 15 \text{ N/mm}^2$ and $C_2 = 0.75E_s/r$ still showed divergence to occur.

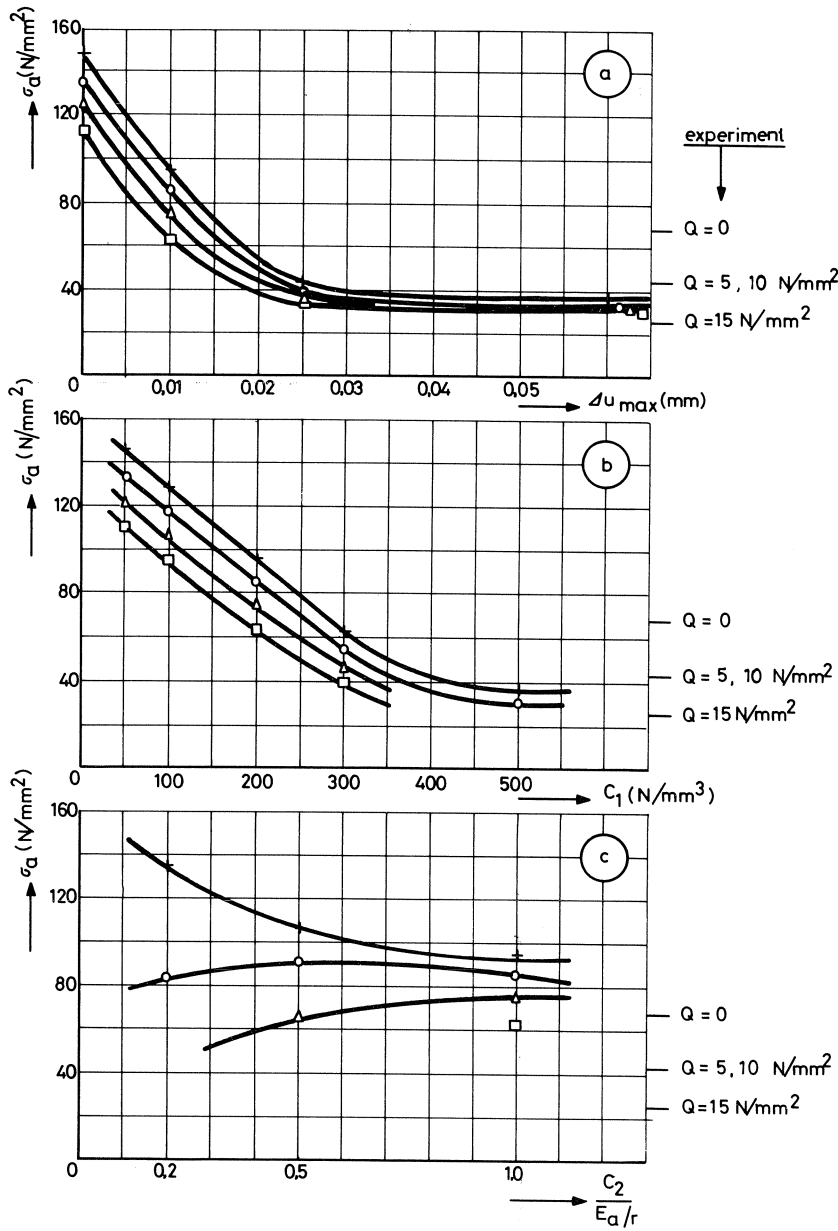


Fig. 7.13. Influence of parameters on steel stress at measuring point 11 (at $1/4$ of specimen).

Hence it would appear advisable not to adopt values lower than $0.5E_s/r$ for C_2 . According to equation (2.23), i.e., $C_2 = \alpha E_s/r$, this is an indication that α must likewise be of the order of magnitude of 0.5 to 1.0. It cannot, however, be more than just an indication, since – according to equations (2.31) and (2.32) – C_1 and C_3 would also have had to vary

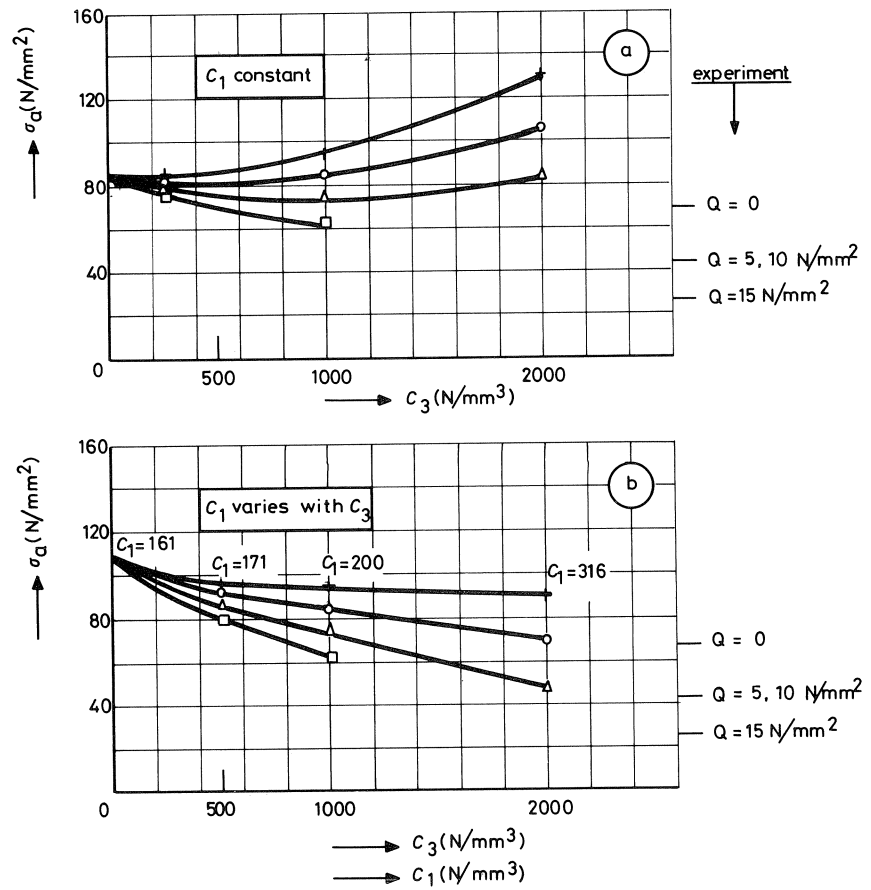


Fig. 7.14. Influence of parameters on steel stress at measuring point 11 (at $\frac{1}{4}$ of specimen).

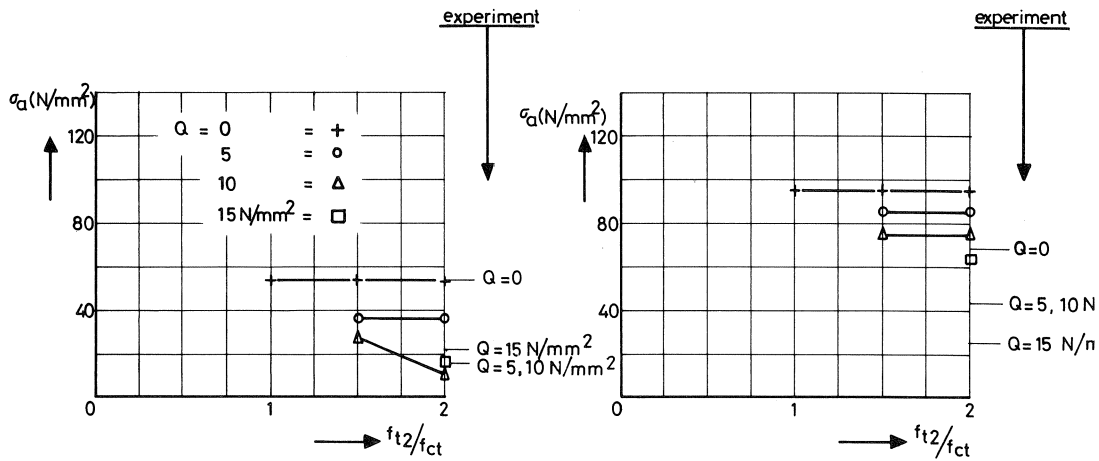


Fig. 7.15. Influence of ratio f_{t2}/f_{ct} on σ_{am} at

along with C_2 in order to determine the actual correct effect of α from Figs. 7.11c and 7.13c.

Effect of C_3 ($= \alpha k E_s / r$):

Figs. 7.12a and 7.14a show the effect of C_3 . With increasing magnitude of C_3 the steel stress is found to increase, which at first sight is a somewhat odd phenomenon. In view of the relation $C_3 = k C_2$ it might be supposed that a variation of C_3 corresponds to a variation of the rib factor k and that with increasing interlocking action the steel stress should surely decrease, not increase. However, it must be considered that C_1 was kept constant at 200 N/mm^3 , so that according to equation (2.31), i.e., $C_1 = S + k C_3$, the surface friction S varies along with k when C_1 is constant. For this reason Figs. 7.12b and 7.14b have been compiled. In these diagrams S has been kept constant at the value corresponding to the standard case $C_1 = 200 \text{ N/mm}^3$, $C_2 = 25750 \text{ N/mm}^3$ and $C_3 = 1000 \text{ N/mm}^3$. From $C_3 = k C_2$ it follows that then $k = 0.0388$, so that $k C_3 = 39$. Hence $S = 200 - 39 = 161 \text{ N/mm}^3$. This value has been kept constant, so that in Figs. 7.12b and 7.14b the magnitude of C_1 varies with that of C_3 .

The results represented in Figs. 7.12b and 7.14b now have a more familiar look. It is seen that for $C_3 = 0$, in which case there is no mechanical interlocking action, the same steel stress is obtained for all values of the radial pressure. This is in agreement with the basic conception that S is independent of the radial stress σ_r .

Effect of Δu_{\max} :

It appears from Figs. 7.11a and 7.13a that above $\Delta u_{\max} = 0.025 \text{ mm}$ there is little further variation in the calculated steel stress at $\frac{1}{2}l$ and $\frac{1}{4}l$ respectively. Having regard to the experimental results, values below 0.01 mm appear rather unlikely. Comparison of the calculated results with the experimental ones further indicates that there must exist a relation between the magnitude of the radial pressure and that of Δu_{\max} . Such a relation will be given later on, in equation (7.2).

Effect of f_{t2}/f_{ct} :

Nearly all the analyses were performed for $f_{t2} = 2f_{ct}$. The Mohr-Coulomb criterion was so chosen that the tension cut-off criteria were always the deciding features in the tension-tension and tension-compression regions. The choice $f_{t2} = 2f_{ct}$ was based on the consideration that premature development of primary cracking in the specimens at somewhat higher values of the radial pressure should be prevented. Besides this choice $f_{t2} = 2f_{ct}$, the analysis for the standard case was also performed with $f_{t2} = 1.5f_{ct}$ and $f_{t2} = f_{ct}$. In both these last-mentioned cases the assumption $f_{t3} = 1.01f_{t2}$ was again made for the Mohr-Coulomb criterion, so that from equations (6.4) and (6.5):

$$\begin{aligned} f_{t2} = 1.5f_{ct} &\rightarrow c = 4.9 \text{ N/mm}^2; \quad \theta = 0.94 \\ f_{t2} = f_{ct} &\rightarrow c = 4.0 \text{ N/mm}^2; \quad \theta = 1.05 \end{aligned}$$

So far as possible, the results are given in Fig. 7.15. For $f_{t2} = 1.5f_{ct}$ the specimen cracked through-and-through at $Q = 15 \text{ N/mm}^2$. For $f_{t2} = f_{ct}$ this occurred already at $Q = 5 \text{ N/mm}^2$. Since such cracking did not take place in the tests, it must be concluded that $f_{t2} = 2f_{ct}$ is the best choice for the analysis of this case.

7.3.4 Provisional conclusions and recommendations

The bond-slip element developed here would appear to be a good approximation for an axially symmetric test specimen. It is found possible to obtain reasonably close agreement with the actual behaviour, while few problems arising from computation time and rate of convergence are encountered. This conclusion remains valid up to instant of through-and-through cracking. When a specimen is at the point of cracking through, the further analysis will have to proceed very cautiously and will involve much computation time. If this requirement is ignored, it may well occur that during the iteration procedure the specimen will wrongly appear to develop cracks over a very extensive region. Of course, this problem can be avoided by the assumption of a certain amount of scatter in the material properties throughout the specimen or by the deliberate choice of a low concrete strength in the region where the crack is expected to form.

On the basis of the research described so far, in [5] the following recommendations were made as to the numerical values of the various bond-slip parameters:

$$S = 100 - 150 \text{ N/mm}^3; \quad k = 0.05 - 0.1; \quad \alpha = 0.5 - 1; \quad \Delta u_{\max} = 0.01 \text{ mm}$$

The recommended value for k was obtained by applying the relation $k = C_3/C_2$ to the values of C_2 and C_3 given in Table 7.4 for the cases A and B employed in the research. The magnitude of S was determined from $S = C_1 - kC_3$, while that of α is as explained in Section 7.3.3. The value recommended for Δu_{\max} is probably too low.

In fact, having regard to results published in the literature, a much more realistic value to be adopted would be $\Delta u_{\max} = 0.025 \text{ mm}$. In this context, see the τ - Δu -relation in Fig. 7.16 which Wahla recommends (consider, for example, Fig. B16 in [11]). The magnitude of S is 200 N/mm^3 in that case, which is not at variance with the results that have so far been obtained. It was accordingly decided to adopt the following values for the purpose of the further investigations:

$$\begin{aligned} S &= 200 \text{ N/mm}^3 \\ k &= 0.05 - 0.1 \\ \alpha &= 1 \\ \Delta u_{\max} &= 0.025 \text{ mm} \end{aligned}$$

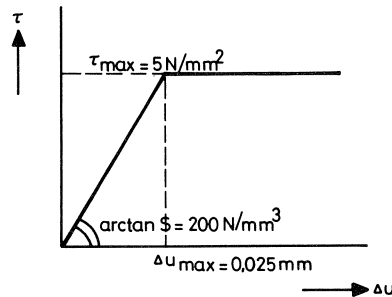


Fig. 7.16. τ - Δu -relation recommended by Wahla [11].

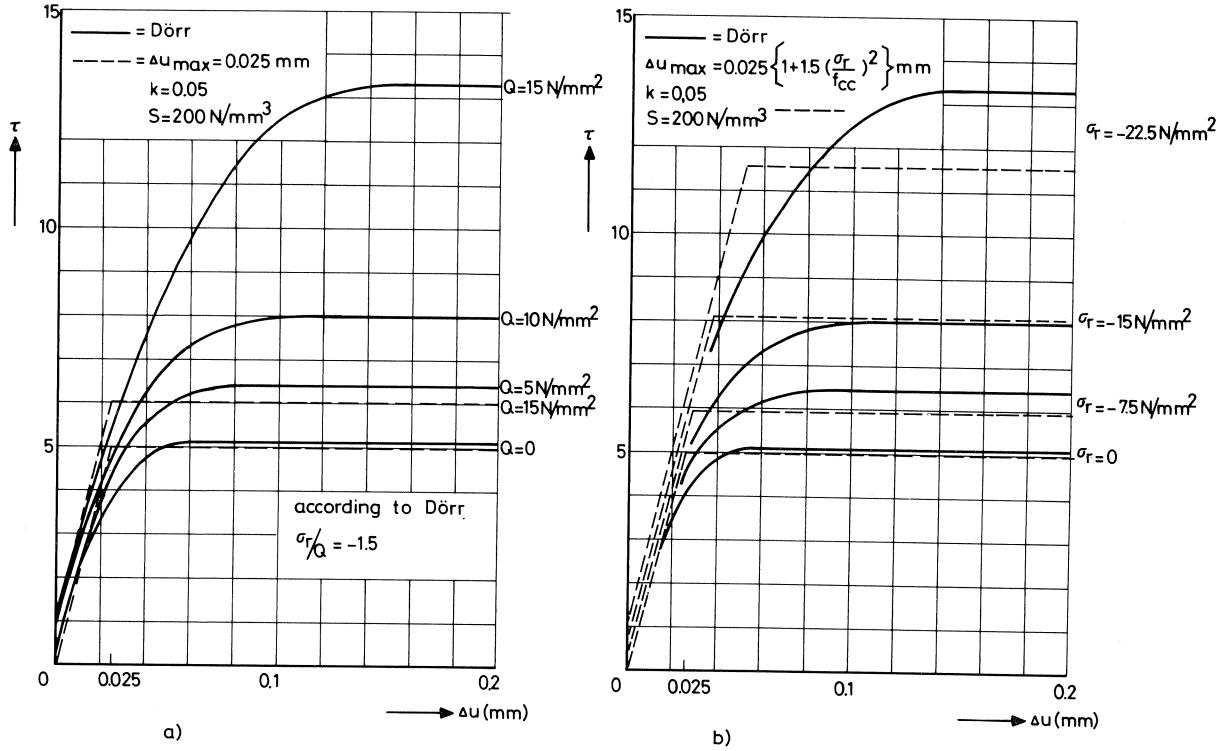


Fig. 7.17. τ - Δu -relation according to Dörr [20].

The choice of $\alpha = 1$ was made for the sake of simplicity.

With regard to the magnitude of Δu_{\max} the following can be said. As stated in Section 2.1, Δu_{\max} is to be regarded as dependent on the magnitude of the radial stress. This can also be inferred from the τ - Δu -relations as a function of the external radial pressure as deduced by Dörr from his measurements and reported in his thesis [20]. The τ - Δu -relations found by Dörr have been reproduced in Fig. 7.17a. In the same diagram are indicated the relations resulting from the recommendations $S = 200 \text{ N/mm}^3$, $k = 0.05$, $\alpha = 1$ and $\Delta u_{\max} = 0.025 \text{ mm}$ for the external radial pressures $Q = 0$ and $Q = 15 \text{ N/mm}^2$.

The recommendations for k and S are found to be quite satisfactory in both cases. The slope and the initial point of the rising branches are suitably described. Also the magnitude of Δu_{\max} in the case where $Q = 0$ appears to be a suitable choice. For $Q > 0$, however, Δu_{\max} (and therefore τ_{\max}) is not satisfactory.

Hence the magnitude of Δu_{\max} was introduced as dependent upon the magnitude of σ_r . For this purpose the ratio between the external radial pressure Q and the radial pressure σ_r (compressive stress) on the bar itself, as determined by Dörr for the specimens considered, was adopted, namely, $\sigma_r = -1.5Q$.

With the aid of this information the following recommendation for Δu_{\max} can be derived:

$$\Delta u_{\max} = 0.025 \left\{ 1 + 1.5 \left(\frac{\sigma_r}{f_{cc}} \right)^2 \right\} \text{ mm} \quad (7.2)$$

With the aid of this amended recommendation for Δu_{\max} the relation represented in Fig. 7.17b is obtained. Now for all values of the radial pressure there is good agreement with the results of Dörr.

Finally, for the extension to the 3D element the recommendation stated in equation (7.2) can be written as:

$$\Delta u_{\max} = 0.025 \left\{ 1 + 1.5 \left(\frac{\sigma_{xa} + \sigma_{xb} + \sigma_{ya} + \sigma_{yb}}{4f_{cc}} \right)^2 \right\} \text{ mm} \quad (7.3)$$

Equation (7.2) yields good results if σ_r is negative, i.e., is indeed a compressive stress. In the opposite case, i.e., where σ_r is a tensile stress, this equation will obviously not be satisfactory, and the following approximation would then appear to be more suitable:

$$\Delta u_{\max} = 0.025 \left(1 - \frac{\sigma_r}{f_{ct}} \right) \text{ mm} \quad (7.4)$$

which, for the general 3D case, can be written as follows:

$$\Delta u_{\max} = 0.025 \left(1 - \frac{\sigma_{xa} + \sigma_{xb} + \sigma_{ya} + \sigma_{yb}}{4f_{ct}} \right) \text{ mm} \quad (7.5)$$

Equation (7.4) is applicable if $\sigma_r > 0$, while equation (7.5) should be applied if $\sigma_{xa} + \sigma_{xb} + \sigma_{ya} + \sigma_{yb} > 0$.

In the above mathematical expressions Δu_{\max} varies linearly from 0.025 mm for the case $\sigma_r = 0$ to 0 for the case $\sigma_r = f_{ct}$. In this latter case it is in fact logical to assume that no further slip resistance can be developed when the tensile strength of the concrete has been reached.

It should, finally, be borne in mind that $\sigma_r = 0$ not only forms the boundary between the ranges of application of equation (7.2) and (7.4), and between those of equations (7.3) and (7.5), but also decides whether $k=0$ should be adopted, as discussed in Section 4.3.

8 Verification of the symmetric variant of the 3D element

8.1 Introduction

When the analysis of the axially symmetric bond-slip element had yielded deeper insight into the various parameters, the research was continued. Attention was not at once switched to the general 3D bond-slip element. Instead, the symmetric variant thereof was considered. The equations for this variant have been given in Chapter 3.

Verification was done with reference to a test from a TNO-IBBC series of three tests on prisms with a central reinforcing bar [4], as shown schematically in Fig. 8.1. The test with the 12 mm diameter bar was adopted for the purpose of this verification. The measured values for the modulus of elasticity and the prism compressive strength were

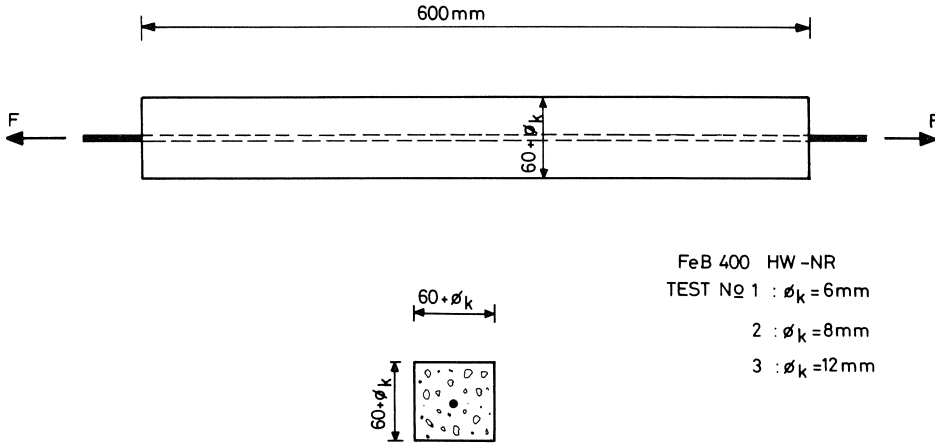


Fig. 8.1. Test series of TNO-IBBC [4].

$E_c = 28000 \text{ N/mm}^2$ and $f_{cc} = 29.6 \text{ N/mm}^2$ respectively. The cube splitting strength was $f_{sp} = 3.3 \text{ N/mm}^2$, and the modulus of elasticity of the steel was $E_s = 205600 \text{ N/mm}^2$.

8.2 Schematization of material properties in the analysis and element distribution

Reinforcing steel:

$$E_s = 205600 \text{ N/mm}^2$$

$$\nu_s = 0$$

The yield point of the reinforcement plays no part in the calculations.

Concrete:

$$E_c = 28000 \text{ N/mm}^2$$

$$f_{cc} = 29.6 \text{ N/mm}^2$$

$$\nu_c = 0.2$$

The Mohr-Coulomb yield criterion was adopted, supplemented by two tension cut-off criteria, as indicated in Fig. 6.1. The tensile strength was taken as $f_{ct} = 0.7 \times 3.3 = 2.1 \text{ N/mm}^2$ because a minimum, not an average, value for the strength has to be used in the calculations. As before, the choice $f_{i2} = 2f_{ct}$ was made, so that $f_{i2} = 4.2 \text{ N/mm}^2$. According to equations (6.4) and (6.5) with the assumption $f_{i3} = 1.01f_{i2}$ this meant: $c = 5.9 \text{ N/mm}^2$ and $\theta = 0.82$.

Element distribution: See Fig. 8.2. The mathematical model comprises 20 volume elements for the concrete and five slip elements. Eight integration points are used in the concrete element, three in the slip element. The analysis makes use not only of symmetry with respect to the X -axis and Y -axis, but also of symmetry with respect to the XOY -plane. In the analysis a restraint (condition of fixity) is assumed at this plane,

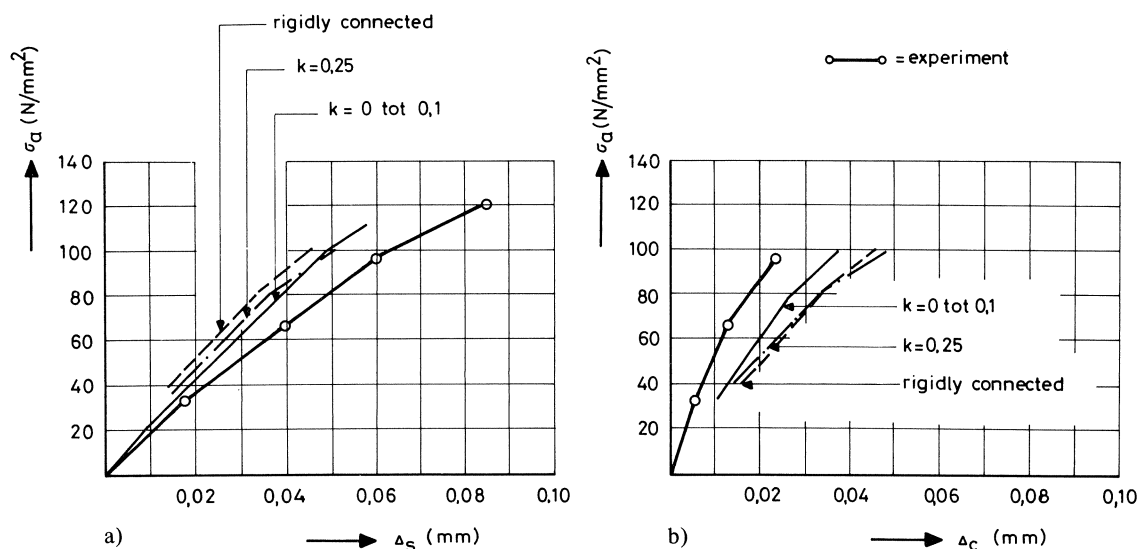


Fig. 8.3. Influence of the factor k in the uncracked phase.

a. elongation of reinforcement (Δ_s)

b. elongation of concrete directly beside reinforcement (Δ_c)

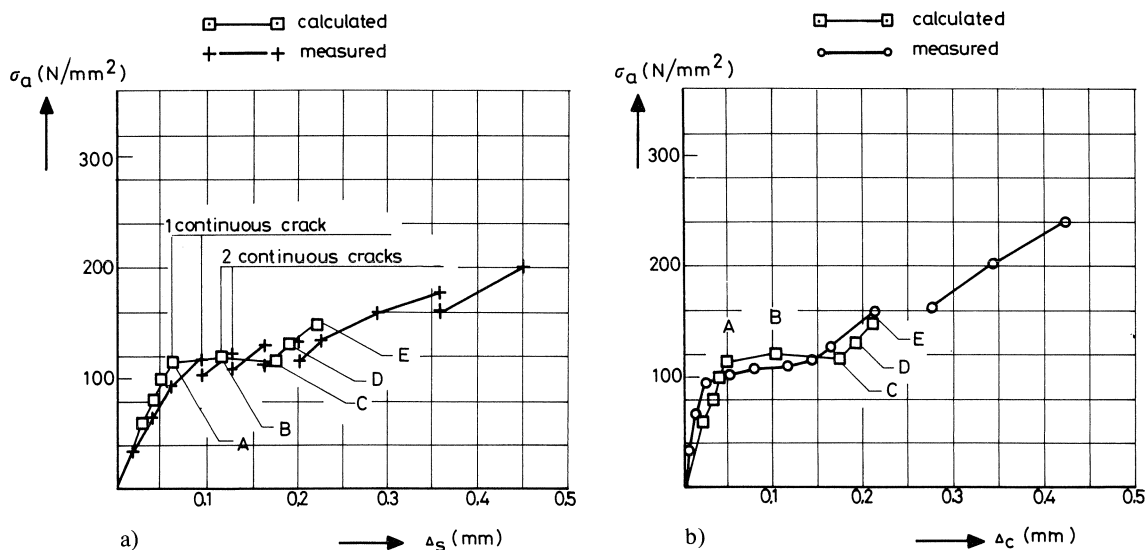


Fig. 8.4. Comparison of calculated results and experimental results for specimen with reinforcement $\varnothing 12$ from [4].

The results of the analysis are presented in Fig. 8.3, which is to be conceived as a detail of the first branch in Fig. 8.4, where the steel stress has been plotted as a function of the total elongation of the steel (Δ_s) and of the total elongation of the concrete (Δ_c). It appears that in Fig. 8.4 the cases corresponding to the values 0, 0.05 and 0.1 for k vir-

tually coincide with one another, whereas the case $k=0.25$ is somewhat too rigid. Of greater importance with regard to the choice of k , however, is the level of load at which the specimen cracks through. For $k=0$ this occurs at too high a load, whereas for $k=0.25$ a load is found which is too low in comparison with the experimental value. The cases $k=0.05$ and $k=0.1$ do indeed both lead to a satisfactory load level, but the differences between them are hardly perceptible, so that no preference for one or the other of these two cases can be stated.

8.4 *Comparison of numerical and experimental results*

The calculated results are compared with the experimental ones in Fig. 8.4, where the experimental values have been taken from Figs. 21a and 21b of [4]. In Fig. 8.4a the steel stress at the free end has been plotted as a function of the total steel elongation Δ_s . Here, just as in [4], “total” refers to half the length of the specimen, i.e., $l = 300$ mm. In Fig. 8.4b the same steel stress has been plotted as a function of the elongation Δ_c of the concrete. In the diagram the point A corresponds to the load at which a through-and-through crack occurs at the restrained cross-section. When that happens, the actual specimen is halved, as it were. At point B there again occurs a through-and-through crack in the analysis, while point C relates to a fully developed crack pattern. In this context it is to be noted that in the analysis no states of equilibrium were found between point B and point C. Only after prolonged iteration, during which cracks were formed in all the elements, was equilibrium attained at point C. In the actual test the cracks developed in the manner deducible from Fig. 8.4a by considering the positions where two points representing measured values are located one above the other.

8.5 *Stress distribution*

For the points A, B and C in Fig. 8.4 the distribution of the shear stress and the axial steel stress, for $k=0.05$ and $k=0.1$ respectively, is represented in Figs. 8.5 and 8.6. For the points A and C in Fig. 8.4 the behaviour of the radial pressure on the reinforcing bar is also given. For case B this has been omitted because, in so far as the radial stresses were concerned, there were still too large unbalanced stresses present, this being due to the iteration not having been continued to a sufficiently advanced stage. This phenomenon was detected only some considerable time after the calculations had been performed, and it was then not considered justified to repeat all the calculations just for the sake of two diagrams, as the main aspects of the interaction of the forces involved would hardly be affected by this. This is more particularly because for $k=0.1$ the shear stress is affected by only $\frac{1}{10}$ of the error in the radial stress, while for $k=0.05$ this proportion is only $\frac{1}{20}$.

8.6 *Conclusions*

The chosen bond-slip parameters turn out to be a suitable choice for the test on a prismatic specimen under tensile load, as considered here. Therefore the parameters

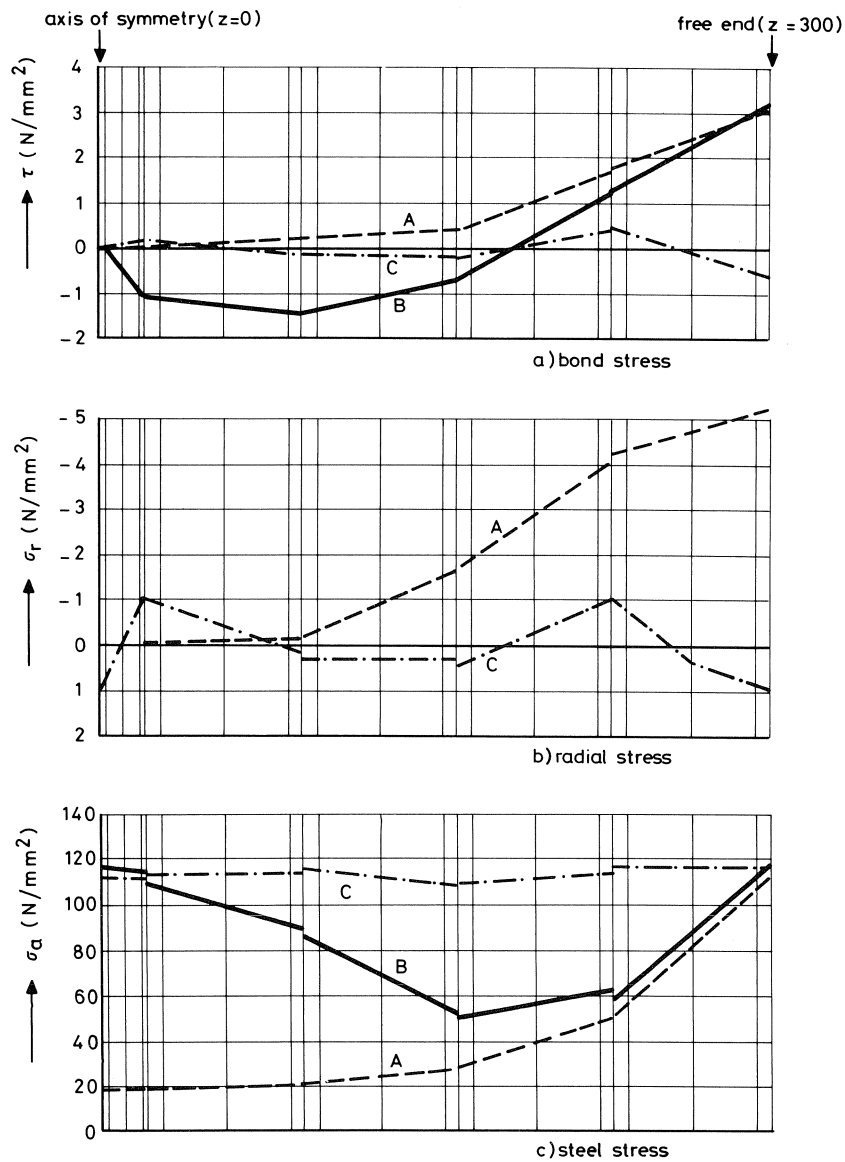


Fig. 8.5. Stress distribution along bar $k=0.05$.

employed still appeared to provide a reasonably satisfactory point of departure for further research:

$$\begin{aligned}
 S &= 200 \text{ N/mm}^3 \\
 k &= 0.05 - 0.1 \\
 \alpha &= 1 \\
 \Delta u_{\max} &= 0.025 \text{ mm}
 \end{aligned}$$

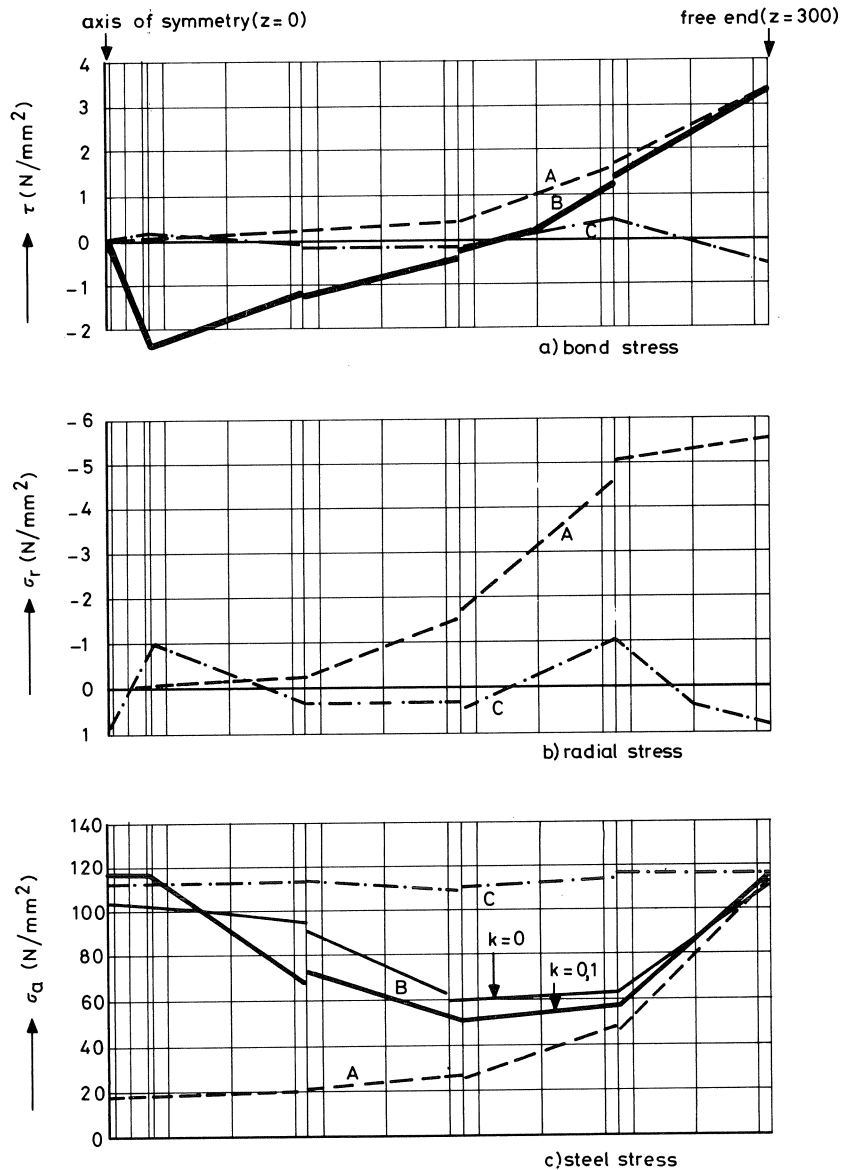


Fig. 8.6. Stress distribution along bar $k=0.1$.

9 Experiments for the general 3D element

9.1 Description of test specimens

For the purpose of verifying the general 3D bond-slip model, two specimens were experimentally investigated by TNO-IBBC [9]. The shape of the specimens was so chosen

that they could be said to simulate a freely supported end of a beam or slab. The aim was to test a structural detail in which the co-operation of concrete and steel would play an essential part. The choice of the model envisaged here was furthermore based on the consideration that, although the interaction of the forces involved was fairly complex, some rational insight into its behaviour was nevertheless available thanks to what had been learnt from earlier tests. This being so, it was felt that the experimental and numerical results obtained could be judged in a justifiable manner. To what extent the chosen specimens conformed to, or deviated from, the actual conditions in the end portion of a beam or slab was in fact not particularly relevant within the context of this research. After all, so long as such specimens were used both for the experimental and for the numerical investigations, comparisons between one set of results and the other would remain valid.

The specimens investigated are shown in Fig. 9.1. The overall (external) dimensions of both were $250 \text{ mm} \times 450 \text{ mm} \times 950 \text{ mm}$. Each specimen comprised two 425 mm long parts, symmetrically disposed in relation to each other, with an extension of 100 mm on one side. This extension was intended to ensure that failure would occur in the other part of the specimen, which was the part where all the measurements were performed. Strictly speaking, only the shorter part, with a length of 425 mm , should be regarded as the actual specimen (it is the part on the right in Figs. 9.1b and 9.1c).

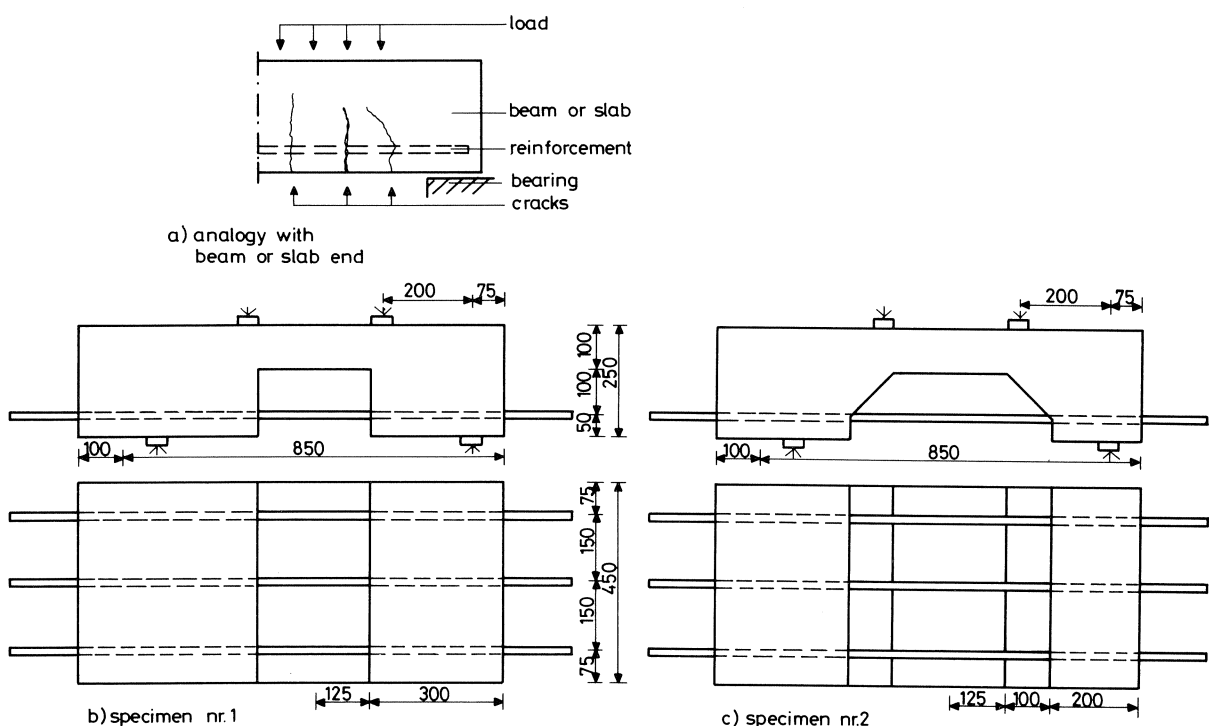


Fig. 9.1. Choice and shape of the specimens.

The reason for adopting different shapes for the two specimens was bound up with the need for measuring the strains in the concrete in the vicinity of the bars and, furthermore, with the cracking expected to occur in a structural detail of this kind. For want of a practical and accurate method of carrying out the measurements in the interior of the concrete, the solution adopted for the problem was based on the following considerations.

With a bearing and loading arrangement as shown in Fig. 9.1a, bond stresses will develop only after one or more cracks have occurred. After a crack has been formed, the behaviour of the part nearest the bearing becomes substantially independent of the concrete located on the other side of the crack. Hence if this concrete were omitted from a test specimen, the behaviour of the specimen would be approximately unchanged, and the exposed "crack face" would thus also become accessible for measuring the local strains in the concrete.

In specimen No. 1 the vertical surface directly beside the load application strip constitutes such a "crack face", on one side of which the concrete can be conceived as having been omitted. As this has been done only over a depth of 150 mm, the specimen itself remains at liberty to develop a larger depth of cracking.

It is known from experience that, after a crack has developed beside the load application strip, more cracks (may) occur between that crack and the bearing when the load is further increased. The situation that then arises was simulated in specimen No. 2, in which the vertical surface extending up to the reinforcement and continuing as the inclined surface towards the load application strip represented such a newly formed "crack face", on one side of which the concrete had been omitted.

Each test specimen contained three 16 mm diameter reinforcing bars installed at a distance $c + 0.5\phi = 50$ mm from the surface of the concrete. The bars were uniformly distributed across the width of each specimen and were spaced at 150 mm centres. The total anchorage length per bar was 300 mm in specimen No. 1 and 200 mm in specimen No. 2.

9.2 *Material data*

The 16 mm diameter reinforcing bars were of grade FeB 400 HW NR, with a modulus of elasticity $E_s = 0.21 \times 10^6$ N/mm².

At the time of testing specimen No. 1 the cube strength of the concrete was 33 N/mm². In the case of specimen No. 2 the cube strength was 41 N/mm² when this specimen was tested.

9.3 *Steel strain measurements*

For the purpose of strain measurements the reinforcing bars were provided in the longitudinal direction with grooves (2.5 mm wide, 2 mm deep) in which the strain gauges were glued. There were two of these grooves per bar, located diametrically opposite each other. In Fig. 9.2 this arrangement is shown in a photograph and also in a diagram representing a cross-section through a bar prepared in this way.

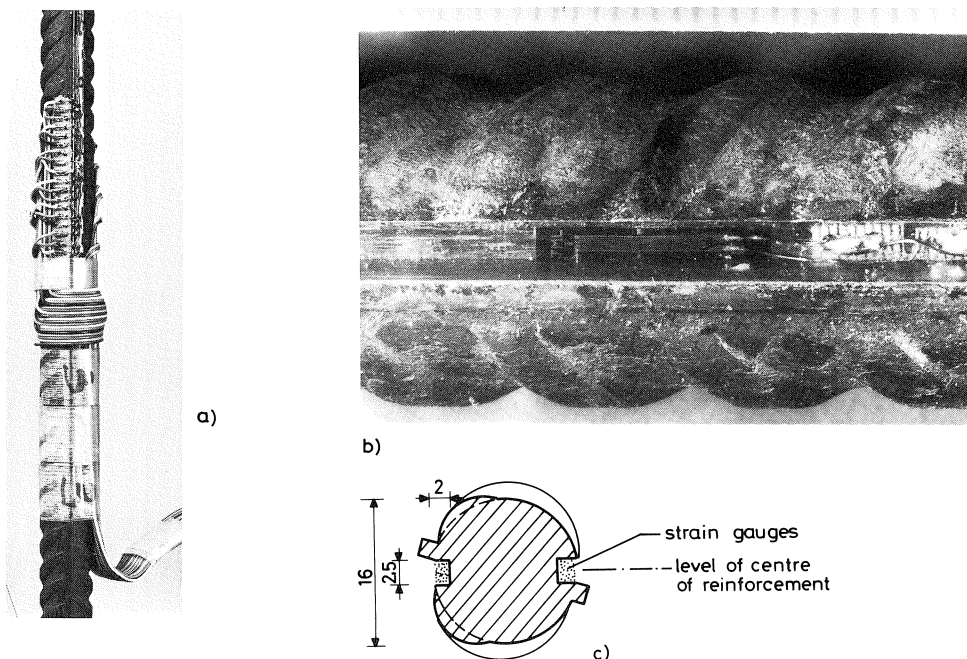


Fig. 9.2. Example of reinforcement employed, with attached strain gauges.
 a. pattern of deformations on bar, and strain gauge terminal
 b. detail of groove containing a strain gauge
 c. cross-section of bar showing position of grooves and strain gauges

Although in each specimen the strains were measured only on two of the three bars, for the sake of symmetry in the transverse direction the third bar (without strain gauges) was likewise provided with grooves. The cross-sectional area of all the bars was thus reduced by 5%. The grooves were carefully filled with glue, so as to restore the original perimeter of the bars. These were so positioned in the formwork that all the grooves were in the same plane (the horizontal plane through the centre-line of the reinforcement).

In principle, each load increment aimed at achieving a stress increase of 40 N/mm^2 in the non-embedded part of the centre bar. At half the value of the anticipated failure load a “loading loop” was interposed (load removal and reloading). After this, incremental increase of the load was continued until the specimen failed. As appears from the diagrams, this principle was not in fact closely conformed to: especially at high values of the load, at which the steel strains in the two bars in which they were measured differed rather considerably, a subsequent increment was chosen arbitrarily.

9.4 Results of the measurements

A number of results of measurements, which will be further considered, have been plotted in Figs. 9.3 to 9.8:

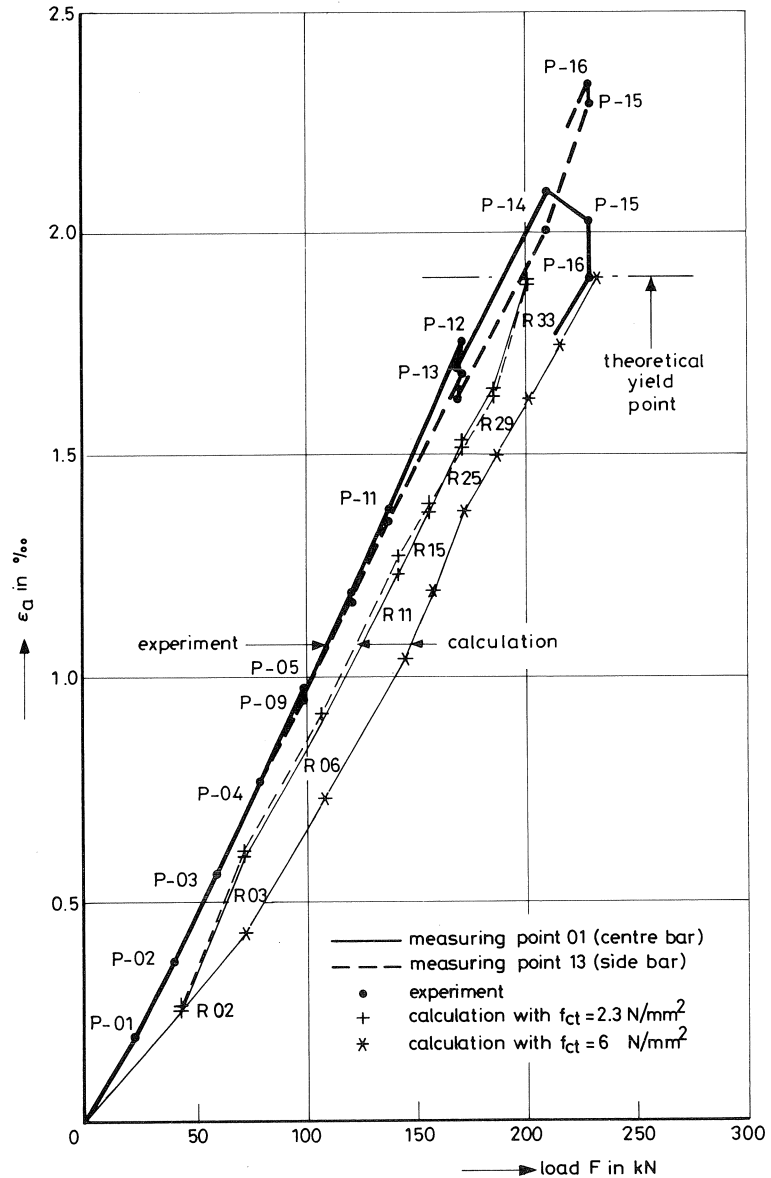


Fig. 9.3. Steel strains in the non-embedded lengths as a function of load; specimen No. 1.

- Figs. 9.3 and 9.4 show the steel strains in the reinforcing bars, measured in the non-embedded parts, as a function of the load F applied to the specimen.
- Figs. 9.5 and 9.6 show the distribution of the steel strains over the embedded lengths of the bars in the specimen.

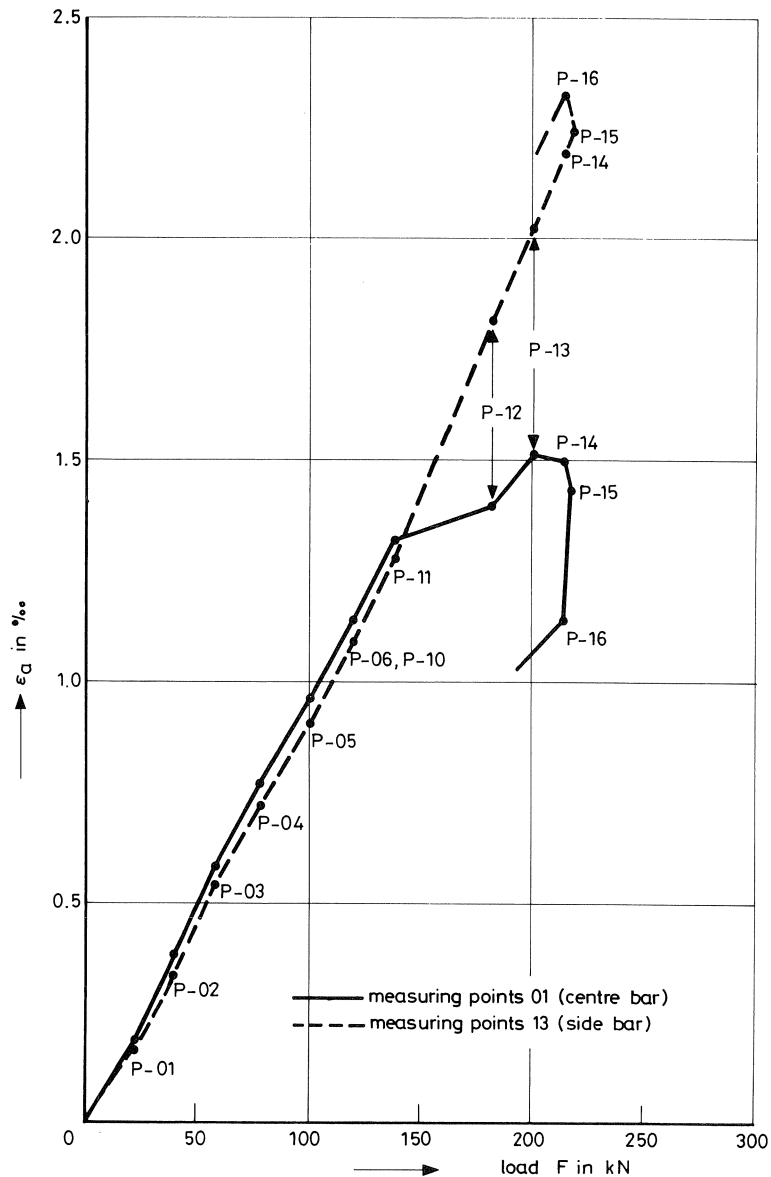


Fig. 9.4. Steel strains in the non-embedded lengths as a function of load; specimen No. 2.

- The difference between the displacement of a bar relative to the plane of cracking of the specimen and the displacement of the concrete directly beside it has been plotted against the local steel strain in Figs. 9.7 and 9.8.

Having regard to the accurately centred loading applied to the specimens, the dif-

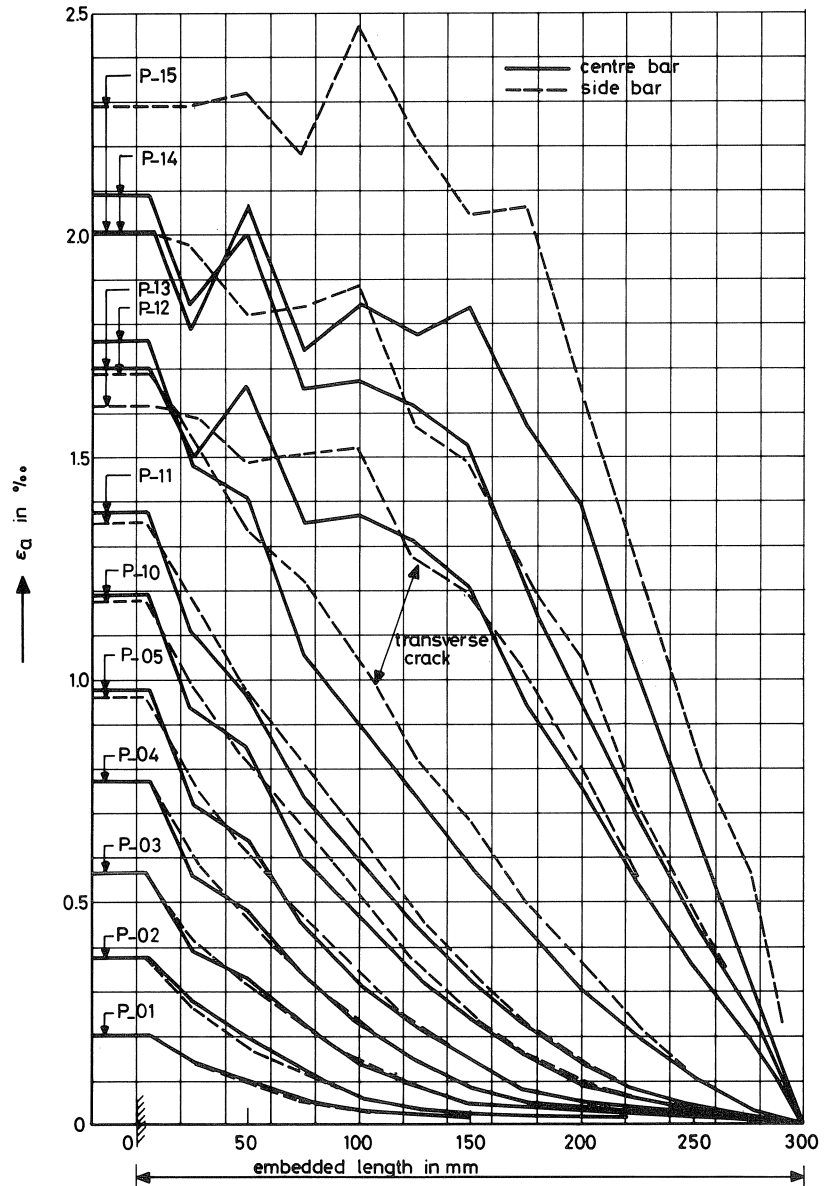


Fig. 9.5. Distribution of steel strains in specimen No. 1.

ference in behaviour of the centre bar and the side bar under relatively large load (as appears from Figs. 9.3 and 9.4) can be attributed only to the lower degree of lateral restraint of the side bar by the concrete and to the scatter in the strength. From the point of view of restraint the concrete around the side bar could be expected to split and

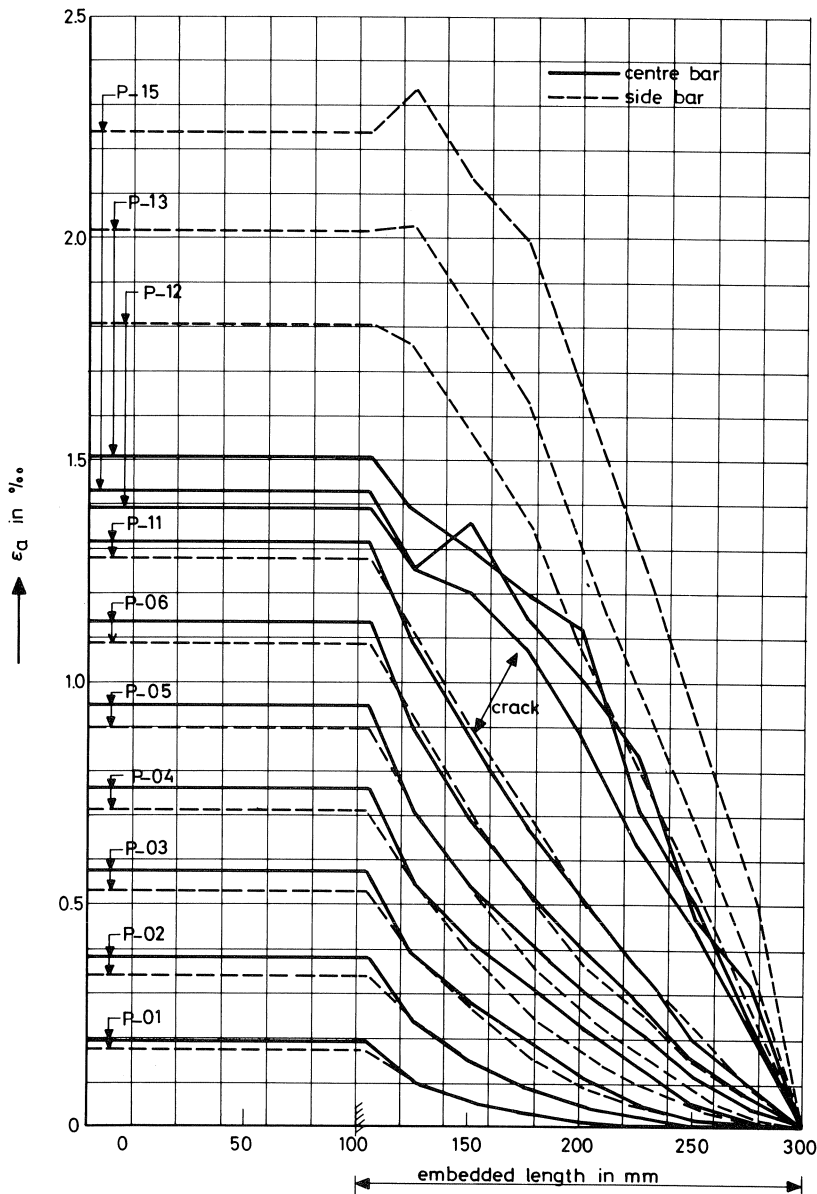


Fig. 9.6. Distribution of steel strains in specimen No. 2.

loosen its grip (so that the stress in the bar would decrease) more than around the centre bar. Yet in specimen No. 2 the very opposite occurred, and it is likely that the scatter played an important part in this case. The possible effect of shrinkage stresses in the concrete cannot be ruled out either.

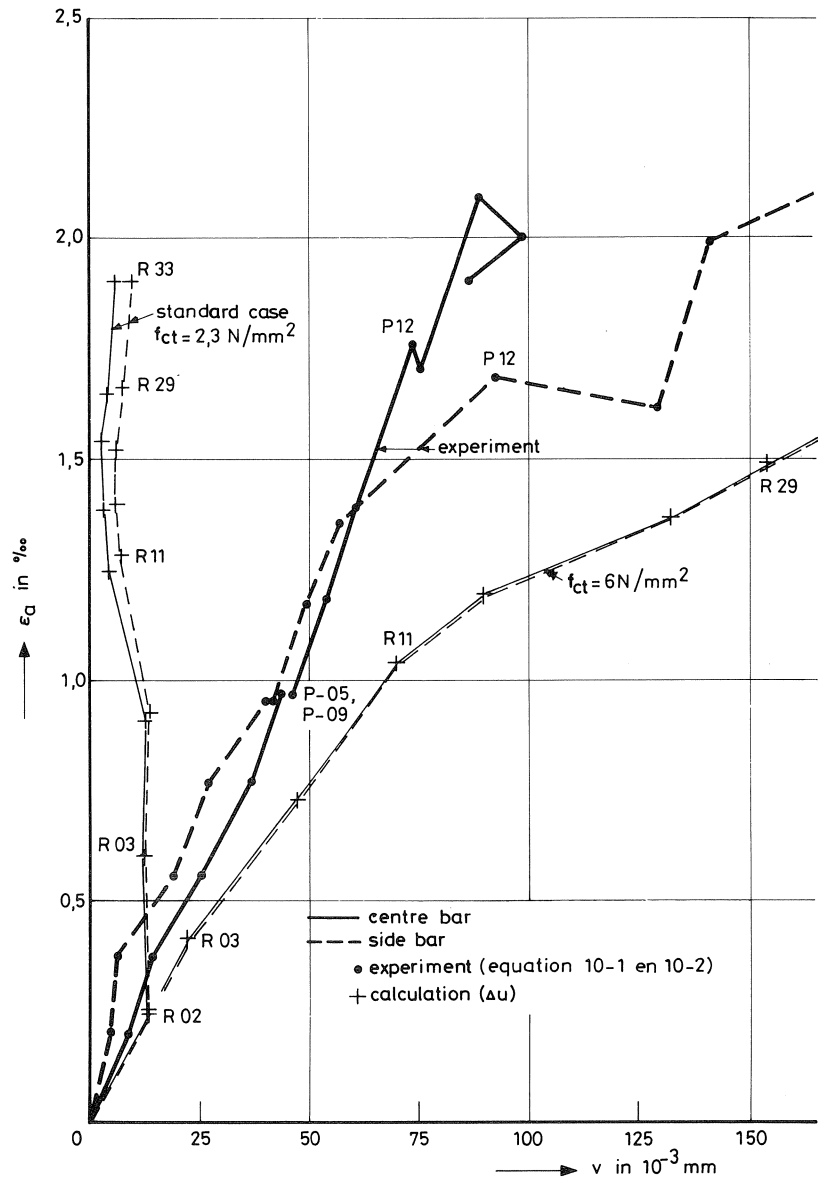


Fig. 9.7. Relative displacement of reinforcing bar/concrete as a function of local steel strain; specimen No. 1.

The measured steel strains plotted in Figs. 9.5 and 9.6 fairly accurately represent the stress distribution in the bar along its embedded length. Any abrupt major increase in stress along the bar is due to the formation of (macro) cracks in the concrete, after which the steel strains in the cracked-off part show a more erratic behaviour.

The relative displacement of a reinforcing bar with respect to the adjacent concrete

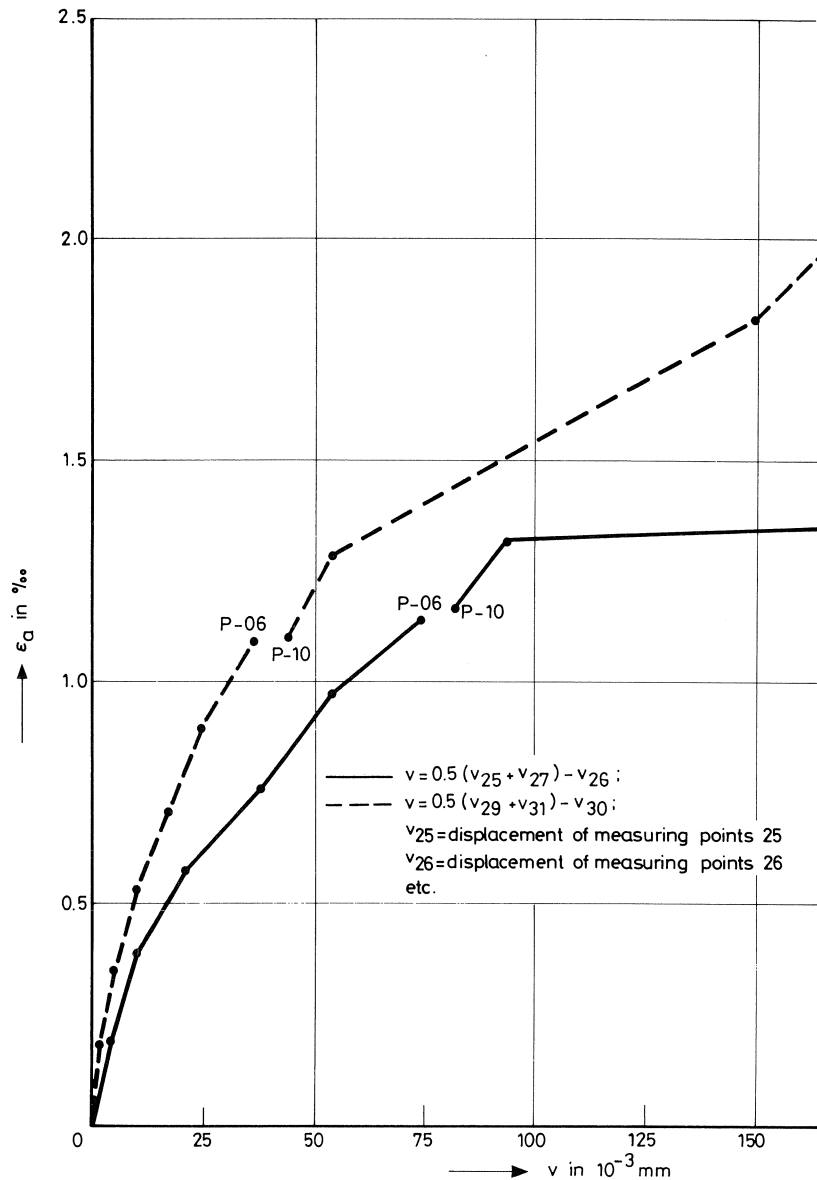


Fig. 9.8. Relative displacement of reinforcing bar/concrete as a function of local steel strain; specimen No. 2.

(see Figs. 9.7 and 9.8) should not be conceived as actual slip between steel and concrete. The relevant measuring points on the concrete were located at 12.5 mm from the centre-line of the bar or at 4.5 mm from the theoretical "shell" of the bar. The actual slip, if any, was certainly less than the values indicated in Figs. 9.7 and 9.8. Finally in the Figs. 9.9 and 9.10 the specimens No. 1 and No. 2 are shown after failure.

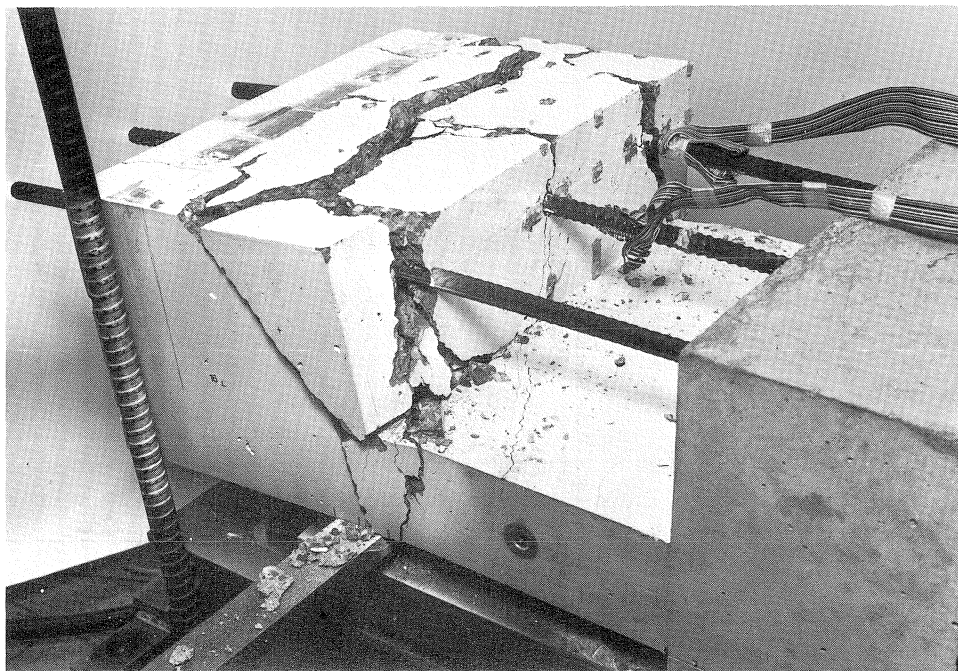


Fig. 9.9. Specimen No. 1 after failure.

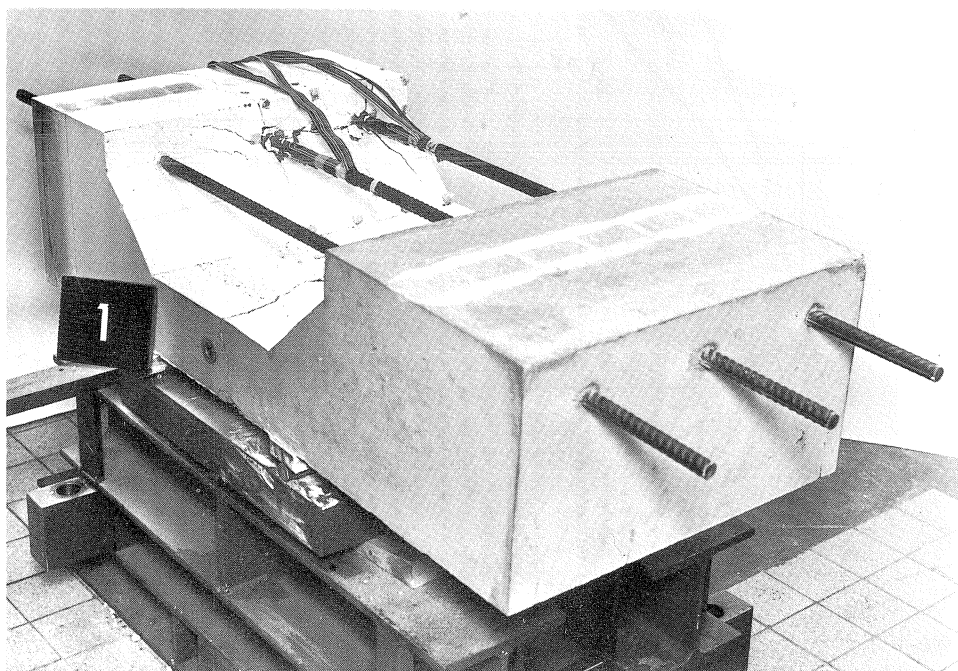


Fig. 9.10. Specimen No. 2 after failure.

10 Verification of the general 3D element

10.1 Mathematical model

The experimental results obtained with specimen No. 1, as reported in Chapter 9, were used for verifying the general 3D element. On the basis of symmetry considerations only a portion of the actual model shown in Fig. 9.1b was analysed for the present purpose, namely, the portion represented by full lines in Fig. 10.1. In this case 57 volume elements, 12 slips elements (3D) and also two bar elements were used, the two last-mentioned taking account of the reinforcement protruding from the specimen.

The manner of loading and the schematization of the boundary conditions are shown in Fig. 10.2. Of course, the load considered here is half the load F applied to the actual specimen. The load which was applied to the top of the specimen, on the second row of elements (see Fig. 10.1), was conceived as uniformly distributed. It was introduced into the analysis as an equivalent set of nodal forces (see Fig. 10.3).

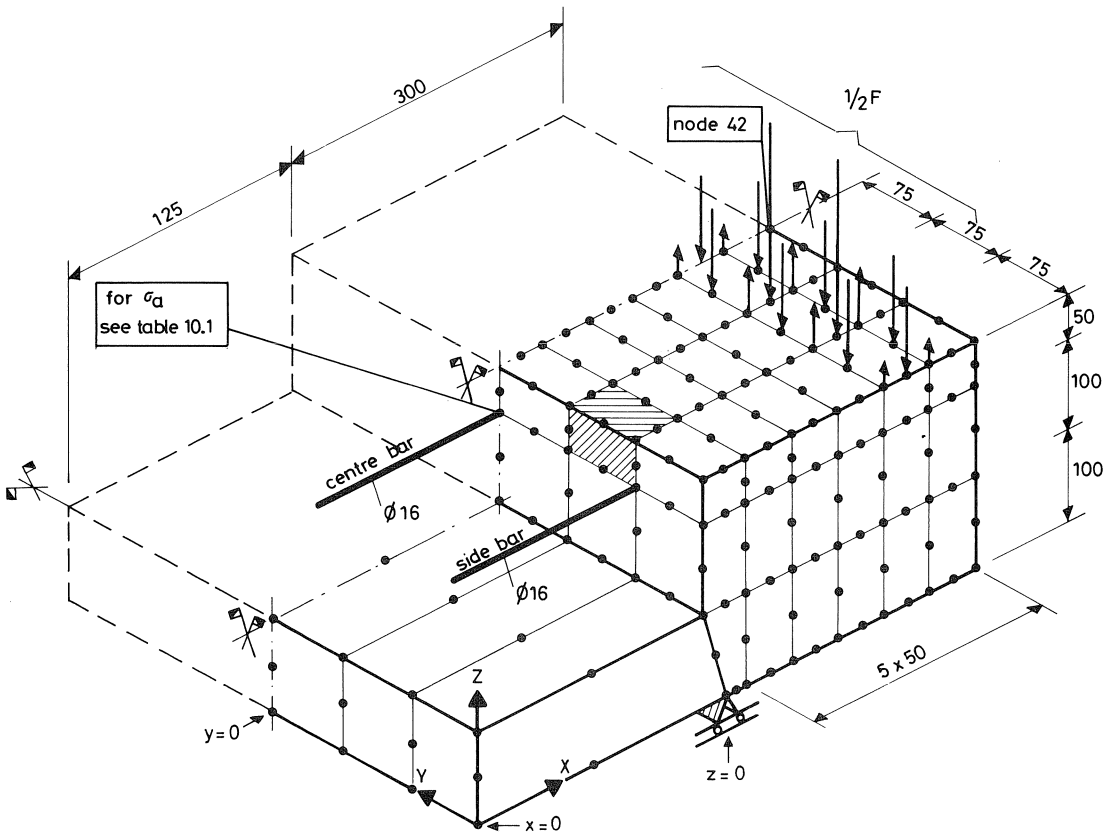


Fig. 10.1. Geometry and distribution of elements.

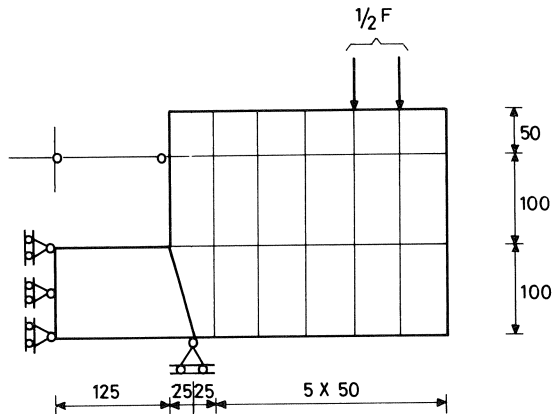


Fig. 10.2. Manner of loading and boundary conditions.

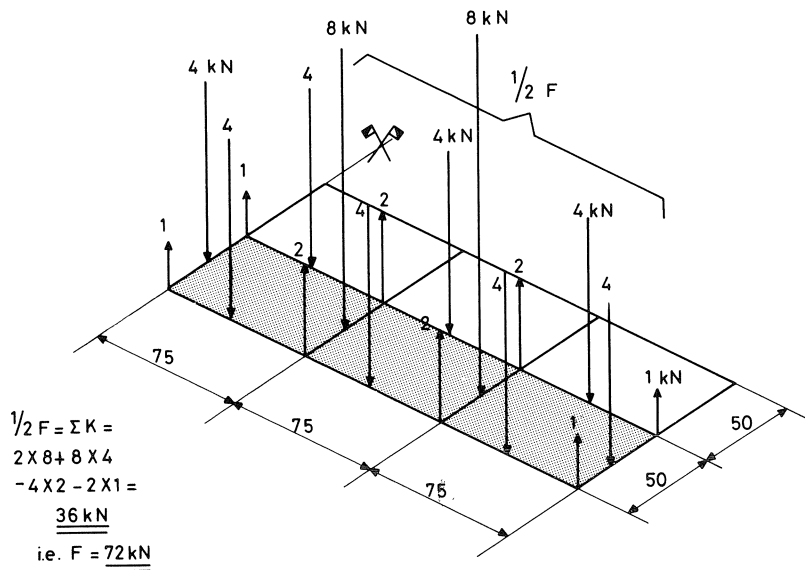


Fig. 10.3. Equivalent nodal forces.

10.2 Material properties adopted in the analysis

At the time of beginning the analysis the precise values of the material properties of the specimen were not yet known. However, the values that were adopted for the purpose were in reasonably good agreement with the measured cube strength and the values derivable from this.

More particularly, the following values for the concrete were introduced:

- compressive strength $f_{cc} = 29.6 \text{ N/mm}^2$
- modulus of elasticity $E_c = 30000 \text{ N/mm}^2$
- uniaxial tensile strength $f_{ct} = 2.3 \text{ N/mm}^2$
- Poisson's ratio $\nu_c = 0.2$

Table 10.1 Calculation procedure

increment	factor	F (kN)	number of iterations	norm of the displacement increases	v_{x42} (mm)	v_{z42} (mm)	σ_a (N/mm ²)
R-01	0.662		0	$0.4680 \cdot 10^{+1}$	0.0859	-0.141	49.8
R-02	0.662		5	$0.1497 \cdot 10^{-4}$	0.0907	-0.148	53.4
R-03	1.0	72	5	$0.9409 \cdot 10^{-2}$	0.170	-0.258	109
R-04	1.5		5	$0.1156 \cdot 10^{-1}$	0.283	-0.419	180
R-05	1.5		5	$0.5478 \cdot 10^{-2}$	0.310	-0.452	188
R-06	1.5	108	10	$0.2437 \cdot 10^{-2}$	0.344	-0.495	192
R-07	2.0		10	$0.1315 \cdot 10^{-1}$	0.453	-0.653	250
R-08	2.0		10	$0.8174 \cdot 10^{-2}$	0.513	-0.728	258
R-09	2.0		10	$0.6439 \cdot 10^{-2}$	0.561	-0.793	260
R-10	2.0		10	$0.4771 \cdot 10^{-2}$	0.601	-0.847	259
R-11	2.0	144	10	$0.4099 \cdot 10^{-2}$	0.637	-0.839	261
R-12	2.2		10	$0.6239 \cdot 10^{-2}$	0.715	-1.00	264
R-13	2.2		10	$0.5157 \cdot 10^{-2}$	0.754	-1.05	269
R-14	2.2		10	$0.4791 \cdot 10^{-2}$	0.781	-1.09	272
R-15	2.2	158.4	10	$0.4285 \cdot 10^{-2}$	0.808	-1.13	274
R-16	2.4		10	$0.6685 \cdot 10^{-2}$	0.879	-1.22	313
R-17	2.4		10	$0.5917 \cdot 10^{-2}$	0.914	-1.27	314
R-18	2.4		10	$0.5498 \cdot 10^{-2}$	0.947	-1.31	316
R-19	2.4		10	$0.5617 \cdot 10^{-2}$	0.980	-1.35	317
R-20	2.4		10	$0.5606 \cdot 10^{-2}$	1.01	-1.39	318
R-21	2.4		10	$0.5633 \cdot 10^{-2}$	1.05	-1.44	319
R-22	2.4		10	$0.5653 \cdot 10^{-2}$	1.08	-1.48	320
R-23	2.4		10	$0.5662 \cdot 10^{-2}$	1.12	-1.52	320
R-24	2.4		10	$0.5576 \cdot 10^{-2}$	1.15	-1.56	321
R-25	2.4	172.8	10	$0.5557 \cdot 10^{-2}$	1.19	-1.60	321
R-26	2.5		10	$0.6925 \cdot 10^{-2}$	1.24	-1.67	330
R-27	2.5		10	$0.6496 \cdot 10^{-2}$	1.28	-1.72	334
R-28	2.5		10	$0.6375 \cdot 10^{-2}$	1.32	-1.76	335
R-29	2.6	187.2	10	$0.7676 \cdot 10^{-2}$	1.38	-1.84	347
R-30	2.7		10	$0.9047 \cdot 10^{-2}$	1.45	-1.92	360
R-31	2.8		10	$0.1016 \cdot 10^{-1}$	1.42	-2.01	373
R-32	2.9		10	$0.1166 \cdot 10^{-1}$	1.60	-2.11	385
R-33	3.0	216	10	$0.1257 \cdot 10^{-1}$	1.68	-2.21	398

It was again assumed that the behaviour of the concrete could be described in terms of the Mohr-Coulomb yield criterion, without hardening, supplemented by two tension cut-off criteria (see Fig. 6.1.). The parameters that determine this model are f_{cc} , f_{ct} , and f_{i2} and f_{i3} . The tensile strength f_{ct} was taken as 2.3 N/mm²; for f_{i2} twice this value was assumed, i.e., $f_{i2} = 4.6$ N/mm², while f_{i3} was taken as equal to $1.01f_{i2}$. This conforms to the results of verification calculations previously carried out.

With equations (6.4) and (6.5) these values lead to $\theta = 0.82$ for the angle of internal friction and $c = 5.9 \text{ N/mm}^2$ for the cohesion. The modulus of elasticity of the reinforcing steel was $E_s = 205600 \text{ N/mm}^2$, while Poisson's ratio for the steel was taken as zero.

The following values were adopted for the further parameters determining the bond-slip behaviour:

$$S = 200 \text{ N/mm}^3; \quad k = 0.05; \quad \Delta u_{\max} = 0.025 \text{ mm}$$

10.3 Calculation procedure

In a non-linear analysis with DIANA the procedure comprises first performing a linear elastic analysis. Next, it is investigated by what factor the applied load can be multiplied so as just not to bring about any non-linear phenomena such as yielding and cracking. This factor was found to be 0.662. From Fig. 10.3 it is apparent that, at that instant, a load equal to $0.662 \times 36 = 23.83 \text{ kN}$ was acting on the "half" specimen. The corresponding load on the actual specimen was twice as large, i.e., $F = 47.66 \text{ kN}$. This load caused incipient cracking in an element located beside the side bar (the element in question is shown hatched in Fig. 10.1). The load was then increased incrementally; several iterations had to be performed per increment. These increments are listed in Table 10.1, which states the norm of the displacements increases along with other information (increment number, load factor, total load, number of iterations). By "norm" is understood the sum of the squares (quadratic values). It is to be noted, too, that the increment numbers are designated by R-01, R-02, etc. to distinguish them from the load increments applied in the test, the latter being designated (where necessary) by P-01, P-02, etc. in Chapter 9. The x and z displacements of node 42 (its location is indicated in Fig. 10.1) have likewise been given in Table 10.1 (columns v_{x42} and v_{z42}), as is also the steel stress in the centre bar portion protruding outside the specimen.

It can be inferred from the table that the rate of convergence is not great – probably because in the version of DIANA employed in this research, namely, DIANA NL03 (constant stiffness matrix method), during iteration the unbalanced stresses are eliminated with the original elastic stiffness matrix and not, as in the subsequent series DIANA NL04 and NL05, with a tangent stiffness (Newton Raphson or modified Newton Raphson). It further emerges from the table that, broadly speaking, the load was increased only when the norm of the displacements increases was less than 0.5×10^{-2} . At the higher load values, however, about twice this value of the norm was accepted, i.e., 1.0×10^{-2} .

The analysis was stopped at increment R-33 because in the mathematical model it had been assumed that the yield point of the reinforcement was $f_y = 400 \text{ N/mm}^2$, a stress that was almost attained at that increment ($\sigma_a = 398 \text{ N/mm}^2$), so that theoretically there was no point in further increasing the load.

10.4 Results of the analysis

More particularly those calculated results will be reported which are comparable with the measured results given in Chapter 9, especially concerning specimen No. 1.

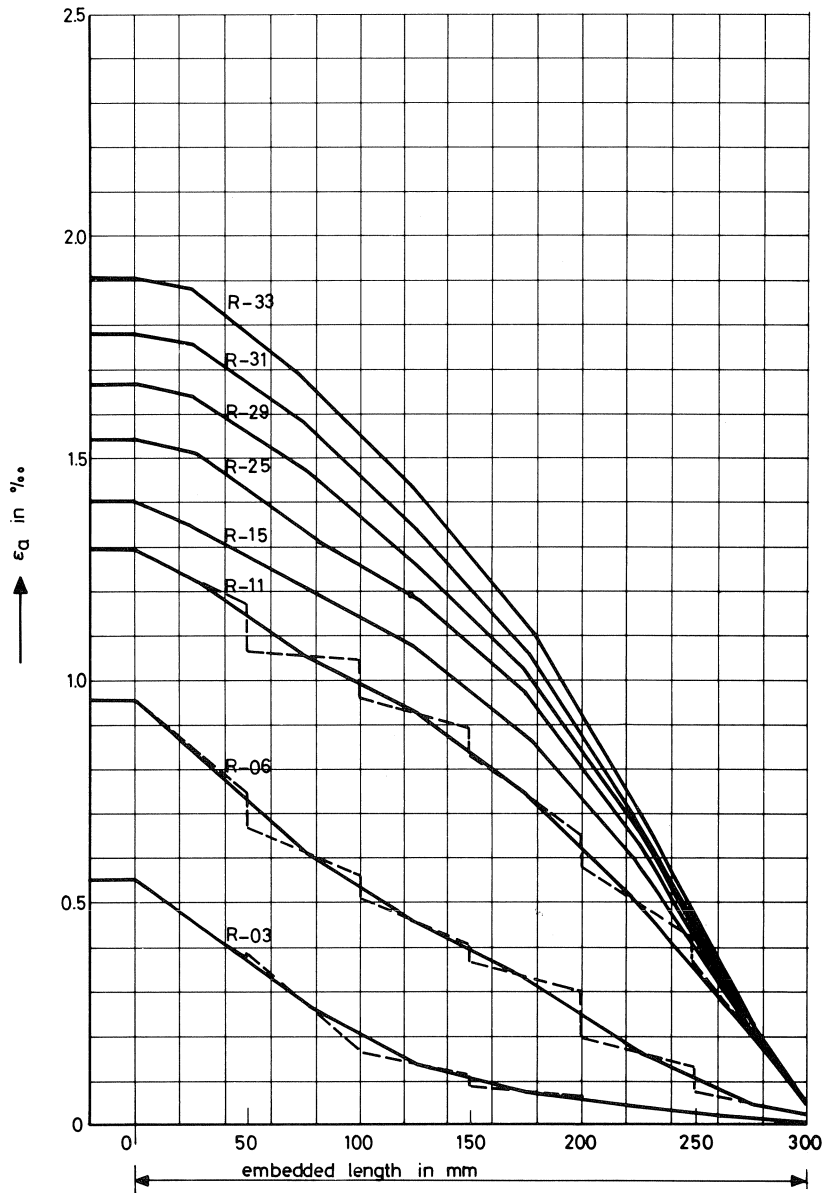


Fig. 10.4. Calculated distribution of steel strain in centre bar.

First, the distribution of the steel strain will be considered (see Figs. 10.4 and 10.5). The load increments "R" in the analysis which are directly comparable with the increments "P" in Chapter 9 are given in Table 10.2.

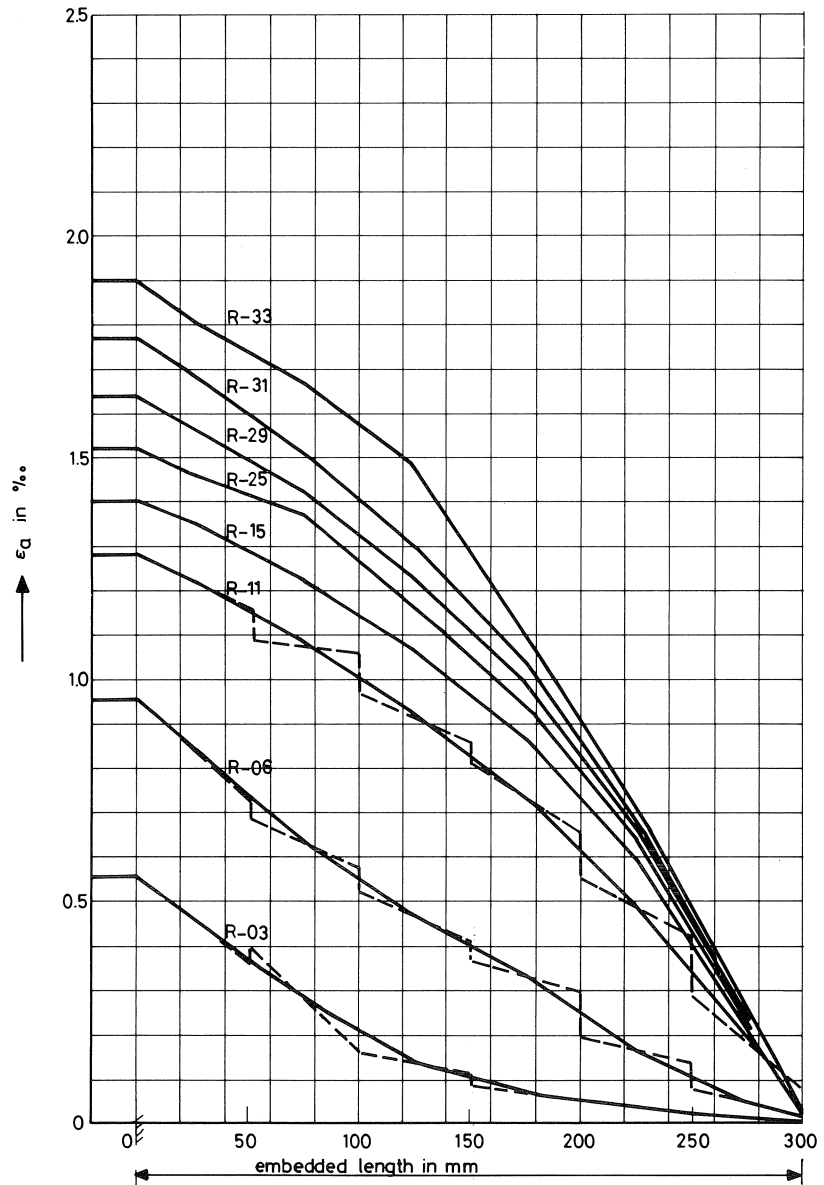


Fig. 10.5. Calculated distribution of steel strain in side bar.

Incidentally, the distribution represented in Figs. 10.4 and 10.5 has been somewhat stylized. For increments R-03, R-06 and R-11 the actual calculated result is indicated by a dotted line.

Discontinuities occur at the edges of the elements. The full (continuous) line is obtained by adopting in each case the middle value per element. The occurrence of dis-

Table 10.2 Summary of the comparable load increments

Fig.	load increment test	load F (kN)	load increment calculation	load F (kN)
10.12	P-03 P-04	60.5 80.1	R-03	72
10.13	P-05	99.4	R-06	108
10.14	P-11	139	R-11	144
10.15	P-12 P-13	173.1 170.4	R-25	172.8
10.16	P-14	210	R-33	216

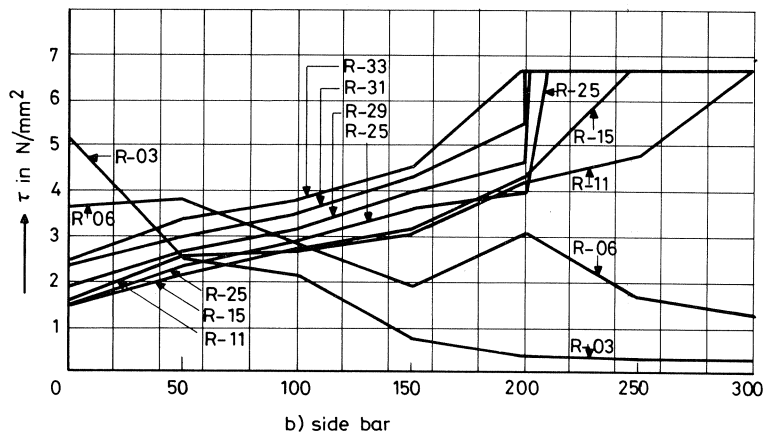
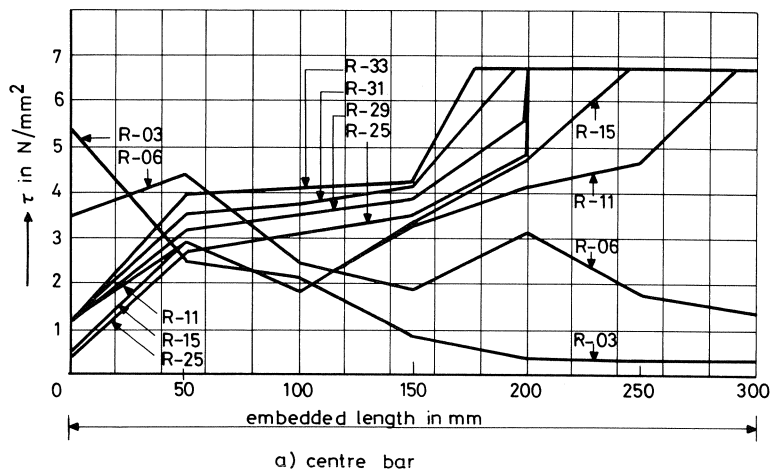


Fig. 10.6. Shear stress distribution.

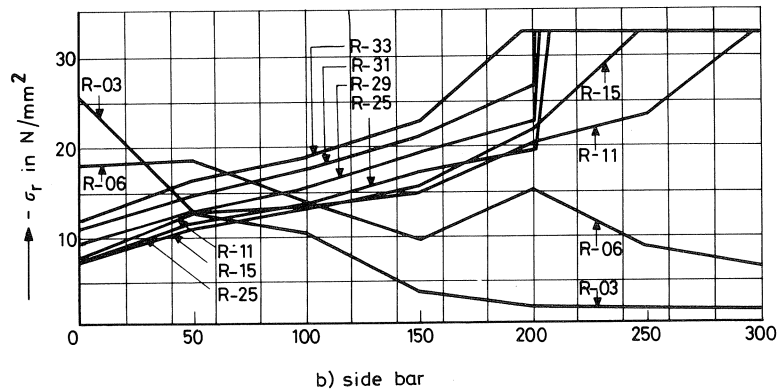
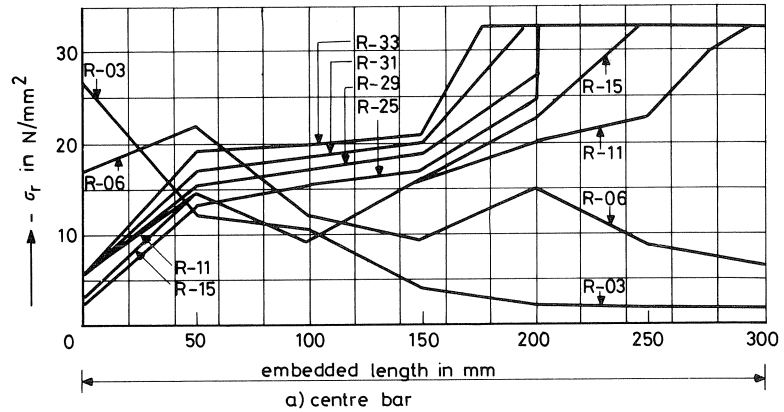


Fig. 10.7. Distribution of radial stress.

continuities in the steel strain curves is due to the fact that for these strains a linear behaviour follows from the assumed second-degree displacement field, while a linear displacement field was adopted also for the slip. Since the shear stress associated with slip should be the derivative of the steel stress, discontinuities are bound to occur.

In Figs. 10.6 and 10.7, respectively, the shear stress distribution and the radial pressure distribution along the reinforcement are represented. Since it was found in the calculations that the stresses perpendicular to the reinforcing bar always conformed to $\sigma_{xa} = \sigma_{xb} = \sigma_{ya} = \sigma_{yb}$, only one stress has been indicated, again designated as σ_r . This phenomenon of equal stresses, which merits closer attention in future investigations, is due to the fact that the calculations always yielded $\Delta v_{xa} = \Delta v_{xb} = \Delta v_{ya} = \Delta v_{yb} = 0$, so that with equation (3.5) it is found that $\sigma_{xa} = \sigma_{xb} = \sigma_{ya} = \sigma_{yb} = C_6 \varepsilon_a r / 2 - C_3 \Delta u$.

The stresses in Figs. 10.6 and 10.7 are not to be compared with measured results.

They have been indicated only in order to give insight into the interaction of the forces involved. Thus it is seen that, for increment R-03, the shear stress and radial stress in the diagrams start at a high value and rapidly die away (from left to right). For increment R-11, and higher, the behaviour is just the reverse. It is seen how the shear stress increases rapidly up to the maximum value obtained from the τ - Δ -relation. The transition is at increment R-06, this being due to cracking of the specimen.

Figs. 10.8 to 10.10 have been compiled with a view of giving some indication of the calculated cracking behaviour. These diagrams relate to the end, top and lateral faces, the locations of which are further explained in the relevant diagrams. The cracks shown in them are associated with the integration points nearest to the face concerned.

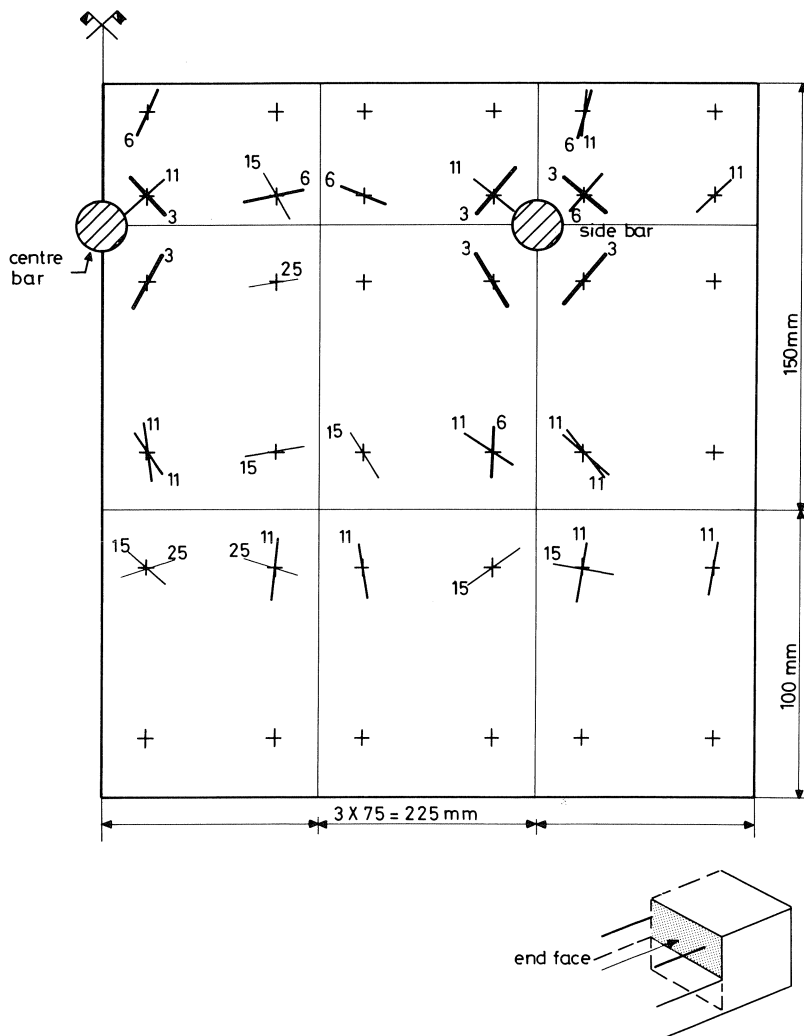


Fig. 10.8. Crack development on end face.

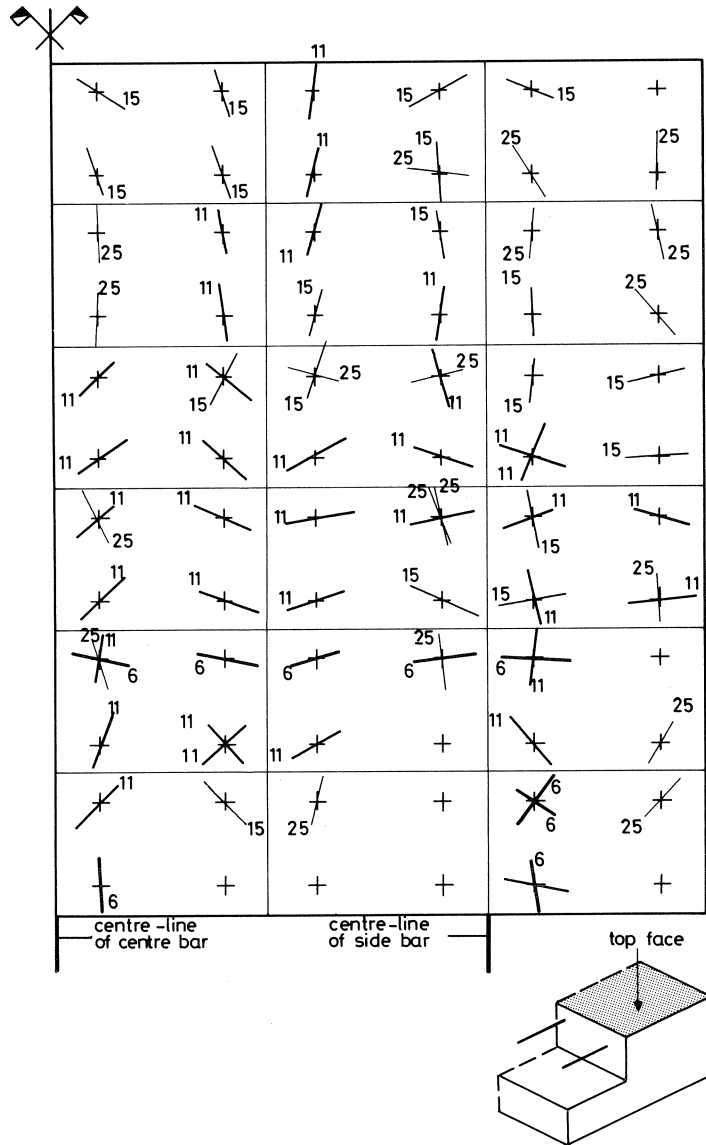


Fig. 10.9. Crack development on top face.

10.5 Comparison with experimental results

For a number of load levels which occurred both in the test and in the analysis (given in Table 10.2) some diagrams have been compiled in which the results obtained by calculation are compared with the experimental ones (Figs. 10.12 to 10.16). Besides the calculated results for the standard case (i.e., with the properties stated in Section 10.2), those for two variants are also represented in these diagrams. In the first variant a value

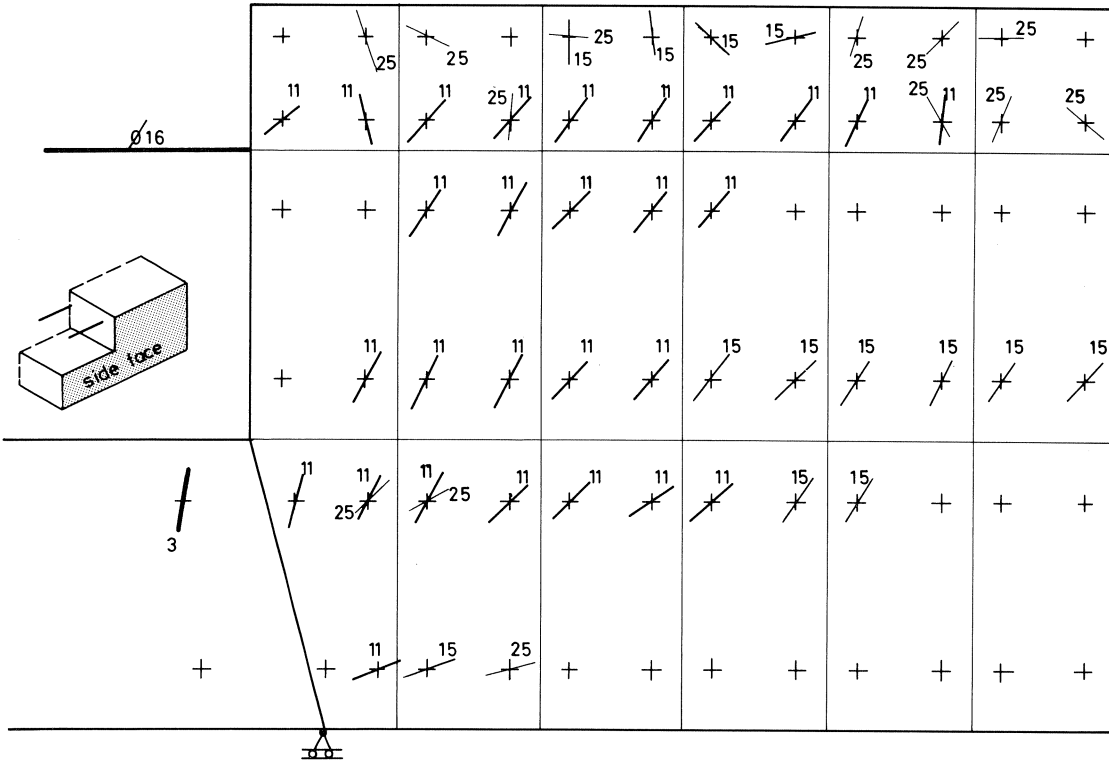


Fig. 10.10. Crack development on side face.

of 400 N/mm^3 has been adopted for S instead of 200 N/mm^3 as in the standard case. In the second, the concrete tensile strength f_{ct} in the specimen proper (see Fig. 10.11) has been increased from 2.3 N/mm^2 to 6 N/mm^2 .

The first thing that strikes one in Figs. 10.12 and 10.13 is that increasing the magnitude of S from 200 N/mm^3 to 400 N/mm^3 makes no appreciable difference. For this reason the curve for $S = 400 \text{ N/mm}^3$ has not been calculated for Figs. 10.15 and 10.16. On the other hand, the tensile strength has a much greater effect on the interaction of forces in the specimens. The tensile strength value introduced into the analysis determines the transition from a concave to a convex shape of the curves. In the test the transition was between P-12 and P-13, as appears from Fig. 9.5, whereas in the calculation this transition for the standard case (for which $f_{ct} = 2.3 \text{ N/mm}^2$) occurs much earlier: between R-06 and R-11 according to Fig. 10.4.

When the tensile strength is raised to the extreme value $f_{ct} = 6 \text{ N/mm}^2$, this transition no longer occurs anywhere. The transition from concave to convex is a direct function of the tensile strength upon which the through-and-through cracking of the specimen depends, this cracking being followed by a change in the distribution of forces in the specimen.

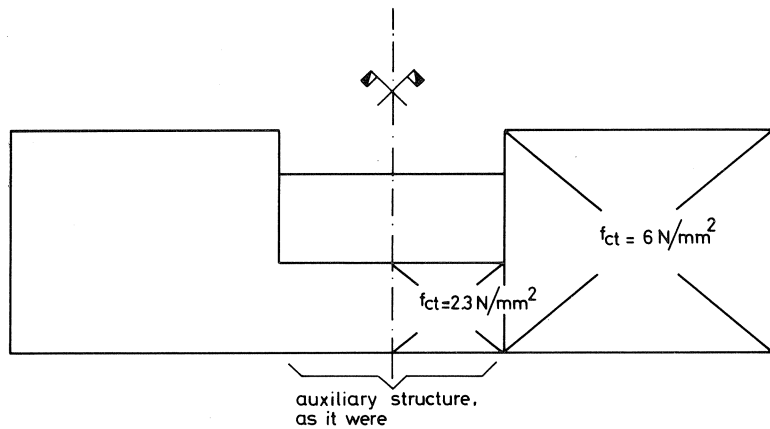


Fig. 10.11. Distribution of tensile strength in the two variant calculations.

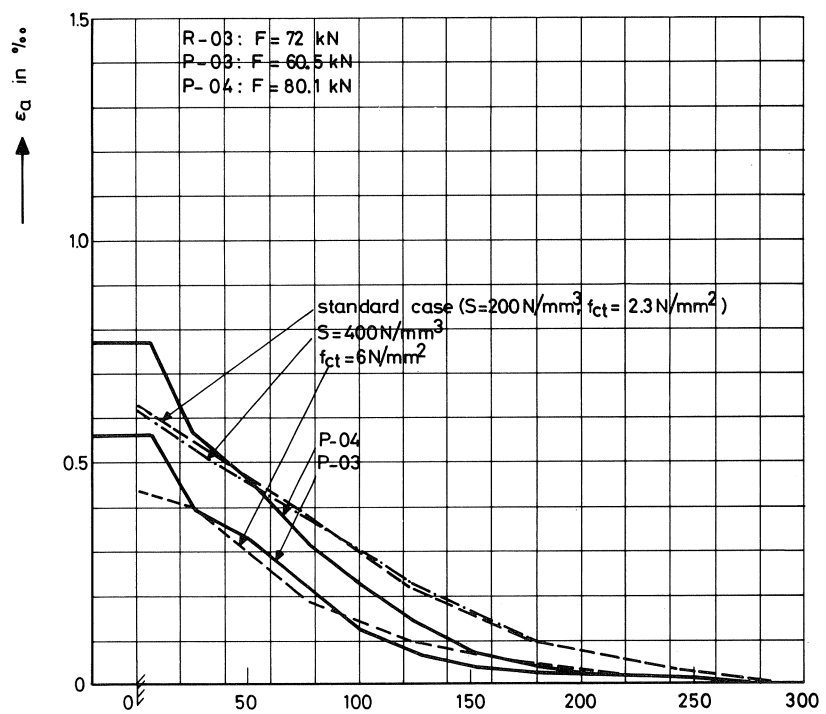


Fig. 10.12. Distribution of steel strains (centre bar) in specimen No. 1 along the embedded length according to calculation (R-03) and experiment (P-03 and P-04).

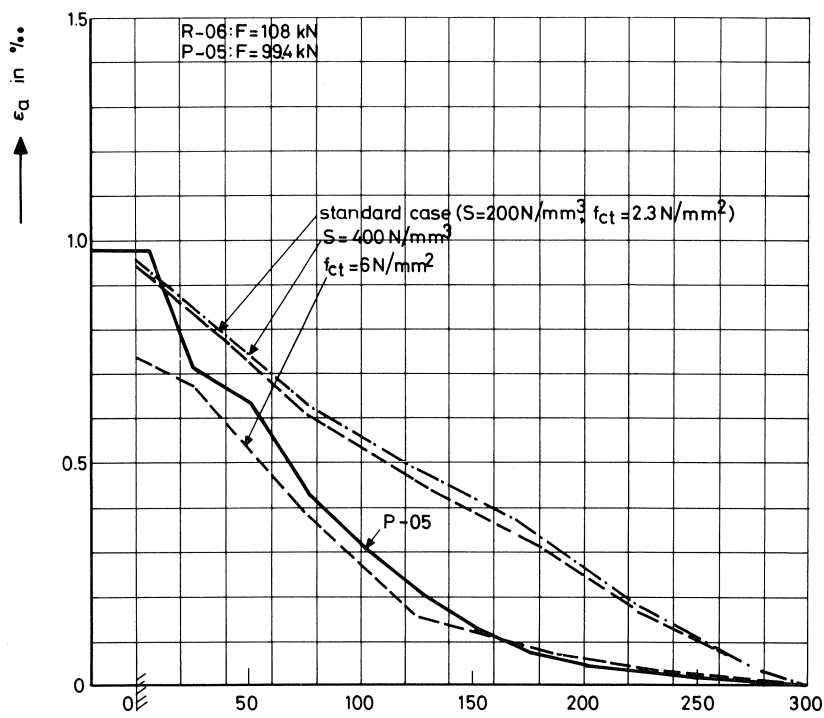


Fig. 10.13. Distribution of steel strains (centre bar) in specimen No. 1 along the embedded length according to calculation (R-06) and experiment (P-05).

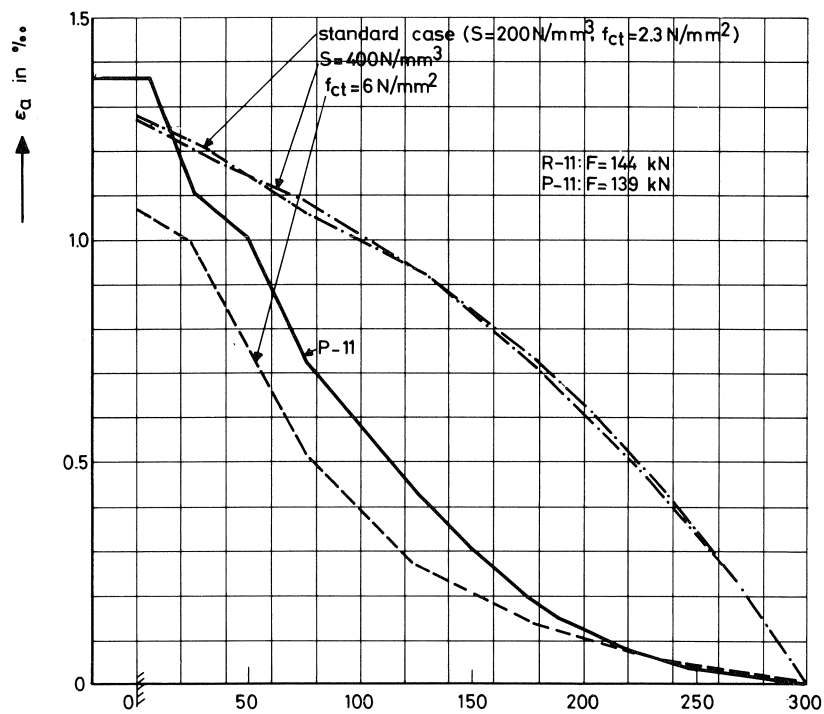


Fig. 10.14. Distribution of steel strains (centre bar) in specimen No. 1 along the embedded length according to calculation (R-11) and experiment (P-11).

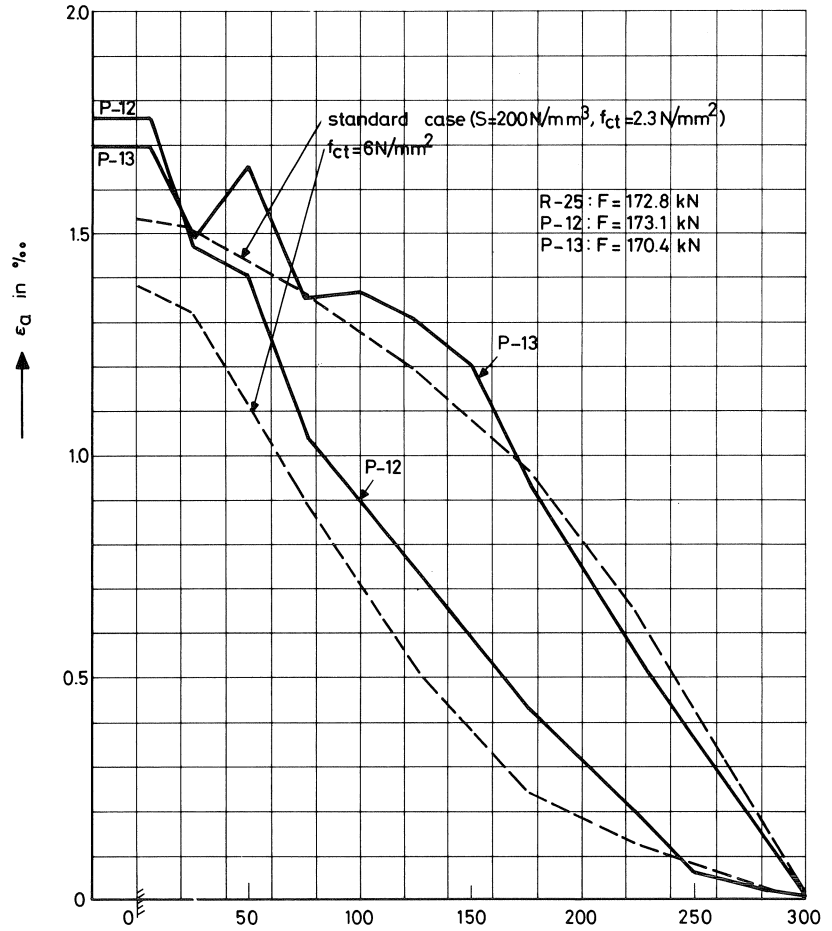


Fig. 10.15. Distribution of steel strains (centre bar) in specimen No. 1 along the embedded length according to calculation (R-25) and experiment (P-12 and P-13).

It is also possible to convey some idea of the agreement between the calculated slip (conceived as true slip) and the relative displacement v as deduced from the tests with the aid of the following definitions:

$$\text{edge bar: } v = 0.5(v_{29} + v_{31}) - v_{30} \quad (10.1)$$

$$\text{centre bar: } v = 0.5(v_{25} + v_{27}) - v_{26} \quad (10.2)$$

where v_{29} denotes the displacement of measuring point 29 in X -direction, etc. See Fig. 9.7 relating to specimen No. 1, in which, besides the experimental results, the calculated results are also indicated for $f_{ct} = 2.3 \text{ N/mm}^2$ and $f_{ct} = 6 \text{ N/mm}^2$ in so far as the slip at the plane of cracking is concerned. The curve corresponding to the results of the experiments is located between the two calculated curves.

That $f_{ct} = 2.3 \text{ N/mm}^2$ represents a reasonable choice is moreover apparent from Fig.

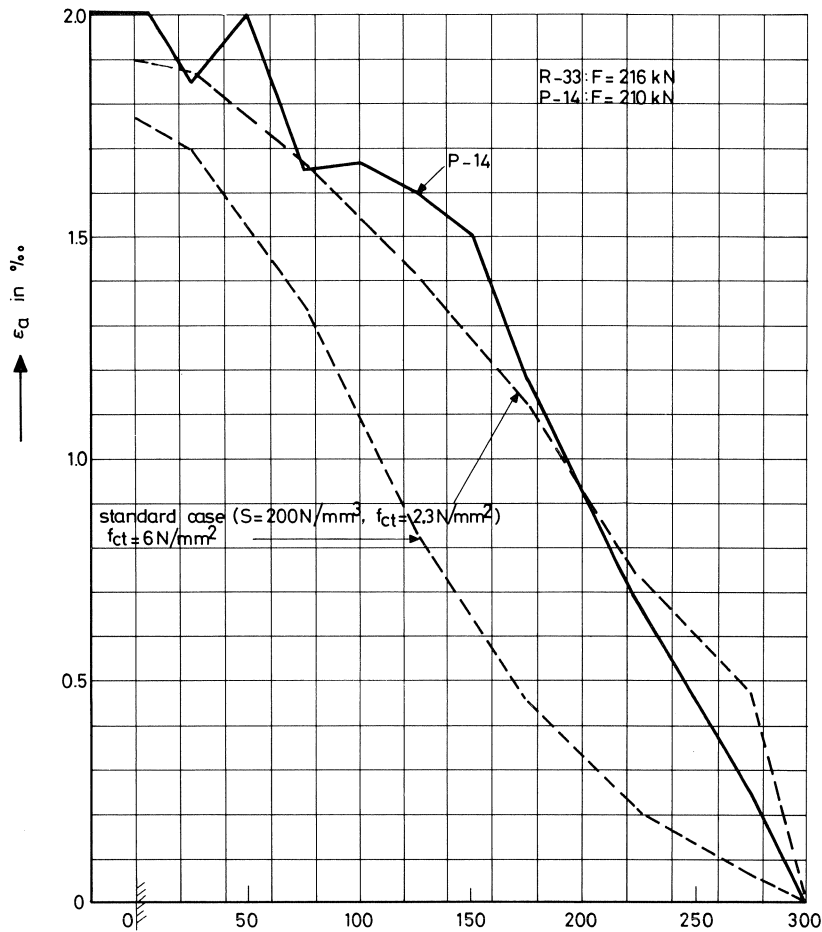


Fig. 10.16. Distribution of steel strains (centre bar) in specimen No. 1 along the embedded length according to calculation (R-33) and experiment (P-14).

9.3. It is found that for this value of f_{ct} the calculated strains of the reinforcing bars at the plane of cracking are in agreement with the measured strains. For $f_{ct} = 6 \text{ N/mm}^2$ the agreement is much poorer.

It is evident from what has been stated here that the tensile strength of the concrete plays an important part in the bond-slip model. Conceivably, the tensile strength of the concrete in the immediate vicinity of the reinforcing bar must have a different value from that in other parts of the concrete. However, having regard to the fairly coarse-meshed element distribution in the numerical model employed in this research, it was not possible to make such a distinction in tensile strength.

In future investigations, when available computer time and storage capacity will become less and less an impeding factor, this possibly essential distinction in tensile strength must not be lost sight of.

11 Conclusions

- In this publication a numerical model has been developed for the bond-slip relation between concrete and steel which takes account both of the slip resistance (by means of the slip modulus S) and of the mechanical interlocking (by means of a rib factor k). See Fig. 2.3. For the boundary layer thickness a coefficient α is used. The slip resistance is bounded with the aid of a limiting value for the slip (Δu_{\max}) which is dependent on the radial stress σ_r . The model is to be regarded as a generalization of the frequently adopted models comprising springs (Fig. 1.5). The numerical model is described with equation (2.30) for the axially symmetric case and with equation (4.1) for the 3D model. In Section 5 a translation of the 3D model into a 2D model has been proposed.
- Verification of the model with reference to the measured behaviour results in the following recommendation for the principal parameters:

slip modulus	S	$= 200\text{N/mm}^3$	
rib factor	k	$= 0.05$	for $\sigma_r \leq 0$ (compression)
	k	$= 0$	$\sigma_r > 0$ (tension)
layer thickness effect	α	$= 1$	
limiting slip	Δu_{\max}	$= 0.025\{1 + 1.5(\sigma_r/f_{cc})^2\}$ mm	$\sigma_r \leq 0$
	Δu_{\max}	$= 0.025\{1 - \sigma_r/f_{ct}\}$ mm	$\sigma_r > 0$

It is to be noted that the interrelation of the parameters requires further research, more particularly as regards the correct apportionment between mechanical interlocking and slip resistance.

- The cracking and therefore the tensile strength of the concrete plays a very important part in the interaction of forces. It would appear that this effect can be correctly taken into account only by assuming around the bond-slip element the presence of a boundary layer possessing a suitably adjusted concrete tensile strength. Variation of the layer thickness coefficient as employed here was in fact found to have little effect on the cracking behaviour.
- The numerical model for describing the behaviour of the concrete in general requires further investigation with a view to obtaining a clear insight into the question whether the actual behaviour can be described with the aid of an elasto-plastic model. Other questions to be considered in this context are what yield criterion and what tension cut-off criteria are most suitable. In the study reported here, good results were obtained with a Mohr-Coulomb yield criterion, without hardening, in combination with two tension cut-off criteria. These last-mentioned criteria were so chosen that plastic behaviour could occur only in the compression-compression-compression region. In the other regions of the stress space the material would undergo brittle fracture if a limit value was exceeded in the direction of the largest tensile stress. Tension cut-off criterion 1 is the determining one if a relatively low compressive stress is acting in a direction perpendicular to that of the largest tensile stress, in which case the limit value is the uniaxial tensile strength f_{ct} . Tension cut-off criterion

2 is applicable if there is a relatively high compressive stress acting in some other direction. The limit value then varies linearly from f_{ct} to zero in the case where the compressive stress attains the compressive strength f_{cc} .

References

1. Work plan and survey of "Betonmechanica", 1977.
2. Betonmechanica-deelproject 2: de aanhechtzone (Concrete mechanics, part 2: the bond zone). Report of CUR Day 1978, Cement XXX (1978) No. 11, pp. 536-539 (in Dutch).
3. MONNIER, TH., F. B. J. GIJSBERS and A. K. DE GROOT, Deelproject 2: samenwerking staal-beton (Sub-project 2: co-operation between steel and concrete). TNO-IBBC Report 77-46 (in Dutch).
4. GIJSBERS, F. B. J. and A. A. HEHEMANN, Enige trekproeven op gewapend beton (Some tensile tests on reinforced concrete). TNO-IBBC Report BI-77-61 (in Dutch).
5. DE GROOT, A. K. and G. M. A. KUSTERS, Parameterstudie met DIANA NL03 (parameter study with DIANA NL03) (axial symmetry without radial pressure) TNO-IBBC Report BI-78-09 (in Dutch). Parameterstudie met DIANA NL03 (Parameter study with DIANA NL03) (axial symmetry with radial pressure) TNO-IBBC Report BI-78-69 (in Dutch).
6. GIJSBERS, F.B.J., A. K. DE GROOT and G. M. A. KUSTERS, A numerical model for bond-slip problems. Contribution to the IASS Symposium 1978, Darmstadt "Non-linear behaviour of reinforced concrete spatial structures". Vol. 1, pp. 37-48, Werner Verlag, West Germany.
7. DE GROOT, A. K. and G. M. A. KUSTERS, Modificatie en uitbreiding van het slipelement (Modification and extension of the slip element). TNO-IBBC Report BI-79-3 (in Dutch).
8. DE GROOT, A. K. and G. M. A. KUSTERS, Toetsing symmetrische variant van het algemene aanhechtingsmodel (Verification of the symmetric variant of the general bond model). TNO-IBBC Report BI-80-4 (in Dutch).
9. DRAGOSAVIĆ, M. and A. K. DE GROOT, Samenwerking van beton en staal (Co-operation of concrete and steel). TNO-IBBC Report BI-80-47 (in Dutch).
10. DÖRR, K., Kraft- und Dehnungsverlauf von in Betonzylindern zentrisch einbetonierten Bewehrungsstäben unter Querdruck (Force and strain distribution of reinforcing bars, centrically embedded in concrete, under transverse pressure). Forschungsberichte aus dem Institut für Massivbau der Technischen Hochschule Darmstadt, No. 30 (1975) (in German).
11. EIBL, J. and G. IVANY, Studie zum Trag- und Verformungsverhalten von Stahlbeton (Study relating to the structural and deformation behaviour of reinforced concrete). Deutscher Ausschuss für Stahlbeton (DAfStb), Heft 260, Berlin (1976) (in German).
12. GOTO, Y., Cracks formed in concrete around deformed tension bars. ACI Journal, Proceedings, Vol. 68, No. 4, April 1971, pp. 244-251.
13. STAUDER, W., Ein Beitrag zur Untersuchung von Stahlbetonscheiben mit Hilfe finiter Elemente unter Berücksichtigung eines wirklichkeitsnahen Werkstoffverhaltens (Contribution to the investigation of reinforced concrete plates with the aid of finite elements, taking account of a realistic material behaviour). Thesis, Technological University of Darmstadt, 1973 (in German).
14. SCHÄFER, H., A contribution to the solution of contact problems with the aid of bond elements. Computer Methods in Applied Mechanics and Engineering, North-Holland Publishing Company, 6 (1975), pp. 335-354.
15. NILSON, A. H., Non-linear analysis of reinforced concrete by the finite element method. ACI Journal, Title No. 65-55, September 1965.
16. CEODOLIN, L. and S. DEIPOLI, Finite element non-linear analysis of reinforced concrete bi-dimensional structures. Technical Report No. 40, Politecnico di Milano, Department of Structural Engineering, September 1974.

17. VAN MIER, J., Onderzoek naar het schuifspanningsslip gedrag van geprofileerd wapeningsstaal en beton (Investigation of the shear slip behaviour of deformed reinforcing steel and concrete). Graduation thesis, Eindhoven University of Technology, Department of Architecture, June 1978 (in Dutch).
18. ZIENKIEWICZ, O. C., The Finite Element Method in Engineering Science. McGraw-Hill, London, 1977.
19. LUTZ, L. A. and P. GERGELY, Mechanics of bond and slip of deformed bars in concrete. ACI Journal, Title No. 64-62, November 1967.
20. DÖRR, K., Ein Beitrag zur Berechnung von Stahlbetonscheiben unter besonderer Berücksichtigung des Verbundverhaltens (Contribution to the analysis of reinforced concrete plates, with particular reference to the bond behaviour). Thesis D 17, Technological University of Darmstadt (1980) (in German).